INSTITUTO POTOSINO DE INVESTIGACIÓN CIENTÍFICA Y TECNOLÓGICA, A.C.

POSGRADO EN NANOCIENCIAS Y MATERIALES

Macroscopic effects of the microscopic structure in magnetic materials

Tesis que presenta

Victor Hugo Carrera Escobedo

Para obtener el grado de

Doctor en Nanociencias y Materiales

Director de la Tesis:

Dr. Armando Encinas Oropesa y Dr. Antonio Capella Kort

San Luis Potosí, S.L.P., 10 de Octubre 2023

Constancia de aprobación de la tesis

La tesis **Macroscopic effects of the microscopic structure in magnetic materials** presentada para obtener el Grado de de Doctor en Nanociencias y Materiales fue elaborada por **Victor Hugo Carrera Escobedo** y aprobada el **3 de noviembre del 2023** por los suscritos, designados por el Colegio de Profesores de la División de Materiales Avanzados del Instituto Potosino de Investigación Científica y Tecnológica, A.C.

_____

Dr. Armando Encinas Oropesa
(Director de la tesis)

_____

Dr. Antonio Capella Kort
(Director de la tesis)

_____

Dr. Sinhué López Moreno
(Asesor de la tesis)

_____

Dr. Jonathan Zamora Mendieta
(Asesor de la tesis)

Créditos Institucionales

Esta tesis fue elaborada en la División de Materiales Avanzados del Instituto Potosino de Investigación Científica y Tecnológica, A.C., bajo la dirección del Dr. Armando Encinas Oropesa y el Dr. Antonio Capella Kort.

Durante la realización del trabajo el autor recibió una beca académica del Consejo Nacional de Ciencia y Tecnología (297370) y del Instituto Potosino de Investigación Científica y Tecnológica, A. C. Por otro lado, también se recibió el apoyo del Centro Nacional de Súpercomputo y del Proyecto Ciencia de Frontera CONAHCyT CF-2023-G-122.

Resumen

En este trabajo se propone y valida un esquema numérico que permite estudiar características macroscópicas como función de la estructura microscópica de un material compuesto por partículas magnéticas monodominio. Lo anterior se lleva a cabo considerando una celda representativa del material que contiene un número finito de partículas con geometría arbitraria. Luego, se aplican condiciones de frontera de Dirichlet o de Robin para simular que el sistema está aislado o que se repite periódicamente en el espacio, respectivamente. Luego, a partir de la teoría micromagnetica, se coloca la ecuación diferencial del sistema en forma débil para posteriormente utilizar el método de elemento finito para obtener una configuración de las partículas que corresponda a un mínimo local de la energía micromagnética. Lo anterior, da como resultado una curva de histéresis que nos permite apreciar el comportamiento magnético del sistema en cuestión. Adicionalmente, se hace un desarrollo con más rigor sobre el mismo problema al utilizar dos aproximaciones: la primera es entender la celda como un sistema que a su vez está contenido dentro de un sistema de mayor escala y luego propagar los factores de demagnetización para obtener un factor de demagnetización del sistema compuesto. La segunda, es utilizar una muestra representativa de volumen para después utilizar el método de homogenización asintótica para obtener, de igual manera, un factor de demagnetización generalizado que contiene las propiedades de la microstructura así como un término que corresponde a la interacción entre celdas. Los resultados de este trabajo representan una solución complementaria para el estudio de ensambles de partículas magnéticas ubicada entre los modelos micromagnéticos y los de campo medio.

Palabras clave: micromagnetismo, método de elemento finito, método de homogenización asintótica, formulación débil.

Abstract

In this work, a numerical scheme is proposed and achieved, so that allows studying the macroscopic properties as a function of the microscopic structure of a material composed of monodomain magnetic particles. This is carried out by considering a representative cell of the material that contains a finite number of particles with arbitrary geometry. Then, Dirichlet or Robin boundary conditions are applied to simulate that the system is isolated or periodically repeated in space, respectively. Then, from the micromagnetic theory, the system's differential equation is placed in weak form to subsequently use the finite element method to obtain a configuration of the particles that corresponds to a local minimum of the micromagnetic energy. This results in a hysteresis curve that allows us to appreciate the magnetic behavior of the system in question. Additionally, a more rigorous development is made on the same problem by using two approximations: the first is to understand the cell as a system that is also contained within a larger-scale system and then propagate the demagnetization factors to obtain a demagnetization factor of the composite system. The second is to use a representative volume sample and then use the asymptotic homogenization method to obtain, in the same way, a generalized demagnetization factor that contains the properties of the microstructure as well as a term that corresponds to the interaction between cells.
Keywords: micromagnetism, finite element method, asymptotic homogenization method, weak formulation.

Palabras clave: micromagnetism, finite element method, asymptotic homogenization method, weak formulation.

(Página en Blanco que se va a utilizar para colocar la copia del acta de examen.)

Dedicatoria

A mi madre y padre, siempre.

Agradecimientos

A papá y mamá, por ser siempre una fuente de inspiración, apoyo, confianza y amor. Por nunca dejar de creer en mí persona (cuando ni yo lo hacía) y proyecto de vida. Por darme todas las oportunidades posibles, por ser siempre una fuente de sabiduría, consejos y ponerme siempre en el buen camino. Ser su hijo fue mi lotería. Gracias, en serio gracias.

A mis hermanos y sus familias, por estar siempre al pendiente.

A mis sobrinos y sobrinas, por ser siempre una inspiración y motivo para ser una buena persona. Servir siempre, aunque sea de mal ejemplo.

Al Dr. Armando y al Dr. Antonio, por tener siempre la paciencia y la dedicación de enseñarme todo lo que hizo falta de física, matemáticas y la vida. Me llevo lo que me enseñaron para pasarlo a mis estudiantes.

A Fernanda Ruíz, mi mejor amiga y cómplice de la gran mayoría de las actividades que se llevaron a cabo en el proyecto. Le agradezco por toda la *paciencia*, apoyo y comprensión con los que nutrió mi persona durante años. Por que si esta etapa tuviera nombre, sería el de ella.

A mis amigos en el IMUNAM, Mónica, César, Oswaldo y todos los del ente autodenominado como ”El Cubo”.

A mis amigos en general, gracias por tanto y perdón por tan poco.

A la comunidad IPICYT de todas y cada una de las divisiones.

Al personal y alumnos, de la UPZ, UAZ e IPN, por tener siempre consideración y apoyo al proyecto.

Al Comité Tutoral por el tiempo que han dedicado para revisar la tesis y por sus aportaciones a la misma.

Al Instituto de Matemáticas de la UNAM (IMUNAM) por su valiosa participación, formación, paciencia y hospitalidad. Siempre será una segunda casa.

Al Proyecto SEP-CONACYT Ciencia Básica 286626, así como al CONACYT por la beca 297370.

Al Proyecto Ciencia de Frontera CONAHCyT CF-2023-G-122.

Contents

List of Figures

Chapter 1

Introduction

1.1 Background and motivation

At the moment there is a great demand by industry on ferromagnetic materials due to their properties. Specially nonhomogeneous ferromagnetic materials is a subject with growing interest. Therefore, there is a necesity to understand and foretell the behaviour of the properties of such materials. The above is completed by means of numerical methods. But also, there is an issue in this task: as the size of the sample becomes bigger the cost of a numerical simulation increases and becomes a lock in the investigation in this matter.

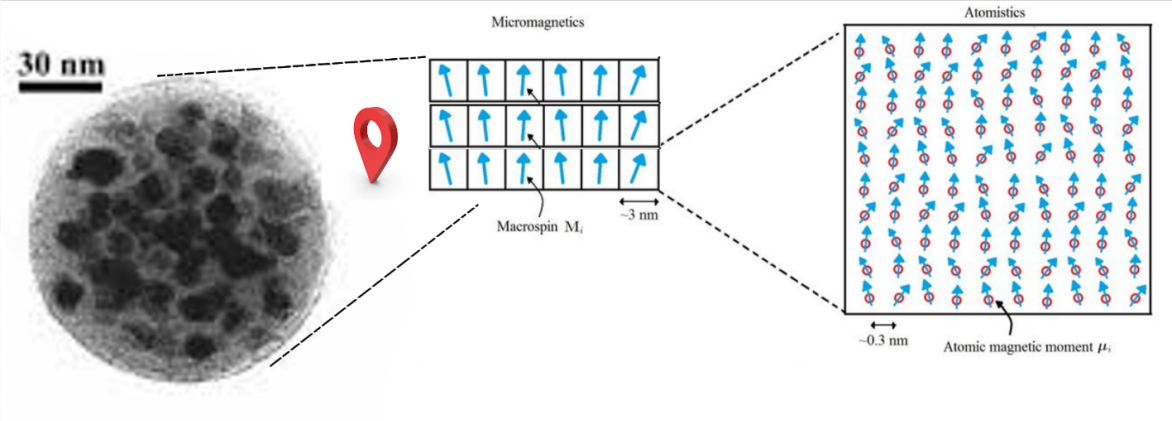

Figure 1.1: Sketch representing the positioning of the model with respect to the other theories.

As far as we know [12] there are four ways to study magnetic materials. The first one is the *atomistic approach* which uses quantum mechanics to study the properties of magnetic

materials in an atomic scale (rightmost picture of Figure 1.1). This can be used to analize the effects of impurities in materials. The second is the *macroscopic approach*. This theory considers the magnetic material as a bulk object and uses classical electrodynamics to determine the properties of the material (leftmost picture of Figure 1.1). This can be useful to study materials with simple geometries but it fails when it comes to study nanomaterials as it can not see the interactions between particles. On third place we have the *micromagnetic approach* wich takes into account the atomic structure and the magnetic interaction between particles (center picture of Figure 1.1) but this approach fails as one wants to study systems above the mesoscopic scale as the computing cost gets bigger. Finally, we have the *Multi-scale approach*, which combines different approaches to study magnetic materials at different length and time scales.

This thesis proposes the combination of the micromagnetic approach and homogenization techniques to create and intermediate approach which can foretell the properties of a bulk material taking into account the geometry of the nanoparticles present in the material and the interaction of such arrangement of magnetic particles. This is done two ways: the first, is to develop a mean-field model which describes the effective magnetostatic anisotropy. This approach is created under the assumption that the material is made up of a very large number of identical spherical particles enclosed in some finite volume V. This allow us to compute the mean values of the main magnetic parameters of such a system ignoring some factors of the microstructure. But also, this set of conditions are quite strong restrictions to the systems that can be studied with this mean-field model. Therefore, there is a need to develop a more general procedure that could tackle a broader set of systems. This is done by means of homogenization techniques. Particularly, we use the asymptotic homogenization technique and the two-scale homogenization approach to get a generalized model that computes the main properties of a magnetic system based on a sample region (cell) of the material which contains the geometry, and volume fraction of the magnetic particles in the cell.

All the above, will serve to predict the characteristic of magnetic nanomaterials which in turn will reduce the number of experimental samples that must be created and characterized. Also, with the ability to numerically simulate materials of this kind, one can also determine the final configuration of the magnetization due to certain initial state of the sample.

1.2 Hiphothesis

We are certain that we can create a numerical scheme based on the minimization of the micromagnetic energy and the Finite Element Method (FEM) studied under a model crafted with partial differential equations in weak form. This scheme will be capable of computing the hysteresis curves of a cell which contains a finite number of magnetic particles with arbitrary geometry subject to Dirichlet, Robin or periodic boundary conditions.

Also, we can predict the main properties of magnetic systems with a mean-field model for systems composed of a large number of spherical particles and, for more arbitrary systems, we can use a scheme based on the homogenization techniques what will determine an operator which determines the demagnetization field based purely on the geometry and arrangement of the magnetic particles in a cell.

1.3 Objectives and scope of the thesis

General objective:

- Create the numerical scheme that determines the hysteresis curve of some magnetic material based on the geometry and accomodation of the particles in a cell.
- Develop a mean-field model capable of determining an analytical expression for the effective magnetic anisotropy for a system made of a large number of identical spherical particles.
- Obtain an operator that computes the demagnetization field based on the geometry of the sample using homogenization techniques.

Specific objetives

1. Set the micromagnetic energy for a system of N particles with constant magnetization vector.
2. Use the boundary conditions to formulate the weak formulation of the problem.
3. Use the lagrange multipliers technique to find the direction in which the energy descends.

4. Use a line search algorithm to find the minimum energy for the actual configuration.
5. Code all of the above on *FreeFem++*.
6. Test the code.
7. Analyze the effects of the geometry and arrangement of the particles.
8. Develop a mean-field model based on the clustering of some lattice repeated in space to form a larger system.
9. Obtain the total magnetic anisotropy for the system above mentioned.
10. Use the two-scale homogenization technique to determine an expression for the demagnetization field.
11. Apply the numerical scheme to magnetotactic bateria and observe the results.
12. Apply the numerical scheme to arbitrary geometries and observe the results.

1.4 Contribution to the field

The present investigation will contribute in two ways: first, with an open source code which includes the numerical scheme mentioned above. This code will be written in *FreeFem++* and published on Github for future generations to use, study and contribute. This code shall be published under a creative commons of GNU license. Second, this investigation will culminate with the publication of scientific papers with the detailed procedure on how to obtain the numerical scheme, how to use the code to study several systems of interest and how to apply the two-scale homogenization to obtain properties of a material with periodic boundary conditions.

Chapter 2

Literature review / State of art

2.1 Overview of micromagnetics

Magnetism in an natural phenomenon that we perceive with normality in daily life but no always has been this way. The history of magnetism dates back to ancient times, the first record of magnetism in history is from chinese literature around 4000 B.C. where is mentioned that magnetite was used as a primitive compass [13]. Over the years, the comprehension of magnetism has evolved with the efforts of numerous scientists.

One of the earliest recorded mentions of magnetism can be traced back to Greece, where the ancient philosopher *Thales of Milletus* noted that some special stones (lodestone) had the abilty to pull small pieces of iron from a certain distance. This lodestone was found in the region of *Magnesia* and because of this the magnets get its name. From here, there was no formal study in this phenomenon until the 16th century when Sir William Gilbert, at a the service of the Queen Elizabeth I, published the first scientific work on the subject of this materials [14]. His investigation was published in the book ”De Magnete” in which Hilbert describes the results of the first experiments with magnets and the term ”magnetism” is introduced to the scientific community.

It was until the 19th century that magnetism was studied with academic rigor, with the discovery of new magnetic materials and the development of experimental techniques. It is in this time when *Michael Faraday* discovered the electromagnetic induction in 1831. Faraday showed that the change in some magnetic field could induce an electrical current in copper wire if the wire was near the source of the variable magnetic fied. This fact is, until today, the basis of the electrical generators and motors. In the same century, James Clerk Maxwell

formulated its famous set of equations, creating the theory that unified the electricity and magnetism. This set of equations, henceforth known as the Maxwell's equations, described the demeanor of electric and magnetic fields and the relation between them. These equations also predicted the existence of electromagnetic waves which in time became the foundations for the development of the radio, television, and signal transmission [15].

Later in the 20th century, magnetism gathered the atention of the scientific community with the discovering of the ferromagnetism: the phenomenon in which a non-magnetic material can become permanently magnetized, this was the begining of the creation of neodymium magnets. Ampere suggested that the ferromagnetism was due some internal electric currents inside the material. This idea had be proven correct on and carried out by W. E. Weber in the 19th century. Weber assumed that the molecules of iron could be capable of move around their own axis, and this would be equivalent to a current flowing around a circular spire creating a tiny magnetic moment but, in the case of iron, the molecules lied in configuration such that every magnetic moment was neutralized with the moment of the other molecules. Then, under the application of an external magnetic field, the magnetic axis of each molecule aligns itself with the external magnetic field. This results in the magnetization of the iron as happens in the experiments [16].

From here, we aim to study magnetic materials in a microscopic scale therefore a subfield of magnetism was requiered: the micromagnetism. The earliest work in this subject was due to Pierre-Ernest Weiss. His investigation was published in 1907 and coined the concept of the "molecular field theory" which describes the interaction between the atomic magnetic moments of in the material. This was the basis for the magnetic domains: regions of a material where the magnetic moments of the atoms are aligned in the same direction [17].

Later, there were numerous scientists [18] that contributed to the field but the most important between them where *Felix Bloch* (1930), who coined the "Bloch wall model" which describes the behaviour of domain walls; and *Andrei Sakharov* (1950) who studied the importance of the thermal fluctuations over the magnetic properties of magnetic materials [19]. On the other hand, the first studies in micromagnetism based on numerical methods date from the year 1960 when the development of computers led to the growth of new models and theories which explained the stability of the magnetic domains and the response of magnetic domains under a pulse of field [20].

Nowadays, the magnets have a significant role in technology as we have found many applications to this materials. We use magnets to transform mechanical energy into electrical energy by using motors and transformers; to store data inside hard drives; to transform mechanical vibrations into electrical signals with a microphone or we can transform electrical energy into mechanical vibrations with a loudspeaker. Among this applications we are Particularly interested in the ones that the computation has brought as the requirement of larger data storage devices began to grow. In general, the magnetic storage devices such as hard drives rely on tiny magnetic elements which store only a single bit of information. There-

fore, the writing speed of these devices depends on the magnetization switching time. This stands for an intensive understanding of the magnetization process and mechanisms in order to design new and better data storage devices [21]. In this fashion, the model and simulation of magnetic media can provide reliable information about magnetic systems without creating every new material that comes to mind. Respec to this, the present thesis is an effort to build a numerical scheme capable of determining magnetic properties of a system of N magnetic nanoparticles with arbitrary shape. Then, as we propose periodical boundary conditions, the numerical scheme wil be capable of calculate the properties of a bulk material with an atomic structure given by the structure of one cell allowing us to accurately predict the properties of think films made of a regular array of magnetic nanoparticles.

2.2 Elements of partial differential equations in weak form

A partial differential equation, in few words, is a mathematical model that represents or describes a physical phenomenon that vary over time and/or space. This kind of equations can be classified by its order, linearity and the number of variables in the equation. There are only a few of this partial differential equations (PDE) that can be solved analytically and therefore are the most known [22]. Some of this cases will be presented next.

2.2.1 The variational formulation

So far, we have seen that the study of partial differential equations is focused on finding unknown functions that satisfy some differential equations subject to certain conditions. In general, differential equations are mathematical models that represent a phenomena. Now, if the interesting variables of a system are time dependent then we say that the differential equation with the initial condition is a *Initial Value Problem* (IVP). On the other hand, if the variables of the system are time independent then the differential equation depends only on the coordinates and the variables of interest. In this case, we say that the differential equation with the conditions established on the frontier conforms a *Boundary Value Problem* (BVP). The solution to this kind of problems is not possible except for some explicit cases. Therefore, we must find the solution to the majority of these problems by approximation methods [23]. Although there is a variety of this methods, in this work we may focus in the *Finite Element Method* (FEM). This method is used to find the solution of partial differential equations in both time dependent and time independent problems. The method consist on the discretization of the workspace by constructing a mesh made of smaller pieces called *elements*, this elements can be constructed with a shape and size that is convenient to system's study. Later we select a function for interpolation and with this function as a basis we determine the *weak form* (or variational formulation) of these problems. As for understanding

what a weak formulation is, we are going to need the support of some concepts of functional analysis.

Definition 2.2.1 (Set)**.** Is defined as an ensemble of things that share some property. An open set is a set that does not contain the boundary points and a closed set is one that already contains the limit points.

Definition 2.2.2 (Space)**.** A set that can be spanned as a linear combination of the elements of the set (a basis) is called a Space. The number of elements that conforms the basis determines the dimension of the space.

Definition 2.2.3 (Vector Space)**.** a.k.a. *Linear Space* is a space that satisfies the conditions of closure under addition and multiplication. Furthermore, a vector space must satisfy the conditions of: commutativity, associativity, additive identity, additive inverse, distributivity of scalars under sum and multiplication and scalar multiplication identity [24].

Definition 2.2.4 (Linear Relation)**.** Let S be a linear space, and $u_i \in S$, and $\alpha_i \in \mathbb{R}$. Then, a mathematical expression of the form

$$\sum_{i=1}^{n} \alpha_i u_i \in S$$

is a linear combination of u_i. And finally, an equation that has the form

$$\sum_{i=1}^{n} \alpha_i u_i = 0$$

is said to be a linear relation.

Definition 2.2.5 (Finite-dimensional Space)**.** A linear space S is a *n-dimensional* space if and only if, there exist n linearly independent elements in S.

Definition 2.2.6 (Function)**.** Let $f(x), x \in \Omega = [a,b]$, then f is a mapping that relates every element in its domain Ω with one and only one element in another set (its range) R. Regularly, this is written as $f : \Omega \to R$.

Definition 2.2.7 (Metric Space)**.** Let S be a linear space such that $a,b,c \in S$. Then, we can define the distance between any two elements of S as $d(a,b)$. Finally, S is a metric space if the following conditions are satisfied:

$$\begin{aligned} &i) \quad d(a,b) = d(b,a) \\ &ii) \quad d(a,c) \leq d(a,b) + d(b,c) \quad \text{Triangle inequalty} \\ &iii) \quad d(a,b) \geq 0 \\ &iv) \quad d(a,b) = 0 \Leftrightarrow a = b \end{aligned} \tag{2.1}$$

And the combination of the linear space S and the metric $d(a,b)$ is a metric space denoted by (S,d)

Definition 2.2.8 (Normed Space)**.** Let S be a linear space such that $u_i \in S$. Also, let us define the norm of u_i as a real number denoted by $||u_i||$. This norm satisfy the following

$$\begin{aligned} &i) \quad ||\alpha u|| = |\alpha||u| \quad \forall \alpha \in \mathbb{R} \\ &ii) \quad ||u+v|| \leq ||u|| + ||v|| \\ &iii) \quad ||u|| \geq 0 \\ &iv) \quad ||u|| = 0 \Leftrightarrow u = 0 \end{aligned} \tag{2.2}$$

Definition 2.2.9 (Strong/Norm convergence)**.** Let (V,d) be a metric space and $\{u_i\} \subset V$ a sequence. Then, we say that $u_0 \in V$ is the limit of $\{u_n\}$ as n goes to infinity if for every $\varepsilon > 0$ there exist $n_0 \in \mathbb{N}$ such that if $n > n_0$, then $d(u_n, u_0) < \varepsilon$. While all of this is true we can say that

$$\lim_{n\to\infty} u_n = u_0$$

or

$$u_n \to u_o \quad \text{as} \quad n \to \infty.$$

And finally we can say that $\{u_n\}$ is (strongly) convergent. In simple words: a sequence is strongly convergent, if as $n \to \infty$ the sequence goes to a certain element inside the same linear space. This is, the sequence gets close to some $u_0 \in V$ as $n \to \infty$.

Definition 2.2.10 (Cauchy Sequence)**.** Let (V,d) a metric space and $\{u_i\} \subset V$ a sequence. The sequence shall be called a Cauchy sequence if for every $\varepsilon > 0$ exist some $n_0 \in \mathbb{N}$ such that if $m,n > n_0$, then

$$d(u_n, u_m) < \varepsilon.$$

This is, after some element of the sequence indexed by n_0 we can always draw a circle centered around u_n and the circle will be completely contained in V.

Definition 2.2.11 (Complete metric space)**.** Let (V,d) be a metric space. Then, the metric space will be complete if and only if every Cauchy sequence in V converges to an element in V.

Definition 2.2.12 (Banach Space)**.** A Banach space B is a complete metric normed space. Recall that every metric space is a normed space but not every normed space is a metric space.

Definition 2.2.13 (Inner Product Space)**.** Let $S \mid x,y,z \in S$ be a linear space. Then, we can define an inner product (x,y) that maps every pair x,y to a real number. This product will satisfy

$$\begin{aligned} &i)(x,y) = (y,x) \\ &ii)(ax+by,z) = a(x,z) + b(y,z) \quad \forall a,c \in \mathbb{R} \\ &iii)(x,x) \geq 0 \\ &iv)(x,x) = 0 \Leftrightarrow x = 0 \end{aligned} \tag{2.3}$$

Definition 2.2.14 (L^p Spaces)**.** Let $1 < p < \infty$. Then, if $u : \Omega \to \mathbb{R}$ is measurable and

$$\int_\Omega |u|^p dx < \infty.$$

Then, $u \in L^p(\Omega)$.

Definition 2.2.15 (Hilbert Space)**.** It is a name for a complete inner product space.

Definition 2.2.16 (H^k Space)**.** Let $H^0(\bar{\Omega}) = L_2(\bar{\Omega})$ be a space of square-integrable functions defined over some $\bar{\Omega}$ Then, we can define H^k spaces as a space of functions whose kth derivative exist and are square-integrable. It is remarkable that H^0 is the bigger and less restrictive space among these.

Definition 2.2.17 (Sobolev Spaces)**.** We begin by denoting this spaces by $W^{m,p}(\Omega)$ and let $D^i u$ represent the ith derivative of u. Then, we say that a function $u \in W^{m,p}(\Omega)$ if the following conditions are both satisfied:

- $u \in L^p(\Omega)$
- $D^\alpha u \in L^p(\Omega)$

where p represents the integrability of the power and m represents the maximum derivative that exist in such a space.

Definition 2.2.18 (Weak derivative)**.** Let $\phi \in \mathcal{C}_c^1(\mathbb{R})$ and $a > 0$ such that $supp(\phi) \subset [-a,a]^n$. Then by the fundamental theorem of calculus we know that

$$\int_{-a}^{a} \frac{\partial \phi}{\partial x_i}(x_i, \hat{x}) dx_i = \phi(-a, \hat{x}) - \phi(a, \hat{x}) = 0,$$

and by consequence

$$\int_\Omega \frac{\partial \phi}{\partial x_i} = \int_{\mathbb{R}^{n-1}} \int_{-a}^{a} \frac{\partial \phi}{\partial x_i}(x_i, \hat{x}) dx_i = 0.$$

With this in mind, let us apply the same procedure to the product $(f\phi) \in \mathcal{C}_c^1(\Omega)$ to obtain

$$\int_\Omega \frac{\partial (f\phi)}{\partial x_i} = \int_\Omega \frac{\partial f}{\partial x_i}\phi + \int_\Omega f \frac{\partial \phi}{\partial x_i} = 0$$

The last equation motivates the definition of weak derivative as follows: let $u \in L^p(\Omega)$ then, u is weakly differentiable in Ω if there exist some $v_1, ..., v_n \in L^p(\Omega)$ such that

$$\int_\Omega u \frac{\partial \phi}{\partial x_i} + \int_\Omega v_i \phi = 0 \quad \forall \phi \in \mathcal{C}_c^\infty(\Omega),$$

for any i. In this context, v_i is called the ith weak derivative of u in Ω such that $D_i u := v_i$

Theorem 2.2.1 (Gradient Theorem)**.** States that the line integral of a gradient field can be evaluated by calculating the integral of the original scalar field at the endpoints of the curve. This is

$$\int_{\Omega} \nabla \phi dx dy dz = \oint_{\Gamma} \hat{n} \phi ds$$

Theorem 2.2.2 (Divergence/Gauss Theorem)**.**

$$\int_{\Omega} \nabla \cdot \phi dx dy dz = \oint_{\Gamma} \hat{n} \cdot \phi ds$$

Proposition 2.2.1 (Integration by Parts)**.** This is a calculus technique that allows to transfer differentiation from one function to another by means of an integral representation. This is also an integration technique that is allow us to rewrite the integral of a product of two functions $(u, v) \in \mathcal{C}^1$ as

$$\int_a^b u dv = [uv]_a^b - \int_a^b v du.$$

Also, combining definitions (2.2.1, 2.2.2) we can get to these useful forms of the integration by parts. On the case of a partial derivative of first order we get

$$\int_{\Omega} (\nabla \phi) \psi d\Omega = -\int_{\Omega} (\nabla \psi) \phi d\Omega + \oint_{\Gamma} \hat{n} \phi \psi ds.$$

And on the case of a second order differential operator we can write

$$\int_{\Omega} (\nabla^2 \phi) \psi d\Omega = -\int_{\Omega} \nabla \phi \cdot \nabla \psi d\Omega + \oint_{\Gamma} \frac{d\phi}{dn} \psi ds$$

The above definitions are not intended to be a express course of mathematical analysis, although this definitions can result useful to give context to some concepts that are recalled later in this work. If the reader is interested in this topic, all of the above come from [23, 25–27]

In spite of giving some context on the use of the integration by parts to change the form of an equation we will show some examples next. Consider an operator $A : S \subset H^1(a,b) \rightarrow H^0(a,b)$ such that

$$A\phi = -\frac{d\phi}{dx}, x \in (a,b).$$

Where we can name the domain $\Omega = (a,b)$ and the boundary of that domain as $\Gamma = \{a,b\}$. Later, we can use the typical definition 2.2.1 to this product to get

$$(A\phi, \psi) = -\int_a^b \frac{d\phi}{dx} \psi dx = \int_a^b \phi \frac{d\psi}{dx} dx + [\phi\psi]_a^b.$$

As you can see, as we integrate by parts the derivative operator goes from ϕ to ψ at the cost of adding the extra term $[\phi\psi]_a^b$. This extra term is called *concomitant*.

Now, let us consider an operator $A : S \subset H^2(a,b) \to H^0(a,b)$ such that

$$A\phi = \frac{d^2\phi}{dx^2}.$$

Then we can use integration by parts to do the following

$$\int_a^b \frac{d^2\phi}{dx^2}\psi dx = \left[\psi\frac{d\phi}{dx}\right]_a^b - \int_a^b \frac{d\phi}{dx}\frac{d\psi}{dx}dx,$$

and if we do the same process to the integral on the right hand side

$$\left[\psi\frac{d\phi}{dx}\right]_a^b - \int_a^b \frac{d\phi}{dx}\frac{d\psi}{dx}dx = \int_a^b \phi\frac{d^2\psi}{dx^2} + \left[\frac{d\phi}{dx}\psi - \phi\frac{d\psi}{dx}\right]_a^b.$$

In this case, by applying twice the integration by parts to the operator acting over some ϕ we change the operator from ϕ to ψ and appears a concomitant which is the term in brackets.

Finally we consider an operator in two dimensions. Let $A : S \subset H^1(\Omega) \to H^0(\Omega) \mid \Omega \subset \mathbb{R}^2$ such that

$$A = \frac{\partial}{\partial x} + \frac{\partial}{\partial y}.$$

Later we can rewrite the following integral as

$$\int_\Omega \left(\frac{\partial\phi}{\partial x} + \frac{\partial\phi}{\partial y}\right)\psi d\Omega = -\int_\Omega \phi\left(\frac{\partial\psi}{\partial x} + \frac{\partial\psi}{\partial y}\right)dxdy + \oint_\Gamma (n_x + n_y)\phi\psi d\Gamma.$$

Where we have used the last equations on definition (2.2.1) to change the integral over Ω to be over the boundray Γ. As in the prior examples, we used the integration by parts technique to modify the form of the equation. As usual, we pass the partial derivatives from ϕ to ψ and the concomitant term appears in terms of n the normal to the boundary Γ.

Now that we have collected the concepts and definitions required, we can approach to the main topic of this section: the weak formulation of a partial differential equation. Generally, when we want to solve a problem numerically, we need to approximate the solution by using a subspace of $H^1(\Omega)$ spanned by a set of basis functions associated to a mesh representing a virtual space. This task could be complicated if we try to solve it in *strong form*. Here is where the weak form becomes interesting. The weak formulation is a way to transfer the concepts of linear algebra to solve a problem in differential equations. To illustrate this concept let us study a simple case as follows:

Suppose we have a problem involving a differential operator as $-\nabla(a(x)\nabla u(x)) = f(x)$. As we use the integration by parts technique we achieve the weak (variational) form of the problem. Then, let $\{\psi_n \mid n = 1,...,N\}$ be a set of linearly independent functions that lay in $H_0^1(\Omega)$. This set of functions clearly span an N-dimensional subspace $V_N \subset H_0^1(\Omega)$. To solve this, we need to find some $u \in H_0^1$ such that

$$\int_\Omega a(x)\nabla u(x)\cdot\nabla v(x)dx = \int_\Omega f(x)v(x)dx \quad \forall v \in H_0^1(\Omega).$$

The next step will be to seek an approximate solution

$$u = \sum_{n=1}^{N} u_n\psi_n \mid u \in V_n.$$

In this way, we just need to test u against every $v \in V_n$ and not to every $v \in H_0^1$. Now, to this end we can propose

$$v = \sum_{m=1}^{N} u_m\psi_m \mid u \in V_n.$$

Taking u and v as series, then the integral equation can be rewritten as

$$\sum_{n=1}^{N}\sum_{m=1}^{N} u_n v_m \int_\Omega a(x)\nabla\psi_n(x)\cdot\nabla\psi_m(x)dx = \sum_{m=1}^{N} v_m \int_\Omega f(x)\psi_m(x)dx.$$

And later, we consider that $v = \psi_k \quad \forall \quad k = 1,...,N$ so $v_k = \delta_{m,k}$. Therefore,

$$\sum_{n=1}^{N} u_n \int_\Omega a(x)\nabla\psi_n(x)\cdot\nabla\psi_m(x)dx = \int_\Omega f(x)\psi_m(x)dx.$$

This becomes a system of equations of $N \times N$ represented by

$$\mathbf{A}\vec{u} = \vec{b},$$

where

$$\begin{aligned}
\mathbf{A} &= \int_{\Omega} a(x)\nabla\psi_n(x)\cdot\nabla\psi_m(x)dx \in \mathbb{R}^{N\times N},\\
\vec{u} &= u_n \in \mathbb{R}^N,\\
\vec{b} &= \int_{\Omega} f(x)\psi_m(x)dx \in \mathbb{R}^N.
\end{aligned}$$

And as we can recognize, this is merely a problem of linear algebra, as desired [28].

2.3 Asymptotic homogenization

First, let us start with the concept of homogenization. In general, the idea of homogenization allow us to upscale a differential equation model. For example, if a certain volume Ω of a material has a certain physical property that depends on the coordinates and it is represented by $f(x)$. In addition, let us say that this property oscillates rapidly over some representative sample of the material. What one would do, experimentally, is to take several measurements over this representative sample and then report or assume the most likely result (the average maybe). If we have some mathematical representation of the property, then we just report that the value of the property in Ω is given by

$$\bar{f}(x) = \int_{\Omega} f(x,y)dy.$$

In this case, we propose that the oscillations of $f(x)$ show the behavior of the *microscale* of the material, represented by the variable y while $\bar{f}(x)$ describe the properties of the material in the *macroscale*. And as a concept the homogenization has the same spirit but it has a more strict mathematical sense.

The process of homogenization begins with the selection of a representative elementary volume (REV). Then we work not with only one function $f(x)$ but with a whole family of functions u^{ε} where $\varepsilon > 0$ is a scale parameter which depends on the spatial coordinates and typically ε is associated with the length of an individual cell of the material. With this in mind, the function u^{ε} let us analyze a family of problems associated with each ε in a sense

that every one of these represent the properties of the material at a different scale. This can be seen in the figure 2.1.

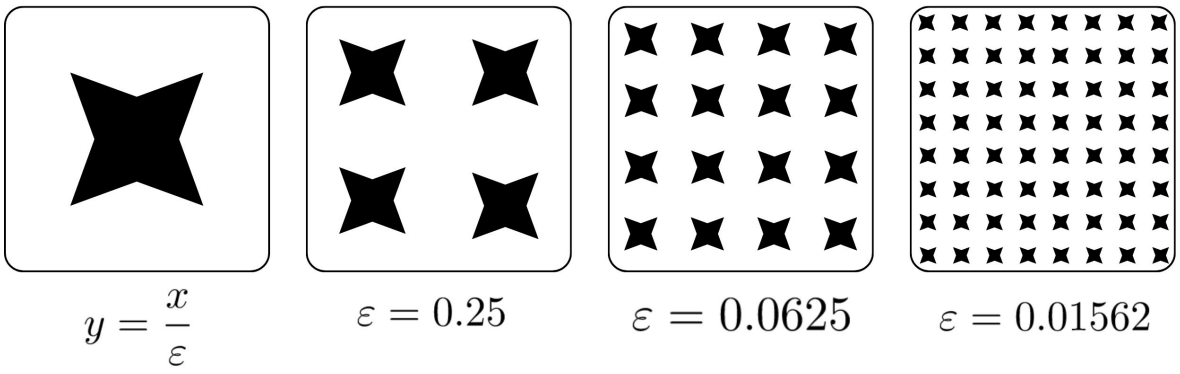

Figure 2.1: Sketch of how ε represents different scales on the material. This is, calculating u^{ε} we can obtain the property at the desired scale of the material.

2.3.1 Example of homogenization in 1D

To illustrate the process we are going to considerate some simple configurations. In this case, we shall consider a one-dimensional diffusion problem where u is the variable of interest and it is defined in some $\Omega = [0,1]$. Then the boundary value problem will be written as

$$\begin{cases} \frac{d}{dx}\left[a(x)\frac{d}{dx}u(x)\right] = 0, \quad 0 < x < 1, \\ u(0) = 0, \\ u(1) = 1. \end{cases} \tag{2.4}$$

From the first equation it is clear that $a(x)u'(x)$ must be constant (that we call Q) and therefore

$$\frac{d}{dx}u(x) = -\frac{-Q}{a(x)}, \tag{2.5}$$

and we can solve this equation to get

$$u(x) = -Q \int_0^x \frac{1}{a(x)} dx, \tag{2.6}$$

and when we consider the boundary conditions this is rewritten as

$$u(x) = \frac{-1}{\int_0^1 a(x)dx} \int_\Omega a(x)dx. \tag{2.7}$$

In this example, we have obtained the quantity $u(x)$ and, as a collateral effect, we also have the diffusion constant characterized by Q. This is the spirit of the homogenization technique. The function $a(x)$ represent a non-homogeneous property of the material (diffusion for this case) and the parameter Q is the effective diffusion in this medium. Note that Q depends on the function that we already know in the cell region, whereas the $u(x)$ depends on both, the cell region and the Ω region over we want to compute the parameter.

Now, with mere descriptive purpose let us modify the problem to this version

$$\begin{cases} \frac{d}{dx}\left[a^\varepsilon(x)\frac{d}{dx}u^\varepsilon(x)\right] = 0, \quad 0 < x < 1, \\ u^\varepsilon(0) = 0, \\ u^\varepsilon(1) = 1. \end{cases} \tag{2.8}$$

Such that every problem will be indexed by the scale parameter $\varepsilon = 1/n$ and the functions $a^\varepsilon(x) = a(\frac{x}{\varepsilon})$ and $u^\varepsilon(x) = u(\frac{x}{\varepsilon})$ are such that have periodicity of length 1. In particular, this fact can be interpreted as that the functions $a^\varepsilon(x)$ are oscillatory functions with increasing frequencies as $\varepsilon \to 0$. If we apply the same procedure as before we obtain a solution that can be written as

$$
\begin{aligned}
u_0^\varepsilon(x) &= \frac{1}{\int_0^1 \frac{dx}{a^\varepsilon(x)}} \int_0^x \frac{dx}{a^\varepsilon(x)} \\
u_0^\varepsilon(x) &= \frac{1}{\int_0^n \frac{dy}{a(y)}} \int_0^{nx} \frac{dy}{a(y)} \\
u_1^\varepsilon(x) &= x + \frac{1}{\int_0^n \frac{dy}{a(y)}} \int_0^{nx} \left(\frac{1}{a(y)} - 1 \right) dy \\
u^\varepsilon(x) &= x + \varepsilon \frac{\int_0^1 \frac{d\hat{y}}{a(\hat{y})}}{\int_0^1 \frac{d\hat{y}}{a(\hat{y})}} - \varepsilon y
\end{aligned}
\tag{2.9}
$$

This can be rewritten as

$$
u^\varepsilon = u(x) + \varepsilon u_1(x/\varepsilon), \tag{2.10}
$$

where $u(x) = x$ and $u_1(x/\varepsilon)$ is a periodic function (1-periodic indeed). Here we can observe that $u(x)$ describes the global or macroscopic behavior of u^ε and $u_1(x/\varepsilon)$ is a correction term that adds the local oscillations of $u^\varepsilon(x)$. For further information and formal description of this process, one can go to [29–32].

2.4 Previous works / State of art

2.4.1 Numerical scheme in micromagnetism

The principal aim of this work is to develop a solid numerical scheme that is capable to compute the macroscopic properties of system of magnetic particles by knowing the microscopic structure of the material. As a way to contextualize the reader of the place that this research has in the field, this section will collect the articles that are related and accompany the present research.

According to [33, 34] the field of the computational micromagnetics is divided in two major fields: static micromagnetics and dynamic micromagnetics. The static micromagnetics is the branch that finds a set of stable magnetization of the particles such that the total free energy E of the system is (at least) in a local minimum with respect the magnetization *vecm*. This model is useful to compute some properties of magnetic materials such as the

hysteresis curves. On the other hand, dynamic micromagnetics makes use of the *Landau-Lifshitz-Gilbert* (LLG) equation which describes the spatial motion of the magnetization in some effective field.

Independently of the model that we use to describe some system, we have to deal with a set of non-linear partial differential equations whose analytical solution exist just for a few simple cases. In general, the solution of static and/or dynamic micromagnetics recall for numerical methods. The most popular numerical methods in micromagnetics are two: the *Finite Difference Method* (FDM) and the *Finite Element Method* (FEM).

In the case of the FDM we have several software packages that already exist such as OOMMF [35], Fidimag [36], Micromagus [37], a very creative implementation of numpy and python [38], Mumax3 [39] and magnum.fd [40]. All of the above mentioned software are based on the FDM and deals with the dynamic version of the micromagnetics.

On the other hand, we have the FEM where we need to solve a system of partial differential equations but instead of make the original problem discrete we need to transform the problem to its variational (weak) form and then discretize this form. In this context we have even more software packages but most of these packages are not oriented specifically to the field of micromagnetics but are a set of libraries that allow us to solve any problem of partial differential equations by means of the FEM. This is quite convenient as opens the boundary to solve not only micromagnetics but anything one can think about. In this respect the most popular software is: Escript [41], MFEM [42], FEniCS [43] and are the basis to construct software that really focuses on magnetism such as Magpar [44] , Nmag [45], Tetramag [46], Fastmag [47].

Now, in general, every one of this packages has advantages and unique characteristics but also each one has its flaws. In brief: Escript, MFEM, and FEniCS are not designed specifically to treat with micromagnetics and due to this, solve a problem of magnetism in this environment needs intermediate knowledge of programming and has a steep learning curve. Also, the discretization of the space into a mesh of finite elements has to be made in external packages which could deepen the learning curve. Fortunately we have the specialized software as Magpar, Nmag, Tetramag and Fastmag. To analyze the opportunities of each of these programs we shall do it one by one. In first place Magpar has a process of installation that is not straightforward and despite of being free of cost, it could be difficult to compile and use; Nmag is an exceptional software that makes use of a large set of tools but it is designed to work on unix based operative systems. This, of course, indicates that the user must have a previous knowledge of this platforms and how to set up and install libraries from scratch. Tetramag and Fastmag are, as well, very powerful tools but both are designed to run over the graphic unit processors (GPU) which, once again, indicates that is not suitable for a non hardcore user and that you need to have a recent GPU and know how to use it.

Therefore, there is a need to create an implement a numerical scheme that is multi-platform, open source, free and easy to install and use for the casual users. This is the aim of this research as to develop this scheme and analyze further examples and cases which, luckily, will inspire the community to develop and cherish new functions, codes, and knowledge over the properties of magnetic materials.

2.4.2 Asymptotic homogenization method in material's science

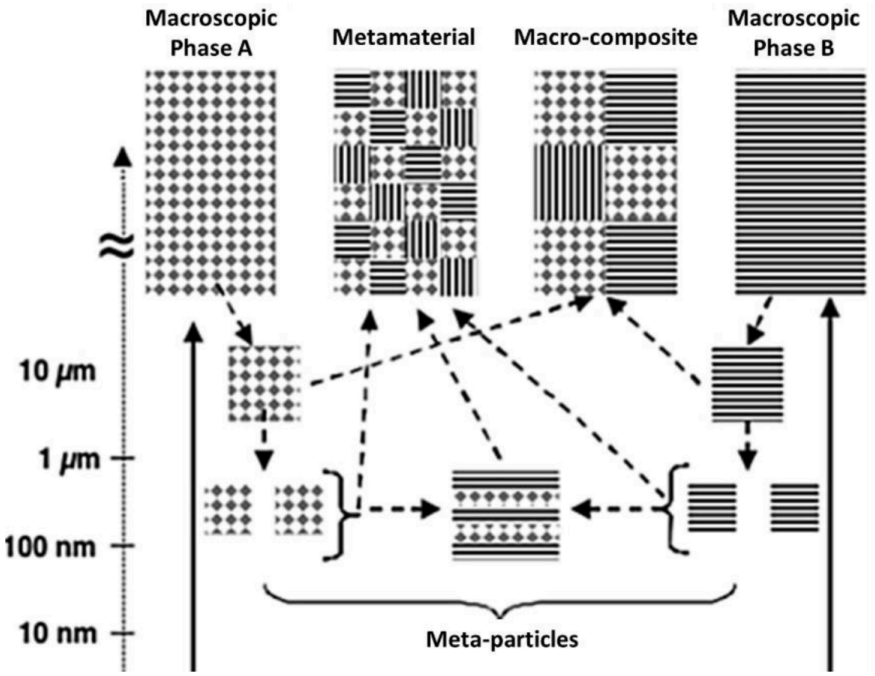

Figure 2.2: Metaparticles and its accomodation in some scales of length [1]

Now, on the subject of homogenization we can find that there is large research field. As new technologies appeared, new ways to construct materials became available. This led to novel ways of thinking of materials: how these are fabricated and the properties that the material could have if the microstructure is carefully chosen. Eventually this leads to the study of metamaterials with a very precise geometry, then appeared the study of the combination of these geometries and the effect that could have in the bulk properties [48]. What is said above can be visualized within figure 2.2.

In a field as wide as material's science there are a lot of applications to the concept of homogenization such as biomedicine [49], acoustics [50], metamaterials [51], composites [52], wave propagation [53, 54], mechanical properties [55] and even turbulence modeling [56]. A great compilation of all this applications and configuration problems can be found in [57]. However, as far as we could inquire in the subject, there a few work related to the

magnetic properties of materials [58–62]. Between these works the most interesting to our ends can be found in [63].

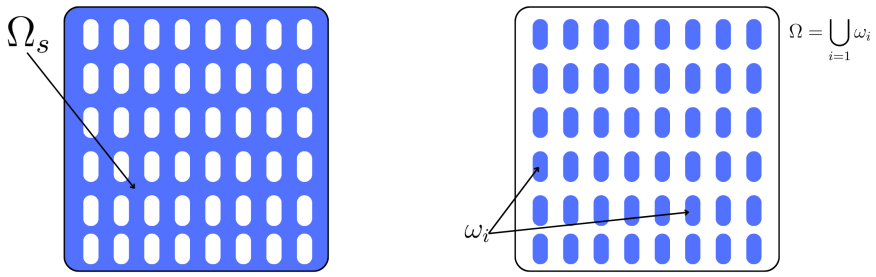

Figure 2.3: Comparison of the geometries. Left: perforated magnetic medium. Right: assemble of magnetic particles inside a cell.

In this thesis, the author study the homogenization of the demagnetization field operator in periodically perforated domains using a two-scale convergence method. This problem is the geometric complement of the problem that we solve in this research, as we can see in figure 2.3. Although the problem is quite similar, the procedure to solve the problem and the solution of it is very different. For the problem of the perforated domains the most remarkable result is an homogenized form of the demagnetization field operator, denoted by $\vec{H}_d$. This homogenized demagnetization field operator turns out to be (3×3) matrix whose elements are given by

$$[\vec{H}_d]_{ij} = \frac{1}{\bar{\chi}} \int_y (\nabla \omega_i'(\vec{y}) + \chi y^*(\vec{y}) \vec{e}_i) \cdot (\nabla \omega_j'(\vec{y}) + \chi y^*(\vec{y}) \vec{e}_j) d\vec{y} - \delta_{ij}. \tag{2.11}$$

Which is used later in the paper to homogenize the LLG equation.

Chapter 3

Theoretical framework

3.1 Notation and definition of the problem

So far, we know that the classical electromagnetic theory developed by Maxwell explains the behavior of the magnetic fields around magnetic materials and it is based on phenomena. Basically, is a description of an averaged function of the atomic structure and we consider the magnetization of some magnetic material as a continuum function of the position. Following this paradigm we could end up ignoring relevant information about how nanoparticles are arranged in space and the interaction that may be happening between them. On other hand we have the quantum theory which explains the source of the magnetic moments in the magnetic materials and is based on an atomistic background. In this model the magnetization of the material is a discrete function of the position. This, of course, will take in consideration a wider set of elements and the interaction between the atoms. The downside is that this method would require an astronomical amount of computational time to simulate a macroscopic material. The continuum theory of micromagnetism was developed to be the bridge that connects the classical theory and the quantum theory. In general, neither the pure classical or pure quantum theories is appropriate to describe the interaction of the magnetic moments in the process of magnetization or to describe the hysteresis loops of structures made of ordered spins [64]. But by means of micromagnetism there is an opportunity to develop an intermediate regime in which we take into account some of the geometrical aspects of the arrangement of magnetic particles but, at the same time, we could infer some of the properties of some macroscopic magnetic material.

Particularly, we are interested in the study of magnetic nanoparticles. These are tiny particles that can be manipulated by using of magnetic fields. In general, these particles are made-up by a magnetic-matrix (iron, nickel. cobalt, etc.) and some other material [65].

Moreover this type of nanoparticles have attracted the interest of the scientific community as it has been found that magnetic nanoparticles can be applied in the catalysis to separate chemical composites [66], biomedicine [67,68], microfluidics [69], data storage [70,71], and many more. Hence there is a growing interest to study and understand the characteristics and effects of magnetic nanoparticles. How these particles interact between them, how can we manipulate the orientation or position of nanoparticles, and the different properties that can be obtained by solely the geometric arrangement of the particles in space.

We are focused on studying a system with a finite number N of magnetic particles inside a cell confined in a three dimensional space $\mathbb{R}^3$. The geometry of each particle is denoted by Ω_i where the subindex $i = 1,2,3,...,N$ marks the particle. The aggregate of the space occupied by all the particles is denoted by

$$\Omega = \cup_{i=1}^{N} \Omega_i$$

and the boundary of each domain Ω_i is indicated by $\partial\Omega_i$. Each particle is considered as single-domain, and therefore, the magnitude of the magnetization inside each particle $|M_i|$ is constant. Considering that each particle has a saturation magnetization (M_s), then we propose a function

$$m := M/M_s = \begin{cases} 1, \forall (x,y) \in \Omega_i \\ 0, \forall (x,y) \in \mathbb{R}^3 \setminus \sum_{i=1}^{N} \Omega_i \end{cases} \tag{3.1}$$

which will be used later to express energy in dimensionless units.

Next, from the Maxwell's equations

$$\begin{aligned} \nabla \times H &= 0, \\ \nabla \cdot (H - M) &= 0, \end{aligned} \tag{3.2}$$

we know that there already exists a function U identified as the magnetostatic scalar potential that satisfies

$$H = \nabla U. \tag{3.3}$$

Also, we consider two cases: one in which the particles only have shape anisotropy and another in which the particles have both: shape and magnetocrystalline anisotropy. Since we will be treating mainly with uni-axial magnetic particles, we use

$$\Phi(m) = 1 - (m \cdot e)^2 \tag{3.4}$$

where e represents a unitary vector pointing in the direction of the easy axis of the magnetic particle.

i

3.2 Magnetic nanoparticles

In the present section we describe the systems that can (and are going to be analized) be studied with the scheme developed in this thesis. In general terms we treat with bidimensional magnetic nanoparticles without magnetocrystalline anisotropy.

In the present work we are using the micromagnetical model whose basic assumption is that the spin direction varies only by a small amount from one point to another. Therefore, we are assuming that the magnetization is a continuous function of its position in space $\vec{m}(x,y,z)$. Also, we are considering that the magnetization has a constant magnitude and hence the magnetization can only rotate on its own axis.

As we are going to describe the magnetic properties of some material, we are going to do so in terms of the magnetization $\vec{m}(x,y,z)$. Now, the magnetic properties of the system depends directly on the state of the magnetization of each particle. This state is governed by the configuration and interaction of the magnetization of the particles and the equilibrium states are those in which the energy reaches, at leas, a local minimum. Therefore, the task in hand is to compute the energy of the system and find the configuration of the magnetization that results in the minimum energy. To do so, we clearly need an expression for the energy of the system, the so called micromagnetic energy that is written as

$$\mathbb{E}(M) = \underbrace{\int_\Omega A|\nabla m|^2 dx}_{Exchange} + \underbrace{\int_\Omega K_a \Phi(m) dx}_{Anisotropy} + \underbrace{\frac{\mu_0}{2}\int_{\mathbb{R}^3} |\mathbb{H}_{stray}|^2 dx}_{Magnetostatic} - \underbrace{\int_\Omega \mathbb{H}_{ext}\cdot M dx.}_{Zeeman} \tag{3.5}$$

3.2.1 The Exchange Energy

The first term, called the exchange energy, comes from the quantum nature of the system. It is related to the interaction between the spins of pairs of ferromagnetic electrons which depends of the relative orientation of the spins. This is to say that energy is lower when the spins are parallel and higher when the spins are anti parallel. Using the Pauli's exclusion principle and the model of Coulomb for electrostatic interaction over every pair of lattice points in a crystal one can get to the expression

$$E_{ex} = \frac{JS^2}{a}\sum_i a^3 \left[\left(\frac{\partial \vec{m}_i}{\partial x}\right)^2 + \left(\frac{\partial \vec{m}_i}{\partial y}\right)^2 + \left(\frac{\partial \vec{m}_i}{\partial z}\right)^2\right], \tag{3.6}$$

where J is the exchange integral between some pair of atoms, S is the spin quantum number, $\vec{m}_i$ is the magnetization of the $i-th$ atom and, a is the lattice constant of the crystal. Later, as we define $A = JS^2n/a$ and replace the sum for an integral interpreting the space as a continuum, the latter equations becomes

$$E_{ex} = A \int_{\Omega} |\nabla \vec{m}|^2 dV. \tag{3.7}$$

3.2.2 The Anisotropy Energy

The next term in the list is the anisotropy energy. This term comes from the fact that ferromagnetic crystals (magnets) are anisotropic. Then, depending on the orientation of the external magnetic field with respect to the crystal, the magnetization can reach the saturation state at lower of higher values of the external field. This anisotropy energy is the work done by the external field to modify the magnetization from the easy axis to the hard axis. In this case, the explicit form of this term must be obtained from experiments and written in some functional form denoted by $\Phi(\vec{m})$. In general, there are a few models for the most common configurations of the lattice (cubic, hexagonal, etc). As this work deals principally with uniaxial particles we can propose the anisotropy energy density of one atom as

$$e_{ani}(\vec{m}) = K_a \Phi(\vec{m}) = K_a(1 - (\vec{m} + \vec{e})), \tag{3.8}$$

and integrating this over the whole volume we get

$$E_{ani} = \int_{\Omega} = K_a(1 - (\vec{m} + \vec{e}))dV. \tag{3.9}$$

Where K_a is the anisotropy constant and is commonly a function of temperature.

3.2.3 The Magnetostatic energy

Later, we describe the third term in the micromagnetic energy, called the magnetostatic energy. This energy comes from the dipolar interaction in the crystal. The a crystal each

magnetic moment creates a dipole field, but this field is influenced by the field of each of the other dipoles in the crystal. Now, the average field over the crystal generated by the interaction of all the magnetic moments is what we call the *demagnetization field*. This is interesting as this field is a nonrotational one and therefore, we can write the field as the gradient of some scalar potential U. This is

$$H_{demag} = H_{stray} = -\nabla U. \tag{3.10}$$

Now, to compute the the magnetostatic energy we consider the energy of each magnetic moment interacting with the demagnetization field. The sum over all the atoms will be the total magnetostatic energy of the crystal. This can be written as

$$E_{magnetostatic} = -\frac{\mu_0}{2}\sum_i \vec{\mu}_i \cdot \vec{H}_{stray}, \tag{3.11}$$

which in turn we can extend to the continuum and rewrite the last equation as

$$E_{magnetostatic} = -\frac{\mu_0}{2}\int_{\mathbb{R}^3} M_s(\vec{m} \cdot \vec{H}_{stray})dV. \tag{3.12}$$

Next, we must consider the boundary value problem that comes from the Maxwell's equations. These equations state that $\nabla \cdot \vec{H}_{stray} = -\nabla \cdot \vec{M}$. Later we plug equation (3.10) in the boundary value problem and we can derive that

$$E_{magnetostatic} = -\frac{\mu_0}{2}\int_{\mathbb{R}^3} (\nabla U)^2 dV = -\frac{\mu_0}{2}\int_{\mathbb{R}^3} |\vec{H}_{stray}|^2 dV \tag{3.13}$$

3.2.4 The Zeeman Energy

This term comes from the fact that every magnetic dipole moment $\vec{\mu}$ that interacts with some magnetic induction $\vec{B}$ is given by $-\vec{\mu} \cdot \vec{B}$. Now, let us define $\vec{B} = \mu_0 \vec{H}_{ext}$ and we get that

$$E_{Zeeman} = -\mu_0 \sum \vec{\mu}_i \cdot \vec{H}_{ex}, \tag{3.14}$$

is the interaction energy between the magnet and the external field. Now, if we make $\vec{M} = N\vec{\mu}$ and take the analysis into the continuum we obtain

$$E_{Zeeman} = -\int_{\Omega} \mu_0 M_s (\vec{m} \cdot \vec{H}_{ext}) dV \tag{3.15}$$

3.3 Weak formulation of the problem

In order to compute the micromagnetic energy, we need to calculate the magnetostatic scalar potential U for a given magnetization m. If ν is the normal with respect the surface of the partile. Then, the magnetostatic scalar potential satisfies the problem

$$\begin{cases} \triangle U = \nabla \cdot m \text{ in } \Omega \\ \triangle U = 0 \text{ in } \mathbb{R}^3 \setminus \Omega \\ \frac{\partial u}{\partial \nu} = m \cdot \nu \text{ in } \partial\Omega. \end{cases} \tag{3.16}$$

The former problem can be solved by taking the weak form of it. From Definition (2.2.18) and integrating by parts

$$\int_{\Omega} \varphi \triangle u = \varphi \nabla U \Big|_{\partial\Omega} = \varphi \frac{\partial u}{\partial \nu}\Big|_{\partial\Omega} = \varphi (m \cdot \nu) \tag{3.17}$$

and

$$\int_{\Omega} f \nabla \varphi = \int_{\Omega} \nabla u \nabla \varphi \tag{3.18}$$

we get to the weak formulation of the problem

$$\int_{\mathbb{R}^3 \setminus \Omega} \nabla u \nabla \varphi dx - \sum_{i=1}^{N} \int_{\partial\Omega} \varphi (m_i \cdot \nu) dx = 0 \tag{3.19}$$

3.4 Numerical scheme

3.4.1 The micromagnetic energy

We know that in order to create magnetic materials and devices we need to understand the effects of the material's microstructure on the macroscopic magnetic properties of the said material and, at the same time, we also need to understand how the interactions between

particles can impact the behavior of the material or device [72]. To this extent the finite element method (FEM) results to be an effective technique to treat these problems simultaneously [73–75]. To this end we use an energy based approach in which we start with a certain number of magnetic particles with magnetizations randomly orientated and then we find the configuration of the magnetization that corresponds to an energy minimum. Then, the micromagnetic energy in SI units is defined as

$$\mathbb{E}(M) = \int_\Omega A|\nabla m|^2 dx + \int_\Omega K_a \Phi(m) dx + \frac{\mu_0}{2}\int_{\mathbb{R}^3} |\mathbb{H}_{stray}|^2 dx - \int_\Omega \mathbb{H}_{ext}\cdot M dx. \tag{3.20}$$

Where A is the exchange constant, K_α is the anisotropy constant, and $\mathbb{H}_{stray} = -\nabla U$. In order to obtain a dimensionless form of the micromagnetic energy, let us define a dimensional constant C_d as

$$C_d = \frac{M_s^2}{2\mu_0}$$

and then divide the latter expression for the energy in order to obtain the volume-dimensional energy

$$E(m) := \frac{\mathbb{E}(M)}{C_d} = d^2 \int_\Omega |\nabla m|^2 dx + Q\int_\Omega \Phi(m) dx + \int_{\mathbb{R}^3} |\nabla U|^2 dx - 2\int_\Omega H_{ext}\cdot m dx. \tag{3.21}$$

where $Q = K_a/C_d$ is the quality factor and measures the strength of the anisotropy relative to that of the stray field. $Q < 1$ include the soft materials, and $Q > 1$ represents the hard materials; $d = A/C_d$ is the exchange length; $U = \frac{M_s}{\mu_0}\mathbb{H}_{stray}$ is a volume dimensional scalar magnetic potential and $H_{ext} = \frac{M_s}{\mu_0}\mathbb{H}_{ext}$ is a volume dimensional version of the external applied field [76] . In this case, we are going to compute the energy of several particles. Therefore, considering that the magnetization is constant inside each particle, the energy in discrete form is written as follows:

$$E(m) = d^2 \sum_{i=1}^{N} |\nabla m_i|^2 dx + Q|\Omega_i| \sum_{i=1}^{N} \Phi(m_i) + \int_{\mathbb{R}^3} |\nabla U|^2 dx - |\Omega_i| \sum_{i=1}^{N} m_i \cdot H_{ext} \tag{3.22}$$

for the purposes in this study, we are going to study only systems with single domain magnetic particles. Therefore, the term corresponding to the exchange energy is null.

3.4.2 Energy minimization

Now we have a way to compute the magnetostatic scalar potential for a given magnetization ($\vec{m}$). For the above, we also have means to compute the micromagnetic energy of the system for a given magnetization $\vec{m}$ and external applied field (H_{ext}). The next objective is to find the set $\vec{m} = (m_x, m_y, m_z)$ that corresponds to a local minimum in the micromagnetic energy. This is carried out by using the Lagrange Multiplier's technique.

We consider a problem in which we want to minimize

$$E(m) = Q|\Omega_i| \sum_{i=1}^{N} \Phi(m_i) + \int_{\mathbb{R}^3} |\nabla U|^2 dx - |\Omega_i| \sum_{i=1}^{N} m_i \cdot H_{ext} = 0.$$

subjec to

$$\int_{\mathbb{R}^3 \setminus \Omega} \nabla u \nabla \varphi dx - \sum_{i=1}^{N} \int_{\partial\Omega} \varphi (m_i \cdot \nu) dx = 0$$

.

Therefore, we are looking for the direction of maximum descent of the energy with respect to the magnetization of each particle. To this end, we take the the lagrangian as

$$\begin{aligned} \mathcal{L}(m_i, U) = &\int_{\mathbb{R}^3 \setminus \Omega} \nabla u \nabla \varphi dx - \sum_{i=1}^{N} \int_{\partial\Omega} \varphi (m_i \cdot \nu) dx \\ &+ Q \sum_{i=1}^{N} |\Omega_i| \Phi(m_i) + \int_{\mathbb{R}^3} |\nabla U|^2 dx - \sum_{i=1}^{N} |\Omega_i| m_i \cdot H_{ext} \end{aligned} \tag{3.23}$$

then, we add a perturbation in the magnetization as follows

$$m_i \to m_i + \varepsilon \alpha_i \tag{3.24}$$

and then take the derivative with respect to ε and evaluate at $\varepsilon = 0$ and obtain

$$\begin{aligned} \frac{\partial \mathcal{L}}{\partial \varepsilon}(m_i + \varepsilon\alpha_i, U, \varphi) = &- \sum_{i=1}^{N} \int_{\partial\Omega} (\alpha_i \cdot \nu) \varphi dx \\ &+ 2Q \sum_{i=1}^{N} |\Omega_i| (m_i \cdot e) \cdot (\alpha_i \cdot e) - \sum_{i=1}^{N} |\Omega_i| \alpha_i \cdot H_{ext} \end{aligned} \tag{3.25}$$

from the last equation is clear that the gradient with respect with the magnetization is given by

$$\nabla_{m_i} E(m_i) = - \sum_{i=1}^{N} \int_{\partial\Omega_i} \alpha_i \nu \varphi dx + 2Q \sum_{i=1}^{N} |\Omega_i| (m_i \cdot e_i) e_i - \sum_{i=1}^{N} |\Omega_i| H_{ext} \tag{3.26}$$

equation (3.26) gives the direction in which the magnetization must move in order to reach a local energy minimum. Then energy minimization is carried out by means of a Newton algorithm [77].

If we take the partial derivative with respect to U in the same fashion we get

$$\frac{\partial \mathcal{L}}{\partial \varepsilon}(m_i, U + \varepsilon\alpha, \varphi) = \int_{\mathbb{R}^3} \nabla \alpha \cdot \nabla (u + \varphi) dx, \tag{3.27}$$

This equation holds for every function $\varphi \in H^1$. Therefore, in an extremal, this equation must be null and implies that

$$\varphi = -U.$$

Indicating that the test function is equivalent to the additive inverse of the magnetic scalar potential.

Finally, we take the partial derivative with respect to the test function φ

$$\frac{\partial \mathcal{L}}{\partial \varepsilon}(m_i, U, \varphi + \varepsilon\alpha) = \int_{\mathbb{R}^3} \nabla U \cdot \nabla \alpha dx - \sum_{i=1}^{N} \int_{\partial\Omega_i} (m_i \cdot \nu)\alpha dx. \tag{3.28}$$

This equation is nothing more than the constrain to the energy in weak form.

3.5 Non-dimensional units and material parameters

For the graphics in the results section we see that both axis are in non-dimensional units. In order to make a clearer description of the graphics, we explain which are the material parameters we are taking into account. We start by defining the energy in SI units as

$$\mathbb{E}(J) = \int_\Omega A|\nabla m|^2 + \int_\Omega K_a \phi(m) + \frac{1}{2}\int_{\mathbb{R}^3} \mathbb{H}_{stray} - \int_\Omega \mathbb{H}_{ext} \cdot J \tag{3.29}$$

where J is the magnetization density, then we define the nondinensional magnetization as $m := J/J_s$ such that

$$m = \begin{cases} 1 & \text{in } \Omega \\ 0 & \text{in } \mathbb{R}^3 \setminus \Omega \end{cases} \tag{3.30}$$

Next, we need to define de volume-dimensional energy. To this end, we set

$$H_{ext} = \frac{\mathbb{H}_{ext}}{J_s} \tag{3.31}$$

$$U = \frac{\mathbb{U}}{J_s} \tag{3.32}$$

$$H_{stray} = \frac{\mathbb{H}_{stray}}{J_s} = -\nabla U \tag{3.33}$$

and define the volume-dimensional energy as

$$E(m) := \frac{\mathbb{E}}{K_d} = d^2 \int |\nabla m|^2 + Q \int \phi(m) + \int |\nabla U|^2 - 2\int H_{ext} \cdot m \tag{3.34}$$

where,

$$K_d = \frac{J_s^2}{2} \tag{3.35}$$

$$Q = K_a/K_d = \text{ quality factor} \tag{3.36}$$

$$d = (A/K_d)^{1/2} = \text{ exchange length} \tag{3.37}$$

Finally, we use the fact that the length unit cell of our system of interest (magnetotactic bacterias) is around 50 nm. Then, our dimensions are going to be set such that $x \to x/\ell$,

where ℓ =50nm. Then, we divide the volume-dimensional energy by the volume of the cubic cell (Ω) (or square) as appropiate and we obtain the non-dimensional energy

$$e(m) := E(m)/|\Omega| = \kappa^2 \int_Q |\nabla m|^2 + Q \int_\omega \phi(m) + \int_{\mathbb{R}^3} |\nabla u|^2 - 2 \int_\omega h_{ext} \cdot m \tag{3.38}$$

where

$$\kappa = d/|\Omega|, \tag{3.39}$$

$$u(x/\ell) = \frac{1}{\ell} U(x), \tag{3.40}$$

$$h_{stray}(x/\ell) = -\nabla u(x/\ell) = H_{stray} = -\nabla U(x), \tag{3.41}$$

$$h_{ext}(x/\ell) = H_{ext}. \tag{3.42}$$

For practical purposes, we set $J_s = 0.5$T such that $\mathbb{H} \approx 0.039 h_{ext}$. With this in mind, when you see $h_{ext} = 1$ in the results, we mean an external applied field of 39mT.

Chapter 4

Computer implementation

4.1 Discretization of the weak form equations

In general, the discretization of the variational problem is made automatically by the software *FreeFEM++* [78]. The software is described by its author as follows:

> "FreeFEM is a partial differential equation solver for non-linear multi-physics systems in 1D, 2D, 3D and 3D border domains (surface and curve). Problems involving partial differential equations from several branches of physics, such as fluid-structure interactions, require interpolations of data on several meshes and their manipulation within one program. FreeFEM includes a fast interpolation algorithm and a language for the manipulation of data on multiple meshes. FreeFEM is written in C++ and its language is a C++ idiom."

As mentioned above, this software package is an idiom of C++ and therefore can run in almost every operative system (OS) making this a good option to create the numerical scheme we want to achieve. Also, *FreeFEM++* has an input mode for the variational formulation of the problem; a geometric input given by the analytic description of the figure; an automatic mesh generator with inner point density proportional to points in the boundary; and inline generator of image and text files.

The space is discretized by a squared mesh of 50 points in each side and the particles are represented by ellipses with 50 points distributed in the perimeter. This is created using the *border* and *mesh* functions already built in *FreeFEM++*. This is done using

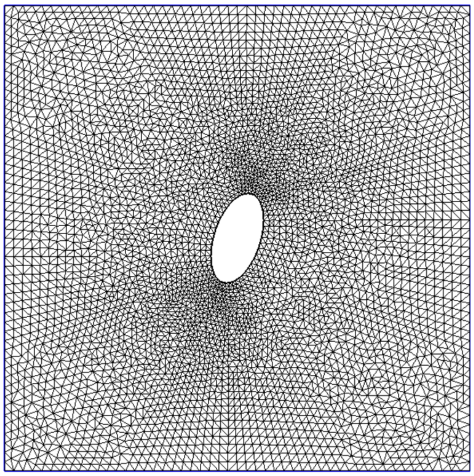

Figure 4.1: Results of the automatic discretization of the physical space done with *FreeFEM++*. We can appreciate that there is a higher density of points near the boundary of the ellipse which represents the magnetic particle.

```
border a1(t=0.0,boxwidth){x=t; y=0.0; label=901;};
border a2(t=0.0,boxheight){x=boxwidth; y=t; label=902;};
border a3(t=0.0,boxwidth){x=boxwidth-t; y=boxheight; label=903;};
border a4(t=0.0,boxheight){x=0.0; y=boxheight-t; label=904;};
real xcenter= boxwidth/2.0;
real ycenter= boxheight/2.0;
border C0(t=0, 2.0*pi){
  x= xcenter +xradius*cos(t)*cos(a0) -yradius*sin(t)*sin(a0) +xshift;
  y= ycenter +xradius*cos(t)*sin(a0) +yradius*sin(t)*cos(a0) +yshift;
  label=0;
};

int mp=meshpoints;
mesh Th= buildmesh( a1(mp)+a2(mp)+a3(mp)+a4(mp)+C0(-mp) );
```

The result can be seen in figure 4.1 where we can see how the points and finite elements are constructed and distributed. We observe that there is a lower density of points at the edges of the square (relatively far from the particle) and there is quite much chore points near the particle. This is done in this way to optimize the computational time and use the resources where we need it.

Later, we have discretized the space of functions $u(x,y)$, which represent the magnetostic potential. This is done merely by use of the function *fespace*.

```
fespace Vh(Th, P1);
```

```
Vh uh, vh, hx, hy, F;
```

where, uh, vh, hx, hy and F represent the problem variables $u = (u, V)$ and $h = (hx, hy)$ and F is an auxiliar variable to keep data of the variational problem.

And finally, we use the function *varf* to implement the variational formulation of the problem inside the virtual space. This is done as follows:

```
varf aa(uh,vh)= int2d(Th)( dx(uh)*dx(vh) +dy(uh)*dy(vh) )
+on(901,902,903,904, uh=0);
```

As we can see, the implementation of the mathematical model as a numerical discrete scheme is done almost entirely by the software. The reader can recognize the structure of some of the written equations in the code above. The syntax is almost identical.

4.2 Numerical algorithm

The algorithm goes as shown in algorithm 1. The principal idea is to find the configuration of the magnetization of each particle which corresponds to a local minimum in the energy and thus to a stable configuration for the given external field value. We start with one initial data: the initial magnetization $\vec{m}_0$. Then, for the first value of the external field, we solve the numerical problem to find the magnetostatic scalar potential ($\vec{u_0}$) for the initial magnetization ($\vec{m}$) and the current external applied field (H_{ext0}). Then compute the energy $E(\vec{u_0}, \vec{m}_0, H_{ext,0})$ and the gradient of that energy with respect the actual magnetization. Now that the direction of maximum descent is known, we compute the next iteration of the magnetization $\vec{m}_1$ by adding a vector to the magnetization in the direction of maximum descent and normalizing the new magnetization to its norm. Then, we repeat the process and calculate the magnetostatic potencial u_1, the energy $E(\vec{u}_1, \vec{m}_1, H_{ext,0})$ and the gradient of the energy with respect the new magnetization and the same external applied field.

Once its done, we compare the energy of the k state E_k with the energy of the $k+1$ state E_{k+1} and make sure that the energy is diminishing. In this part, we use a line search algorithm to find the local energy minimum by iterating the magnetization $\vec{m}_i$. Finally, we use energy as a convergence test. As we approach the local minimum the difference $E_{k+1} - E_k$ must be as small enough, indicating that the energy on the point k is as close to the energy in the point $k+1$ as desired. On the other hand, if the system is in a non-saturated state the gradient of

the energy with respect the magnetization must approach to zero. Then we can say that the algorithm has found the magnetization that gives an stable configuration (which corresponds to the local energy minimum). This magnetization is stored into a file along with the current external field applied to the system. Then, the algorithm proceeds to the next iteration in the external applied field and the process is repeated.

$\vec{m}_k \leftarrow \vec{m}_{initial}$
$H_{ext} = H_{ext,initial}$
while $H_{ext} < H_{ext,final}$ **do**
  while $||\nabla_m E|| > \varepsilon$ **or** $|E_{k+1} - E_k| > \varepsilon$ **do**
    Compute $u(\vec{m}_k)$ by solving Eq. (3.19)
    Compute $E(\vec{m}_k)$ by Eq. (3.22)
    Compute $\nabla_{m,k} E$ by Eq. (3.26)
    Compute $\vec{m}_{k+1} = \vec{m}_k + \vec{\alpha} \cdot \frac{\nabla_{m,k} E}{|\nabla_{m,k} E|}$
    Normalize $\vec{m}_{k+1}$
    Compute $u(\vec{m}_{k+1})$ by solving Eq. (3.19)
    Compute $E(\vec{m}_{k+1})$ by Eq. (3.22)
    Compute $\nabla_{m,k+1} E$ by Eq. (3.26)
    if $E(\vec{m}_{k+1}) < E(\vec{m}_k)$ **then**
      continue
    else
      $\vec{\alpha} \leftarrow \vec{\alpha}/2$
      $\vec{m}_{k+1} \leftarrow \vec{m}_k$
    end if
  end while
  $\vec{m}_c \leftarrow \vec{m}_k$
  OutputFile $\leftarrow [H_{ext}, \vec{m}_c]$
  $H_{ext} \leftarrow H_{ext} + \Delta H_{ext}$
end while

The complete code can be downloaded directly from the Github page of the author [79].

Chapter 5

Numerical Results

For reference and as a first test, we analyze the classical problem of a Stoner-Wohlfarth particle. This corresponds to a single dominain ellipsoidal particle with a uniaxial magnetic anisotropy whose easy axis is along the long axis of the ellipsoid. The objective is to calculate the hysteresis loops for different applied field directions with respect to the easy axis.

In this chapter we show the results of simulating various configurations of magnetic particles. This intends to explore the effects changing the microstructure of an array of magnetic particles over the hysteresis curve (a macro property). Also, this set of examples serve as an sample of the systems that can be simulated with the numerical scheme developed in this work.

5.1 Stoner-Wohlfarth particles

For the simulation, we are defining t as $d^2/|\Omega| = 1t$ as a measure of length inside the code. Then, fot this numerical experiment we are using a bounding square box of $[0,10t] \times [0,10t]$ with open (Dirichlet) boundary conditions. The length of the major and minor semiaxis are $1t$ and $0.5t$, respectively, The external applied field is sweeped from $[-5,5]$ in units of $z = \frac{M_s}{\mu_0}\mathbb{H}_{ext}$.

This experiment is used as fireproof for the code we begin by computing the hysteresis curve of single particle with elliptical shape. An external magnetic field H_{ext} is applied in the vertical axis of the system. Let us define ϕ as the angle between the easy axis of the particle

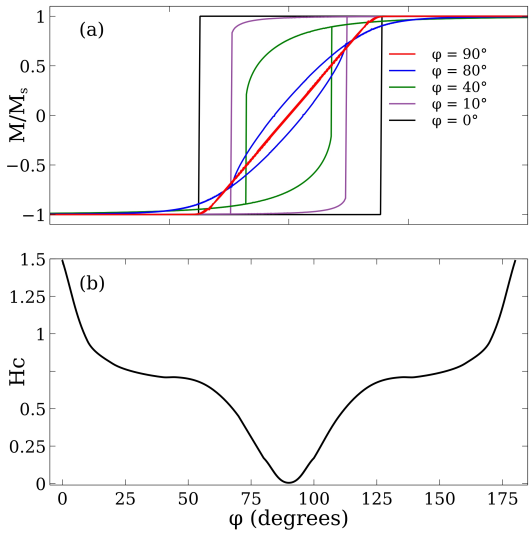

Figure 5.1: Hysteresis curves of the particle as we shift the angle from a vertical position ($\phi = 0^o$) to an horizontal position ($\phi = 90^o$).

and the direction of the external field H_{ext} so that $\phi = 0$ when the easy axis is parallel to the direction of the external field. As shown in figure 5.1a. This is, $\phi = 0$ when the easy axis of the particle is in the upward vertical direction. We vary ϕ by moving the easy axis of the particle and observe the interaction between the external field and the magnetization of the particle. The resulting hysteresis curves for different values of ϕ are shown in figure 5.1b which agree with the Stoner-Wolhfarth model [80].

5.2 Axis length

Next is the case in which we modify the geometry of a single isolated magnetic particle. Then, we extend the length of one of the semiaxis of the ellipse while the length of the other is held constant. In this experiment we are using a squared bounding box such that $[0, 10t] \times [0, 10t]$ with open boundary conditions, the minor semiaxis is held constant at $0.2t$ and we shift the major semiaxis from $0.2t$ to $1.1t$. Also, we are using an angle $\phi = -60^o$.

The results of this experiments are shown in figure 5.2. Each figure consists on the geometry of the particle (in color white) in the upper row and its respective hysteresis curve in the bottom row.

We start with a circle, as shown in figure 5.2(a), Then, we enlarge one of the semiaxis of the particle in a sequence. In figures b, c, and d the mayor semiaxis has a length of $0.4t$, $0.8t$, and $1.1t$, respectively. Also, for this three figures we have a coercivity of approximately $0.5z$,

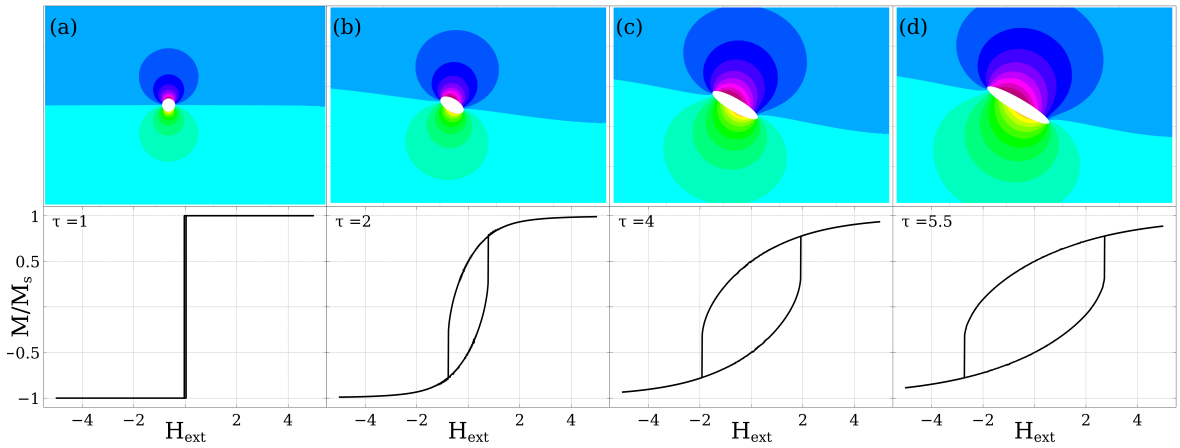

Figure 5.2: Upper row: the geometry of the particle is shown in white. The colors represent the magnetostatic schalar potential (u). The red and black dashed lines are the minor and major semiaxis, respectively. The length of each axis in units of $d^2/|\Omega|$ is indicated in the bottom row. Bottom row: hysteresis curve of the system obove each curve. In the left upper corner of each plot is the length of the major and minor semiaxis of the particle inside the system.

$2z$, and $3z$ in units of $z = \frac{M_s}{\mu_0}\mathbb{H}_{ext}$. Therefore, we can see that the coercivity of the systems increases as the shape of the particle becomes more asymmetrical. This is exactly what one would expect, as, with a less symmetrical geometry there is more shape anisotropy such that we requiere a more intense magnetic field to chance the magnetization of the particle. This is, we need more field to flip the magnetization of the particle. Also, as we enlarge one of the axis while keeping the other as a constat, the solume of the particle is increasing. Therefore, we need a stronger field to flip the magnetization of the particle. In any case, this experiment proves that the simulator is capable of detect and show the interaction between the geometry of the particles and the intensity and direction of the external magnetic field applied. Further, it also prooves that the code is sensible to the volume of the particle in the system.

5.3 Constant area

In the past experiment we observed that the program is capable of fetch the changes in the hysteresis curve coming from both the volume and the shape of the particle. As a way to discard that the increment in the coercivity is due only to the change in volume, in this experiment we change the dimensions of the particle, such that the product of major semiaxis and minor semiaxis remains constant. This is $ab = 0.495t^2$, such that the volume remains constant. Where $t = d^2/|\Omega|$. The bounding box in this experiment is a square of $[0, 10t] \times [0, 10t]$ with open boundary conditions.

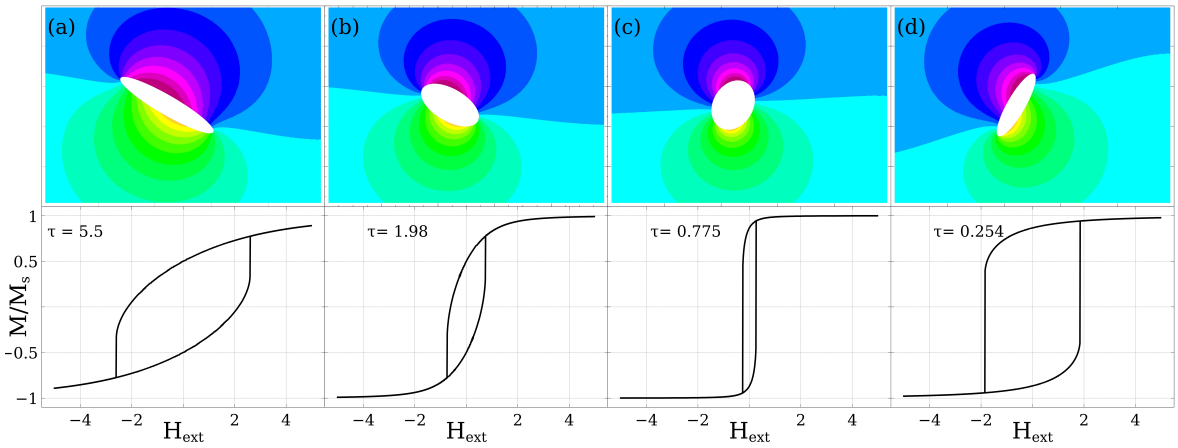

Figure 5.3: Upper row: the geometry of the particle in white. u is represented in the colorbar. Red and black dashed lines indicate the semiaxis of the elliptical particle. Bottom row: hysteresis curve of the system. The length of each of the semiaxis is shown in the upper left corner of each plot in units of t. In this case, the major and minor semiaxis are selected such that the product between them remain fixed to 0.495.

The results of this experiment are shown in figure 5.3. There we can see that when the particle has a more rounded form, the coercivity of the system is of the order of $1z$. This is the case of the figure 5.3b and (5.3c. On the other hand, for the figures 5.3a and 5.3d which have a stretched form, we see that the hysteresis curves goes around $2z$. In this experiment, the changes in the coercivity are due only to the shape of the particle beacuase the volume of the particle is held constant. Therefore, the code is capable of account the changes in the hysteresis curve due to the change in the geometry of the particles inside the system. Also, from the hysteresis curves, we get a relationship between the eccentricity of the ellipse and the coercivity of the system. For each of the systems shown in figure 5.3 their respective eccentricity is $0.181, 0.505, 0.775$ and 0.254. This can be compared to the predictions corresponding to the Stoner-Wohlfarth model. In this case, for eccentricity above 0.254 the coercivity does not increase anymore.

5.4 Volume fraction

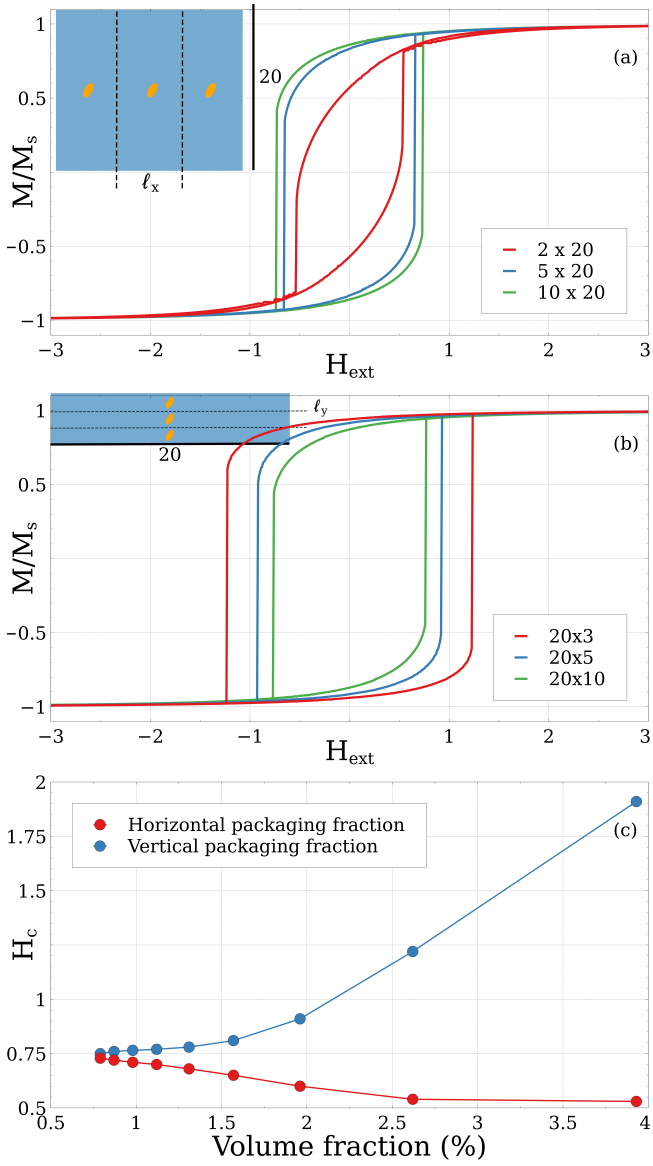

Figure 5.4: Top: Schematization of the system. We study a single cell with periodic boundary conditions, therefore, there is an exact copy of the cell next to every side of the principal cell. Every set of particles of similar size is the schematization of one experiment and each experiment is a red point in the graph below. Bottom: plot of volume fraction vs coercivity. As we increase the volume fraction, the coercivity of the system diminish. Indicating that the code can calculate the interaction between two particles in different cells.

Next, we present an experiment with periodic boundary conditions. To this end, we use a rectangular bounding box. The height of the box is $20t$ and the width of the box is sweeped from $2.5t$ to $12t$. The major semiaxis of the particle is equal to $1t$ and the minor semiaxis of

the particle is $0.5t$. The tilt of the particle is such that $\phi = 50^o$. The goal of the experiment is to make sure that the code is taking into account the interaction between particles in periodic interacting systems. So, let us define a cell for this experiment. We take a cell as a rectangle containing one particle. The dimensions of the cell (bounding box) are selected such that the particle interacts with the particles at its sides but the particles above and below are too far away to make an interaction with the particle in the selected cell. Then, we hold the size of the particle, but we reduce the width of the cell, making a more pronounced interaction between the particles in each cell. Thus, as we reduce the dimensions of the cell, we are increasing the volume fraction of magnetic material inside each cell. Then, we compute the hysteresis curve of each cell and manually obtain the coercivity and the volume fraction of each experiment. The results are shown in the bottom row of figure 5.4. Every point (volume fraction, coercivity) is a red dot in the resulting plot. From this, we can recall that as we increase the volume fraction (partciles get closer) the coercivity of the system goes down. This makes sense, as the particles at the sides help to flip the magnetization of the system. This is, we requiere less external magnetic field to change the magnetization of the particle [81]. Therefore, the code successfully takes into account the interaction between particles on different cells by just changing the boundary conditions of the system.

5.5 Interaction between two adjacent particles: distance between particles

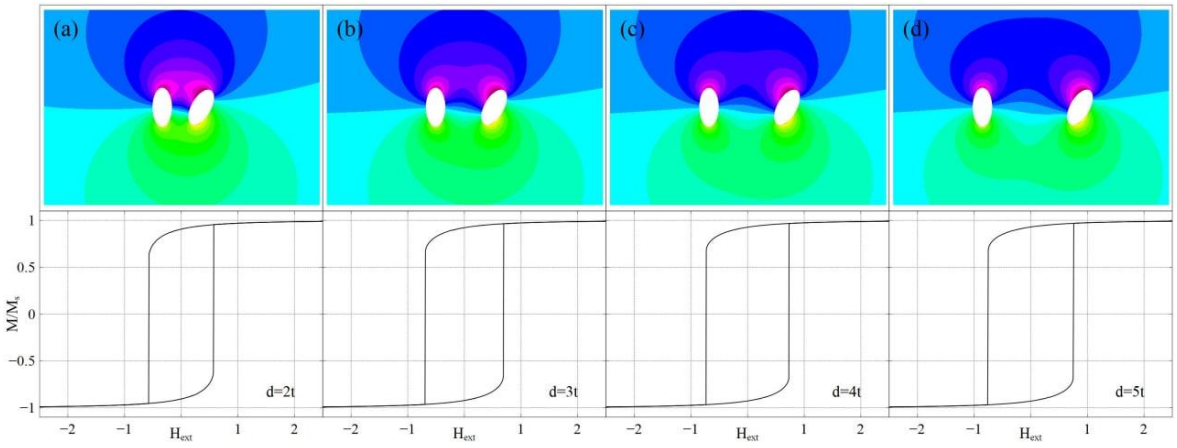

Figure 5.5: Two particles inside a unit cell with open boundary conditions. Top: schematic cell of the system of study. The particles are in white and the magnetostatic scalar potential u is in color. With each iteration we separate the particles on increments of $1t$. Bottom: hysteresis curve of the system above. We can see that the hysteresis curve of the respective system.

In the past section we checked that the code considers the interaction between particles in distinct cells. As a complement, we check that the code also considers the interaction

between two particles inside a single cell with open boundary conditions. For this, we use a bounding box of dimensions $[0,30t] \times [0,30t]$. Also, we use two identical particles with a major semiaxis of $1t$ and a minor semiaxis of $0.5t$. The first particle has its easy axis paralell with the external field ($\phi_1 = 0$) and the second particle has a tilt $\phi = 30^o$. In this experiment we begin with the particles separated by a distance of $2t$ then we enlarge this distance of separation up to $5t$ in order to study the interaction between these two particles.

The interaction between particles is shown in figure 5.5. As usual, we show the geometry of the system in the upper row and the hysteresis curve in the bottom row. We can see that in every system we get a similar shape of the hysteresis curve. However, as we augment the gap between the particles the hysteresis curve becomes wider. This implies that as we separate the particles, the coercivity of the system increases which means that the slanted particle is interacting less with the other particle, therefore needing more external field to flip the magnetization of both particles.

In any case, this demonstrates that the code can take into account the interaction between particles inside the same cell on open boundary conditions.

5.6 Interaction between two adjacent particles: the case of a rotating particle

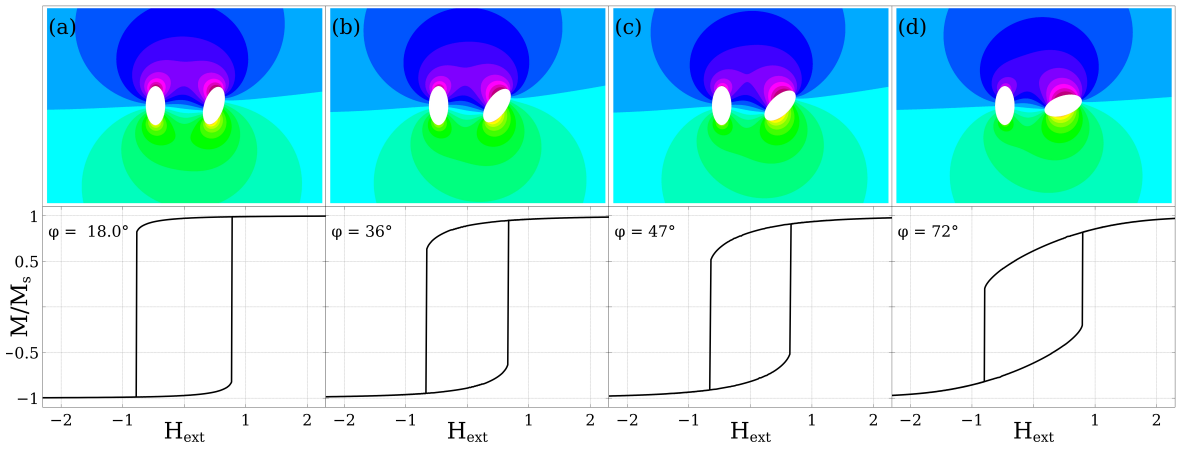

Figure 5.6: Top row: schematic primordial cell, in which the geometry of the system is shown. As usual, the colors represent u and the particles are in white. Bottom row: Hysteresis curve of the system above. The hysteresis becomes softer as the particles get more interactino between them because there is a wider set of accesible stable states for the magnetization.

For this experiment we use a bounding box of $[0,30t] \times [0,30t]$ with open boundary conditions. Inside the box there are two partciles with a major semiaxis of $1t$ and a minor

semiaxis of $0.5t$. Both particles are separated by a distance of $3t$, this is, the center of each ellipse is at $1.5t$ from the center of the box. The particle in the left has its easy axis parallel with the external applied field ($\phi = 0$), and the particle on the right is going to be slanted at $\phi = 18^o, 36^o, 47^o, 72^o$. The latter, to check that the code can show the interaction between geometry of the particles.

The result of this experiment is shown in figure 5.6. As usual, the upper row represents the geometry of the system and the bottom row the hysteresis curve of the system. In the upper row the values of the magnetostatic scalar potential are shown in color. In this case, we can see that the hysteresis curve starts in sort of squared shape, which makes sense if we think that the magnetization of both particles flip at the same time. This is, as soon as the slanted particle flips its magnetization, the vertical particle is affected by this interaction and tends to flip its magnetization as well. This is effect is the same in each of the cases studied. Nevertheless, we can see that when we modify the slope of the slanted particle, the shape of the hysteresis curve mutates into a rhombohedrical shape with a more smooth ascent. This is, the system locates a bigger set of stable magnetization states without reaching the saturation magnetization. Therefore, we can see states which are not the saturated state of the system. This results provide sufficient proof that the code can take into account the interactin between shape and position of particles inside the same cell.

5.7 Particles with arbitrary shape

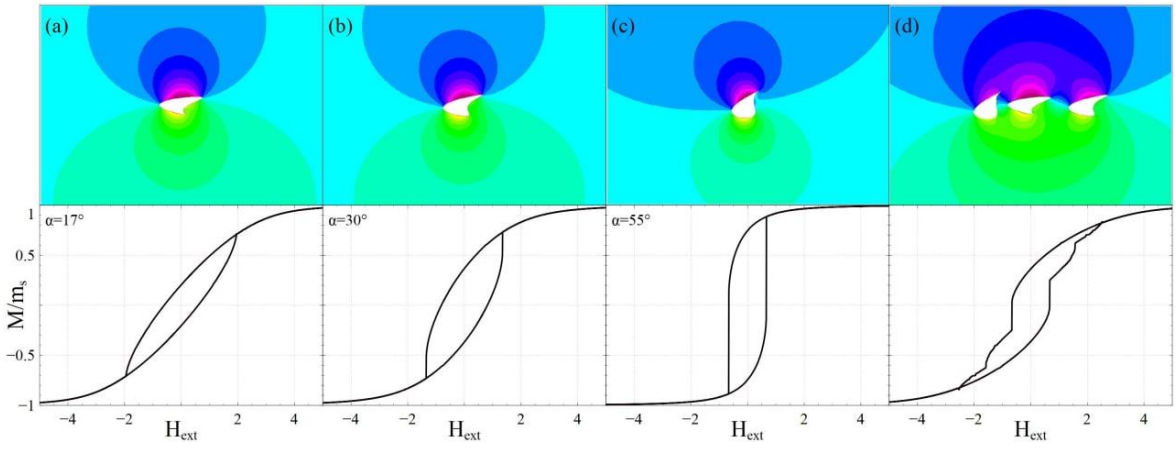

Figure 5.7: Top row: Particles with arbitrary shape and their corresponding magnetostatic potential. Bottom row: hystersis curve of the corresponding system.

Next, we want o test the capabilities of the code in terms of the geometries that can simulate. This is, particles with an irregular geometry. To this end, we use the parametric

equations

$$\begin{aligned} x =& x_0 + (a + \sin(t))\cos(t)\cos(\alpha) - b\sin(t)\sin(\alpha) \\ y =& y_0 + a\cos(t)\sin(\alpha) + b\sin(t)\cos(\alpha), \end{aligned} \tag{5.1}$$

where $a = 0.8, b = 0.4$ and $\alpha = 17^o, 30^o, 55^o$, to generate three particles with irregular geometry.

Then, as usual, we use a bounding box of $[0, 30t] \times [0, 30t]$ with open boundary conditions. Later, we compute the hysteresis curve for four systems. One system for each particle with a geometry given with by equation (5.1) for $\alpha = 17^o, 30^o, 55^o$. Then, we simulate a system in which a box with open bondary conditions holds the three particles before mentioned separated by a center-center distance of $2t$. The results of this experiment are shown in figure 5.7.As usual, the geometry and magnetostatic scalar potential (in color) are shown in the upper row and the hysteresis curve of each system is shown below of the sketch of each system in the bottom row.

The results show that the code can completely obtain the hysteresis curve of the systems with one particle inside the box. The particles in systems (a) and (b) are similar to an horizontal ellipsoid and therefore the hysteresis curve seems to have a more rounded shape acoording to the number of stable states of the magnetization. On the other hand, the particle in system (c) resembles more to a vertical ellipsoid resulting in a more squared shape of the hysteresis curve as the magnetization flips more abruptly. Finally for the system in (d) we see combination of the hysteresis curve of the systems in (a). (b) and (c). The rounded part of the hysteresis curve in (d) is a combination of the hysteresis curves of (a) and (b) while the vertical step in (d) corresponds with the vertical part of the hysteresis in (c).

Therefore, we can theorize that the magnetization of a system of particles in a combination of the individual hysteresis curve of each particle which makes up the system.

5.8 Magnetotactic bacteria

5.8.1 A Magnetotactic Bacteria

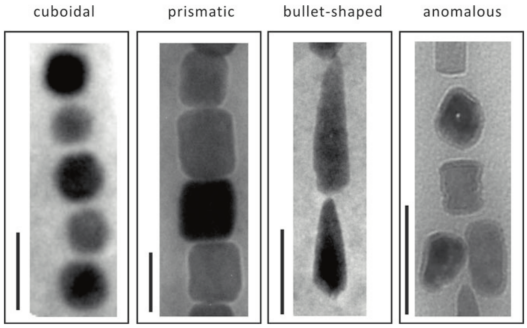

Figure 5.8: Transmission electron microscopy micrographs showing the shapes of the magnetosomes. Bars=100nm. [2]

The magnetotactic bacterias (MTB) are a group of bacteria that can align themselves with the Earth's magnetic field in order to reach regions with a low oxygen concentration [82]. MTB have a variety of morphologies such as coccoid, spirillar, rod-shaped, and multicellular cells with a certain number of chains of magnetosomes which at the same time are arranged in crystals and that can be cuboidal, prismatic, bullet-shaped, or anomalous (figure 5.8) [83,84]. The magnetosomes can be considered as magnetic particles with a single stable domain with sizes between 30 and 120 nm. Furthermore, the MTB's are made up of chains in order to optimize the magnetic moment which ensures that the MTB can move in the direction of the Earth's magnetic field [85]. MTB's can be found globally in diverse aquatic environments such as salt ponds, swamps, lakes, deep-sea sedimentals, among others [86]. This magnetosomes have a high potential in paleontology as proxys in paleoenviromental reconstructions and as magnetic separators or detectors [87].

The magnetosomes in MTB are made up of magnetite and the uncultivated MTB display tiny sizes and uniform morphologies. This causes that the MTB may be difficult to obtain by means of a chemical synthesis. But still, we can find the properties of the isolated magnetosomes as well as the properties of magnetosomes as part of a chain in a cell. In particular we can hope to find a coercivity field between 16.27 and 33.4 mT and a remanence between 20.34 and 46.7 mT [88–90]. Unfortunately, very few measurements are made in the uncultivated magnetosome chains due to the large number of cells required for measurements and this should be a potential research field for a numerical scheme.

In this study we numerically analyze various systems of MTB in order to understand the magnetic behavior of different lattices of magnetosomes. We intend to analize the cases

where we have an infinite array of cells with a chain of magnetosomes in each cell and the magnetosomes in the chains have different morphology. On the other hand, we analize a cell with a chain of magnetosomes with uniform and mixed morphologies to find the optimal geometric configuration that leads to nano-technological applications of the MTB. This is accomplished by using the full micromagnetic energy and a FEM numerical scheme. The numerical scheme is implemented with FreeFem++ [78]. Besides, the energy minimization method is based on a Lagrange multiplier method applied to the weak formulation of the micromagnetic energy. Also FreeFem++ enable us to easily change the boundary conditions in the problem to study the cases of a periodic array of cells and the case of an isolated cell.

5.8.2 Cuboidal shape

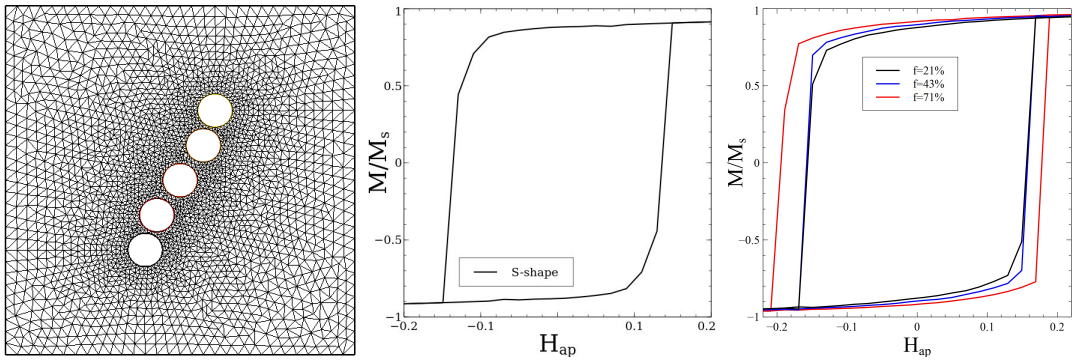

Figure 5.9: Left: geometry used to simulate the cuboidal shape of magnetosomes. Center: hysteresis curve of the ”S” shaped bateria. Right: hysteresis curve as function of the volume fraction.

In this simulation the particles are merely a circle or radius $r = 1.5$ units inside a squared box that serves as the unit cell containing the set of magnetosomes that make up the MTB.

We first studied the effects of moving the second magnetosome (counting from bottom to top) to the sides (over the x axis). If we displace the magnetosome to the left (red and black solid lines) we have that the hysteresis shows a step and the magnitude of the step is proportional to the displacement of the magnetosome. On the other hand, if we move the magnetosome to the right (green and blue dotted lines) the hysteresis shows a double step. In this case, the depth of the second step is inversely proportional to the magnitude of the displacement. This results are shown in the left plot of figure 5.9. From this affirmation we supposed that an ”S” shape, characteristic in certain MTB’s, would present an optimum hysteresis curve for field detection. The center plot of the figure 5.9 points otherwise. In this plot, the hysteresis loop show no steps, but it shows an increment in the remanence.

Exploiting the properties of the FEM and the weak formulation, is straightforward to change the area of the unit cell in which the magnetosomes are contained. For this end,

the size of the magnetosomes remains constant and we use the geometry shown in the left plot of the figure 5.9. In other words, we shrink the size of the unit cell as the size of the magnetosomes remain constant. Which is the same as increasing the packaging factor. The results are shown in the right plot of the figure 5.9. From the figure we conclude that the packaging factor is not an overwhelming characteristic to obtain superior field detectors. The effect of increasing the packaging factor sums up to increase the coercivity of the system.

5.8.3 Prismatic shape

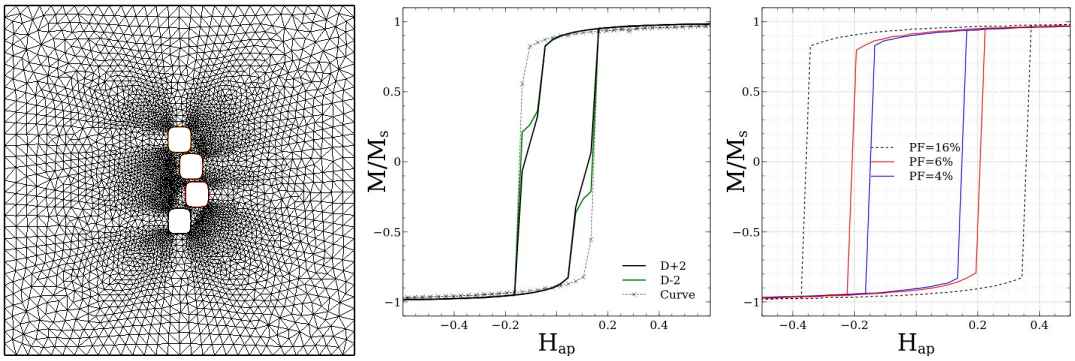

Figure 5.10: Left: Mesh used to simulate the prismatic shape of MTB's. Center: hysteresis curves of a system of magnetosomes in which one of the particles is displaced to left and right. Right: Hysteresis curve of the system as we increase the the packaging factor.

In this simulation the magnetosomes are constructed by the equation of the so called squircle:

$$x = \quad x_0 + \sqrt{|\cos(t)|} \cdot r_1 sign(\cos(t)) \tag{5.2}$$

$$y = \quad y_0 + \sqrt{|\sin(t)|} \cdot r_2 sign(\sin(t)) \tag{5.3}$$

where $t \in (0, 2\pi)$, $r_1 = 1.0$ units, and $r_2 = 1.1$ units. Once again, the starting size of the unit cell is $30x30$ units.

We analize the behaviour of a system of magnetosomes with prismatic shape. In first instance, we start with a system in which the magnetosomes are aligned in a vertical line. Then, let us take as reference the system shown in figure 5.10 we move one of the magnetosomes in the x direction. The hypothesis were that if we move a magnetosome the same distance to left and right, then we could obtain the same hysteresis curve. This has been proved wrong. From the center plot in the figure 5.10 we see that there is a remarkable difference in moving the particle two units to right and left. As we move the particle to the left, we can see two steps appearing.

We also tried the geometrical configuration shown in the right plot of the figure 5.11, in which two particles are moved to the right side. Te result is shown in in the center plot of the same figure with a black dashed line. We show that there is an increment in the coercivity of the system but no significant differences in the shape of the hysteresis.

Finally, we analyze the effect of the packaging factor. The process of shrinking the area of the unit cell as the size of magnetosomes is held constant is schematically shown in figure 5.11. The results are shown in the right plot of the figure 5.10. Once again, the volume fraction of is not a decisive factor in the form of the hysteresis curve. Also, the increment of the volume fraction is related with an increment in the coercivity of the system.

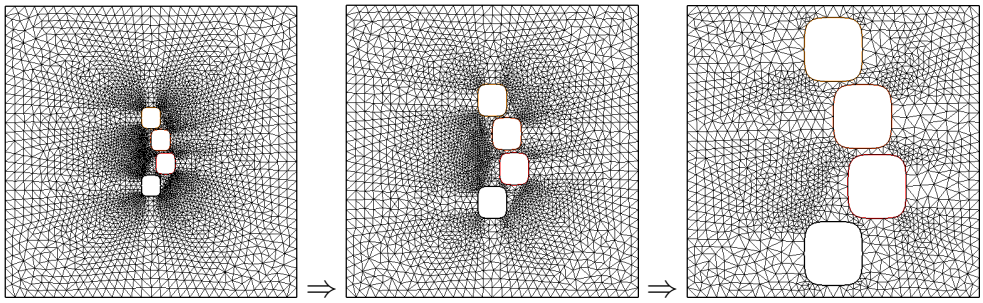

Figure 5.11: Evolution of a unit cell as we increment the volume of the magnetosomes with respect to the size of the cell.

5.8.4 Bullet shaped

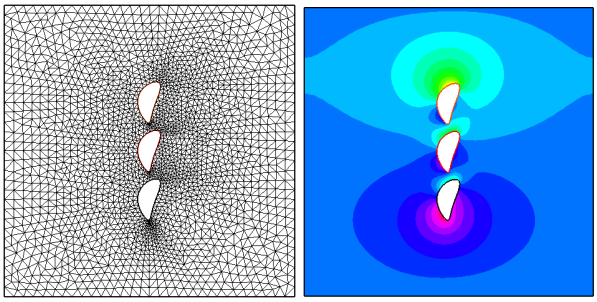

Figure 5.12: Mesh of the bullet shape of the magnetosomes and the magnetostatic potential of the array.

In this section we analyze the effects of moving magnetosomes and changing the volume fraction in the unit cell. We use the geometry shown in figure 5.12 in which the magnetostatic potential is also shown. In this sketch, we see that the particle at the bottom is the particle *1* and counting upwards we have the particles *2* and *3*, respectively. The unit cell has dimensions of $30x30$ units as above, and the shape of every magnetosome is obtained with

the equation:

$$x = x_0 + (r_1 + \sin(t))\cos(t)\cos(\theta_1) - r_2 \sin(t)\sin(\theta_2) \tag{5.4}$$
$$y = y_0 + r_1 \cos(t)\sin(\theta_1) + r_2 \sin(t)\cos(\theta_2) \tag{5.5}$$

where $t \in (0, 2\pi)$, $r_1 = 1.4$, $r_2 = 1.9$, $\theta_1 = 44°$, and $\theta_2 = 3°$.

From figure 5.13a is clear that displacing the magnetosomes to left or right has no significant effect over the behaviour of the hysteresis curve. But is remarkable that the displacement in each particle has a particular effect. In the figure 5.13b we see that a positive displacement of the magnetosomes first and third, yield a decrease in the coercivity. On the other hand, a displacement in the second particle yields an increment in the coercivity.

One should expect that a negative displacement should yield an opposite effect, but it is not the case. From figure 5.13c we can see that a negative displacement in the first and second magnetosomes yields a diminish in the coercivity. Yet, a negative displacement in the third magnetosome, brings an augment in the coercivity. Finally, in the figure 5.13d we see a comparison between a negative (solid lines) and a positive (dashed lines) displacements in the magnetosomes. Concluding that we can modify the coercivity of the system just by rearranging the position of the magnetosomes.

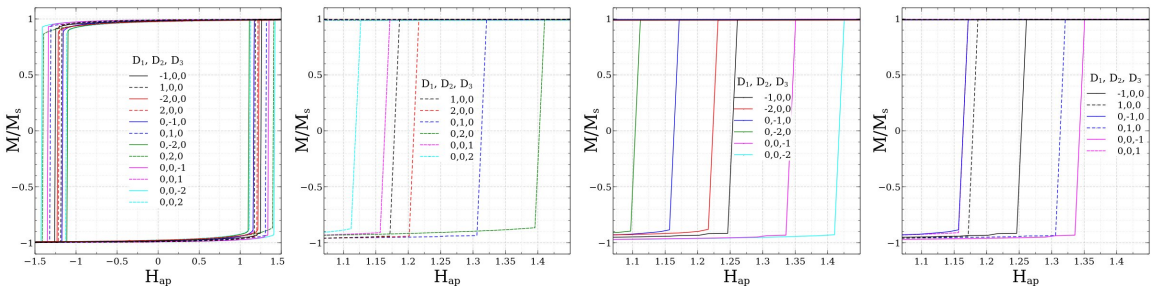

Figure 5.13: a) Hysteresis curve of the bullet-shaped magnetosomes in function of the displacements of the first, second, and third particle. b) Zoom at the hysteresis for positive displacements. c) Zoom at the hysteresis for negative displacements. d) Comparison between the positive and negative displacements.

In the case of the volume fraction, we see from figure 5.14 that the volume fraction plays a role in the coercivity of the system. Also, we check that we can obtain almost the same behaviour for a volume fraction of 2.77% and 4.69% (black and green lines, respectively).

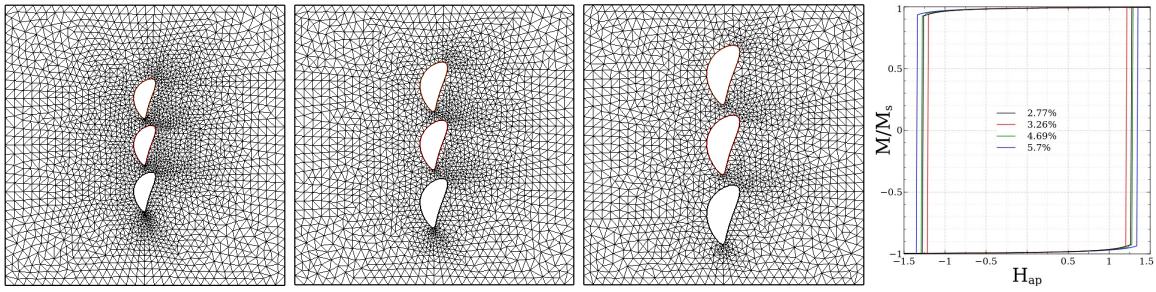

Figure 5.14: Evolution of a unit cell as we change the volume fraction and the hysteresis curve depending on the volume fraction.

5.8.5 Anomalous shape

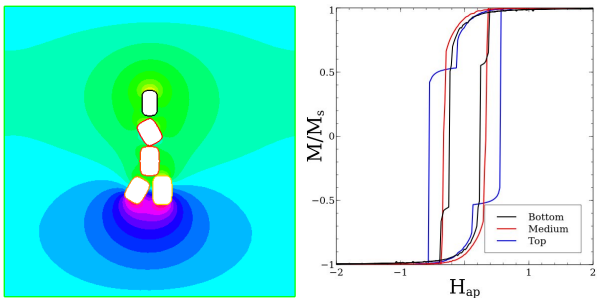

Figure 5.15: Right: Sketch of the system used to study the interaction of bacterias with anomalous shape. Left: Hysteresis curve with the doble particle in distinct positions.

Maybe the most interesting case in this article, is the one from anomalous shape. The mesh used to simulate the system is shown in the figure 5.15. As usual, the unit cell has dimenions of $30x30$ units. The shape of the magnetosomes is generated by applying a rotation matrix

$$\begin{pmatrix} \cos(\theta) & -\sin(\theta) \\ \sin(\theta) & \cos(\theta), \end{pmatrix} \tag{5.6}$$

where $\theta = 30°$, to a vector given by equations (5.2).

For the first experiment, we want to inquire the effect of the double magnetosome in a row. The hysteresis curve of the system is shown in the right plot of the figure 5.15. From there, we can see that if we put the double magnetosome at the bottom the hystereis curve shows the characteristic steps of magnetic field detector. When we put the double magnetosome in the middle of the chain we reduce this steps. Finally, when we put the double magnetosome at the top of the chain we obtain the most effective field detector.

Chapter 6

Analytical Results

6.1 Analytical magnetostatic mean-field model two dimensional array of cylinder shaped assemblies of packed spherical particles

The contents of this section correspond to the article:

Magnetostatic model for magnetic particle aggregates with cylindrical shapes
Victor Hugo Carrera-Escobedo, Kevin Hintze-Maldonado, Armando Encinas
DOI: https://doi.org/10.31349/RevMexFis.69.041605

6.1.1 Introduction

Using magnetic particles as building blocks to construct more complex structures is a well known approach to fabricate materials with tailored magnetic properties. A well developed and extensively studied class of such materials are the so-called soft magnetic composites [91]. In which magnetic powders of a soft magnetic material are compacted to form a larger, macroscopic shape. This materials are very interesting for their application as soft materials [92, 93]. Such constructions using densely packed particles has also been explored with magnetic nanoparticles [94–96]. Another interesting example was reported by Merk, et al, where they found that using wood as a template, an anisotropic composite material is

obtained, related to the hierarchical structure of wood [97]. In another report, magnetic particles have been printed using an inkjet printer leading to a anisotropic printed material [98]. These reports show that when particles are packed in a given geometry, the assembly tends to show a magnetic anisotropy having the symmetry of the enveloping volume [99, 100]. Interestingly, this has been observed when nearly spherical isotropic particles are packed together. This anisotropy is due to magnetostatic effects, in particular demagnetizing dipolar interaction between the particles. Moreover, there is evidence showing that changing the shape of the particle packing and forming arrays of such packings can lead to novel anisotropy properties which show symmetry properties derived from both the shape of the packing and the array formed with them [94, 95, 97, 98, 101].

Calculation of the magnetic anisotropy properties of these systems is complex and requires specialized software and computing resources [102]. In this sense, simple model calculations capable of providing a clear and practical view of the relation between the packing geometries and the resulting magnetic properties are needed. Specially given the current advancements of current fabrication techniques that provide an unprecedented control at the nanoscale to produce extremely complex particle assemblies. In this sense, herein we propose and validate a simple mean-field model for spherical particle assemblies which accounts for the magnetostatic properties of these systems. These properties allow to obtain the magnetic shape anisotropy of the assembly. Moreover, we focus our analysis to cylinder shaped assemblies of packed spherical particles. The cylindrical shape includes the tube (hollow cylinder) and the homogeneous cylinder. For both cases, it is possible to use approximate expressions for the demagnetizing factors leading to simple analytical expressions. The model is extended to include the more complex case of a two dimensional array of cylinder shaped assemblies of packed spherical particles. The results show that despite using spherical isotropic particles, the assembly shows an effective magnetic anisotropy that originates in the dipolar interaction between the magnetized particles. The symmetry and magnitude of this anisotropy depends explicitly on the geometrical parameters of the system.

Overall, the model is shown to lead to the expected limiting cases without any inconsistency. Moreover, we show that it allows to vary independently all the relevant parameters of the system. The results provide insight into the role played by each parameter and sheds ligth to possible mechanisms viable to control and tailor the magnetic anisotropy of these particle assemblies.

6.1.2 Analytical mean-field model for magnetostatic effects in assemblies of packed spherical particles

An analytical mean-field model has been developed to describe the effective or total magnetostatic shape anisotropy and dipolar interaction effects in assemblies of packed spherical

particles. We first present the model, starting with a brief overview of the basic expressions for a single assembly of packed spherical particles and then the model is extended for the case of a two dimensional array of cylinder shaped packings of spherical particles.

6.1.3 Single assembly of packed spherical particles

Previous work done in our group lead to the analytical mean field model for magnetostatic effects in a single assembly of packed spherical particles [3]. This model has served as the starting point to develop the extension for the two dimensional array of cylinder shaped assemblies of packed spherical particles. For this reason we now provide a brief review of this model in order to highlight the main expressions that were used for the extended model.

The basic system is a cylinder filled with spherical particles (the cylindrical packing of spheres). Herein we consider the general cylinder is a tube and the homogeneous cylinder is a particular case.

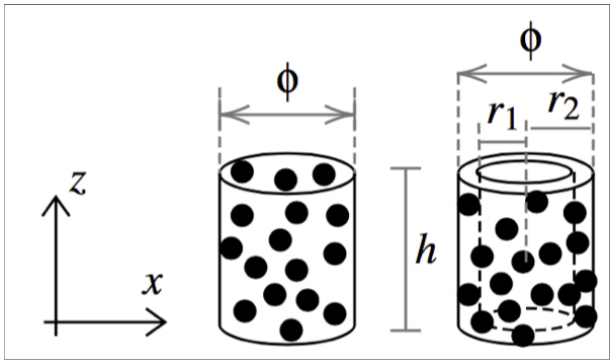

Figure 6.1: Two cylindrical packing of particles, a homogeneous cylinder and a tube, along with their main geometrical parameters. Image adapted from [3].

Figure 6.1 depicts this cylindrical packing of spheres and the coordinate system that will be used hereafter, the z-axis is taken parallel to the long axis and there is circular symmetry in the xy-plane. From this schema, we define the system parameters as the cylinder diameter ϕ, its height h, the aspect ratio $\tau = h/\phi$. Moreover, the particles occupy a packing fraction P of the total volume of the cylinder. For the tubular structure we use the internal and external radii r_1 and r_2 ($r_2 = \phi/2$), respectively.

We use the model proposed by Martinez-Huerta, et al; for the effective demagnetizing field for particle assemblies [103]. As it is customary for the calculation of demagnetizing effects, it is assumed that the system is fully saturated.

The model considers the assembly as a collection of identical particles contained in a bounding outer volume. The particles are the elemental building blocks and each is characterized by its volume V_1 and demagnetizing factor N_1. The external volume V_2 has a demagnetizing factor N_2. The particles occupy a volume packing fraction P in the external volume. The effective demagnetizing field (H_{Dt}), or the effective (total) demagnetizing factor ($N_{Dt} = H_{Dt}/\mu_0 M_s$) is written as [103],

$$N_{Dt} = N_1 + (N_2 - N_1)P. \tag{6.1}$$

This expression is the sum of the demagnetizing effects of the single elementary particle, the first term N_1, and the interaction between particles contained in the external volume and occupying a volume fraction P, which is the second term $(N_2 - N_1)P$.

The total magnetostatic or shape anisotropy can be determined using this expression. Recalling that the shape anisotropy is defined as $E_{St} = \mu_0 M_s^2 \Delta N_{Dt}$, where $\Delta N_{Dt} = \Delta N_{Dtx} - \Delta N_{Dtz}$. Here it is assumed that the easy axis is along the long axis of the cylinder, in this case the z axis while the hard axis is along x, see figure 6.1.

Using equation (6.1) to calculate ΔN_{Dt}, we obtain

$$\Delta N_{Dt} = \Delta N_1 + (\Delta N_2 - \Delta N_1)P. \tag{6.2}$$

This expression is proportional to the anisotropy energy E_{St}, so that in the following we use and refer to the effective anisotropy as $\Delta N_{Dt} = E_{St}/(\mu_0 M_s^2)$.

This expression is general as no specific geometries have been given. Considering spherical particles, the corresponding demagnetizing factor is $N_i = 1/3,\ i = x, y, z$. For the external volume we have a circular tube with $\beta = r_1/r_2$ as the ratio between inner and outer radii and where the homogeneous (or solid) cylinder corresponds to the particular case of the tube when $r_1 = 0$ and $\beta = 0$. The demagnetizing factor for the tube is $N_2 = \{N_{2x}, N_{2x}, N_{2z}\}$, where by symmetry $N_{2x} = N_{2y}$.

Noting that the particles are spherical, we have $\Delta N_1 = 0$. Additionally, taking advantage of the symmetry in the xy-plane, we can see that $2N_x + N_z = 1$ and $\Delta N_2 = (1 - 3N_{2z})/2$, we can write equation (6.2) for the effective anisotropy as,

$$\Delta N_{Dt} = [1 - 3N_z]\frac{P}{2}. \tag{6.3}$$

Hereon, we drop the number 2 in the sub-index, so $N_{2z} = N_z$. For N_z we use the approximate expression for tubes proposed by Nam, et al [104]; that relates the demagnetizing factor the tube with the one of the solid, homogeneous cylinder N_{cz},

$$N_z = N_{cz}(1-\beta^2). \tag{6.4}$$

While the axial demagnetizing factor of a homogeneous circular cylinder is computed as a function of the aspect ratio $\tau = h/\phi$ using the approximate expression proposed by Sato and Ishii [105], namely,

$$N_{cz} = \frac{1}{1+\frac{4\tau}{\sqrt{\pi}}}. \tag{6.5}$$

Using equations (6.4) and (6.5) in equation (6.3) leads to the approximate analytical expression for the shape anisotropy of a tube containing spherical particles,

$$\Delta N_{Dt} = \left[1 - \frac{3(1-\beta^2)}{1+\frac{4\tau}{\sqrt{\pi}}}\right]\frac{P}{2}, \tag{6.6}$$

which depends on the aspect ratio of the tube, $\tau \geq 0$, the thickness of the tube wall (β) and the volume fraction occupied by the particles and subject to $0 \leq \beta < 1$ y $0 \leq P \leq 1$.

Two dimensional array of assemblies of packed spherical particles

We now extend the model for the case of a two dimensional array of cylinder shaped assemblies of packed spherical particles. This case leads to the interaction between tubes. Figure 6.2 shows a 2D array of parallel tubes each containing spherical particles. In this case, we have the same parameters (inner and outer radii, height) with the addition of the center-to-center distance D and the reduced center to center distance D/ϕ. For this system we have two packing fractions: P_1 corresponding to the volume fraction of the spherical particles in each tube, and a second packing fraction P_2 corresponding to the tubes in the 2D array.

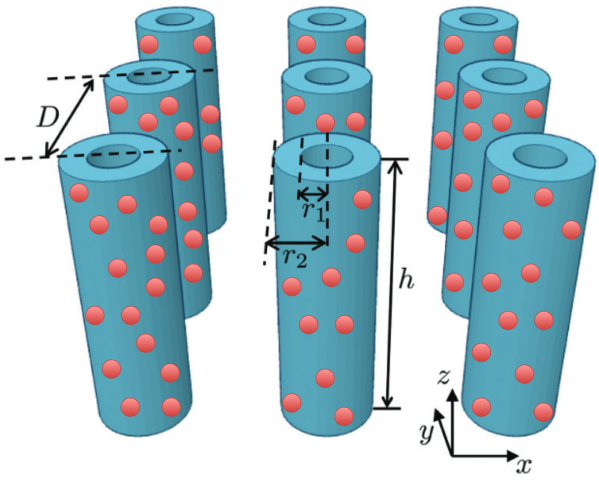

Figure 6.2: 2D array of parallel tubes each containing spherical particles with a vulome fraction P_1. The geometrical parameters of the system are the internal and external radii (r_1, r_2), their heigth h and the center-to-center distance D between the tubes.

This system can be described using three different volumes and their respective demagnetizing factors. As previously, the first volume is that of the spherical particles, N_1. The next volume is that of the cylindrical tube, N_2 and now we include a third volume which corresponds to a thin film, N_3, that contains the 2D array. Figure 6.2 depicts the system, where the same geometrical parameters are used as before with the addition of the center-to-center distance between cylinders D.

To extend the model we start with (6.1). Since the tubes (N_2) form an array, we call N_2' the effective demagnetizing factor of the tube array, so equation (6.1) reads as,

$$N_{Dt} = N_1 + (N_2' - N_1)P_1, \tag{6.7}$$

Now, for N_2' we use the same equation but introducing the third volume (thin film) and the packing fraction occupied by the tube array in the film (P_2): $N_2' = N_2 + (N_3 - N_2)P_2$. Substitution in equation (6.7) and rearranging terms, we obtain the expression for this system,

$$N_{Dt} = N_1 + (N_2 - N_1)P_1 + (N_3 - N_2)P_1P_2, \tag{6.8}$$

as in the previous section, the effective anisotropy is given as ΔN_{Dt}, this is,

$$\Delta N_{Dt} = \Delta N_1 + (\Delta N_2 - \Delta N_1)P_1 + (\Delta N_3 - \Delta N_2)P_1P_2, \tag{6.9}$$

As done before, from this expression it is possible to analyze the most important limiting cases. The first one is when $P_1 \to 0$, that corresponds to a single particle and we see that indeed, the previous expression reduces to $\Delta N_{Dt} = \Delta N_1$. If now we take the limit $P_1 \to 1$, which corresponds to a homogeneous tube, we can see that the terms containing ΔN_1

are eliminated and we obtain the expression corresponding to a 2D array of tubes having a packing fraction P_2 analogue to equation (6.1). Taking now $P_2 \to 0$ in equation (6.9), we recover the case of a single tube containing spherical particles. For the limit $P_2 \to 1$, we have that the tubes ideally fill entirely the volume of the thin film. From equations (6.8) and (6.9) we see that the terms containing N_2 are eliminated and we obtain the expression for a film (N_3) containing spherical particles (N_1) that occupy a volume fraction P_1. These are the four expected limits.

The corresponding demagnetizing factors can be entered in equation (6.9). For the spheres and tubes, we use the same as before and for the thin film $N_3 = \{0,0,1\}$.

Taking again $\Delta N = N_x - N_z$, we have that $\Delta N_1 = 0$, $\Delta N_2 = (1-3N_z)/2$ y $\Delta N_3 = -1$. This leads to,

$$\Delta N_{Dt} = \left[\frac{1}{2} - \frac{3}{2}N_z\right] P_1 - \left[\frac{3}{2}(1-N_z)P_2\right] P_1. \tag{6.10}$$

To further simplify, we use equations (6.4) and (6.5) for N_z as before. For the packing fraction of the tubes in the thin film (P_2) we use the expression reported previously for a 2D hexagonal array of tubes with external diameter ϕ separated by a center-to-center distance D and reduced distance as $d = D/\phi$ [106],

$$P_2 = \frac{\pi}{2\sqrt{3}} \frac{(1-\beta^2)}{d^2} \tag{6.11}$$

Note that the first term in equation (6.10) reduces to equation (6.6). Substitution of the expressions for N_z and P_2 leads to the following analytical expression for the (reduced) effective anisotropy,

$$\Delta N_{Dt} = \left[1 - \frac{3(1-\beta^2)}{1+\frac{4\tau}{\sqrt{\pi}}}\right] \frac{P_1}{2} - \left[\frac{\pi\sqrt{3}}{2}\left(1 - \frac{(1-\beta^2)}{1+\frac{4\tau}{\sqrt{\pi}}}\right)\frac{(1-\beta^2)}{d^2}\right] \frac{P_1}{2}. \tag{6.12}$$

This expression contains the sum of two terms and they both correspond to dipolar interaction field contributions. Comparing to equation (6.9), the first term in equation (6.12) is the dipolar interaction between the particles in a given tube. While the second term represents the dipolar interaction between tubes in the 2D array. Here again $\Delta N_1 = 0$ as the spherical particles have zero shape anisotropy. Then the anisotropy in this systems originates in the dipolar interaction between the constituent particles and their spatial arrangement.

We note that $P_1/2$ appear multiplying both terms, which as discussed in the previous section, it will simply modulate the amplitude of the effective anisotropy. Besides from P_1, the anisotropy depends on the width of the tube wall (β), the tube aspect ratio (τ) and the reduced center-to-center distance (d). The particular case of a 2D array of continuous/homogeneous

tubes is obtained when $P_1 = 1$, so equation (6.12) reduces to the expression reported previously [107].

6.1.4 Results and discussion

In the previous sections analytical approximate expressions have been obtained for the 2D array of tube shaped spherical particle arrays. These expressions can be easily evaluated making it practical and easy to obtain curves of the different quantities of interest. We analyze first the case of a single cylinder shaped assembly of packed spherical particles, and then we consider the 2D array of such cylinder shaped assemblies.

Single cylinder shaped assembly of packed spherical particles

The case of a single cylinder shaped assembly of packed spherical particles has been previously considered [3], so at present we limit the discussion to those results that are fundamental for analyzing the more complex case of the 2D-array.

As a first point, note that the system has a finite magnetic anisotropy despite the fact that it is made with isotropic spherical particles. Indeed, despite $\Delta N_1 = 0$, $\Delta N_{Dt} \neq 0$ implying a finite magnetic shape anisotropy. This anisotropy originates from the dipolar interaction between the spherical particles and can be written in general form using equation (6.2),

$$\Delta N_{Dt} = \Delta N_2 P. \tag{6.13}$$

Clearly, for $P \to 0$ the expected limit for a single isotropic particle is recovered ($\Delta N_{Dt} = 0$), and for $P \to 1$ we obtain the shape anisotropy of the homogeneous tube of arbitrary aspect ratio $\Delta N_{Dt} = \Delta N_2$.

The anisotropy for these type of particle packing depend on the aspect ratio and the tube wall thickness, both defining the demagnetizing factor, as well as the packing fraction of the particles P. Consider first the limiting case $P = 1$ and the material is a continuous and homogeneous tube ($\beta \neq 0$) or cylinder ($\beta = 0$). This case serves as a reference to compare with previous results reported for tubes [107].

Figure 6.3 (a) shows the reduced effective anisotropy as a function of the aspect ratio for different tube wall thickness β for the particular case of the continuous tube ($P = 1$). As seen in the figure, the curves show an increase of the anisotropy with the aspect ratio. However, this increase is faster as the value of β increases, corresponding to a reduction of the tube

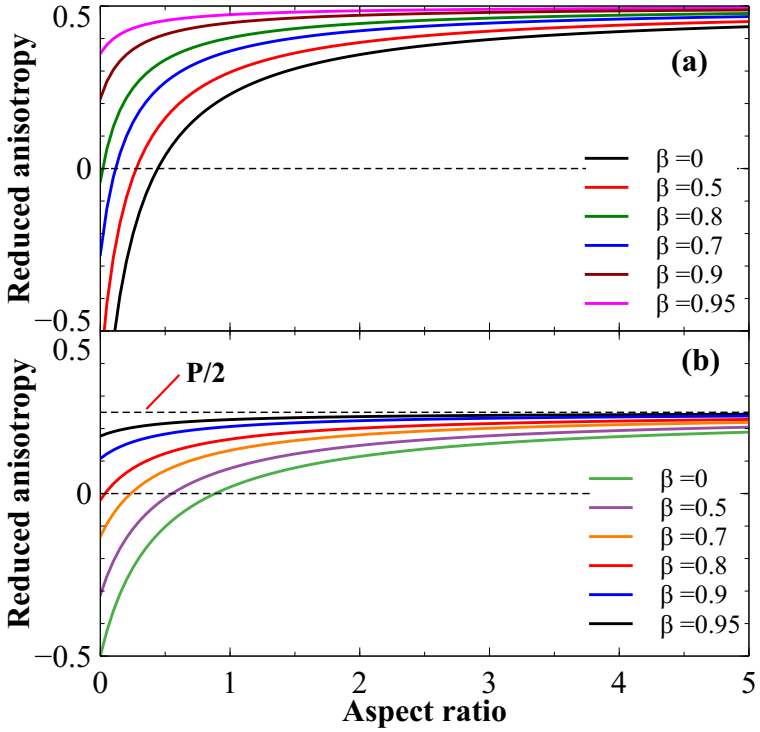

Figure 6.3: Reduced effective anisotropy as a function of the aspect ratio for different tube wall thickness β for (a) the particular case of the continuous tube ($P = 1$) and a particle volume fraction of $P = 0.5$.

wall thickness. So that a reduction of the tube wall thickness enhances the shape anisotropy of the tube [106, 107].

From the figure it can also be noted that for small values of β, the anisotropy goes from positive to negative as the aspect ratio decreases. This change in sign corresponds to a change of the easy axis direction below a critical aspect ratio. For an homogeneous (continuous) cylinder this critical value has a well-known value of $\tau = 0.906$ [107]. However, as the value of β increases, the value of the aspect ratio where the anisotropy is equal to zero decreases, and for β >0.8 it no longer reaches zero. In this case, the easy axis no longer reverses regardless of the aspect ratio. AS expected, these results ($P = 1$) are equivalent to those reported for continuous tubes [107]. Regarding the effect of the packing fraction, we note from equation (6.6) that the packing fraction is a multiplicative factor and therefore it only modulates the amplitude of the total anisotropy. As expected, the anisotropy is zero when $P = 0$, which is the case of a single isotropic sphere and it reaches its maximum value of 1/2 for $P = 1$ for large aspect ratio values. This modulating effect of the packing fraction is shown in figure 6.3 (b), where the total anisotropy as a function of the aspect ratio for different values of the tube wall thickness is shown for the particular case where P =0.5. Comparing to the results shown in figure 6.3 (a), we see the same behavior but, as expected, the amplitude is reduced. We can see that the maximum value of the anisotropy is given by

$P/2$.

To gain further insight to the role of the packing fraction the effective anisotropy was calculated as a function of the aspect ratio while keeping the value of the tube wall thickness constant (β=0.5) for different values of the packing fraction. The results are shown in figure 6.4 (a). As seen from the figure, the volume fraction simply modulates the amplitude of the anisotropy and its general variation with the aspect ratio is independent. Here we note that the point where the anisotropy is zero is the same regadless of the value of P and therefore the reorientation of the easy axis only depends on τ y β. This is clear in equation (6.6), where a change of sign in ΔN_{Dt} can only result from the quantity in the brackets.

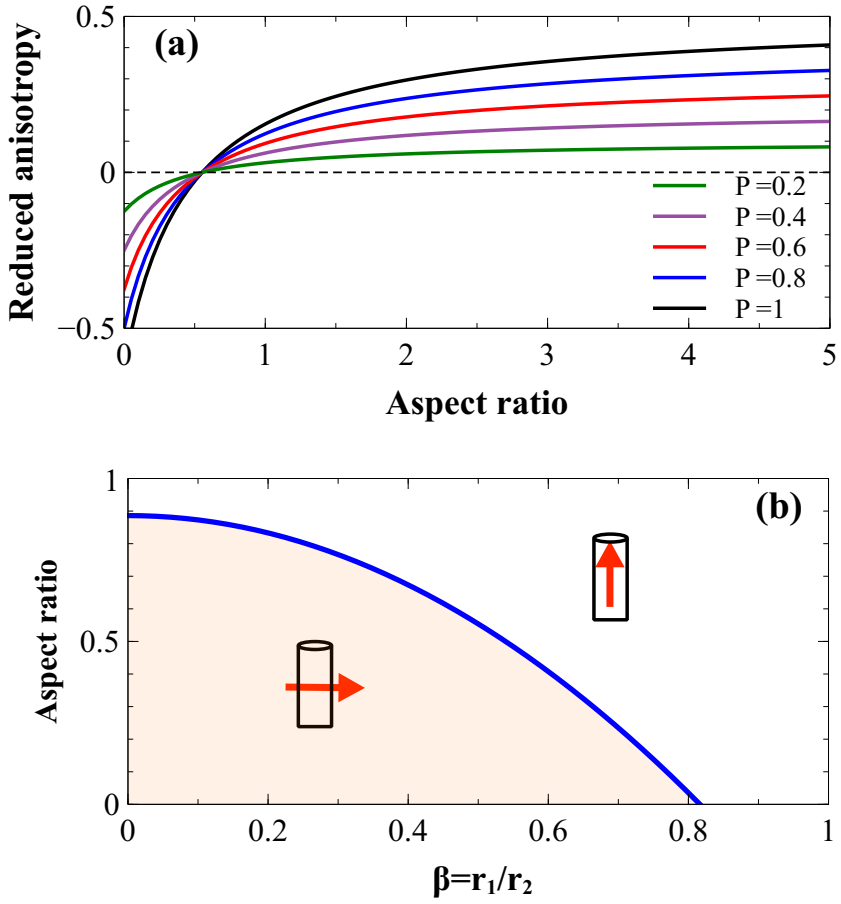

Figure 6.4: (a) Reduced effective anisotropy as a function of the aspect ratio for different values of the packing fraction (P) for the particular case of β =0.5. (b) Zero anisotropy curve, showing the critical aspect ratio value at which the anisotropy is zero as a function of the tube wall thickness β.

To find the condition for the isotropic point, we equate equation (6.6) to zero an solve for the critical aspect ratio τ_c, which is given by:

$$\tau_c = \frac{3\sqrt{\pi}}{4}\left(\frac{2}{3} - \beta^2\right) \tag{6.14}$$

This expression is equal to equation (13) in reference [107] which reflects a quadratic dependence on β. This expression can be evaluated to obtain the zero anisotropy curve for the critical aspect ratio as a function of β, which is shown in 6.4 (b). Where, as shown schematically, those values above the curve correspond to an easy axis parallel to the tube axial axis, $\Delta N_{Dt} > 0$, whole those values below the curve correspond to an easy axis perpendicular to the tube axis, $\Delta N_{Dt} < 0$. In addition, we note that the curve goes to zero at β ≈0.8. This means that above this value of β the total anisotropy has the easy axis parallel to the tube axis ($\Delta N_{Dt} > 0$) regardless of the value of the aspect ratio. This is the same result pointed out in figures 6.3 (a) and (b), where above a value of β ≈0.8 the anisotropy no longer reaches negative values. Taking $\tau_c = 0$ in equation (6.14) we obtain the value of β above which it is no longer possible to reverse the easy axis by changing the tube aspect ratio. This value is $\beta_c^2 = 2/3$ or β_c =0.82.

This condition related to the tube wall thickness (β) as well as equation (6.14) have already been identified and predicted for the case of a 2D array of homogeneous tubes [107]. However, for the cylinder shaped assembly of packed spherical particles considered herein, this diagram becomes important since it is independent of the packing fraction. This is, to tailor the easy axis direction it is only necessary to adjust τ and β following equation (6.14), regardless of the volume packing of the spherical particles.

2D array of cylinder shaped assembly of packed spherical particles

In contrast to the single tube/cylinder, the 2D array introduces additional contributions to the effective anisotropy which originate in the classical dipolar interaction between the tubes/cylinders.

Equation (6.12) shows the sum of two terms. The first one is the interaction between spherical particles in a given tube. This is the case already analyzed in the previous section. The second term is the dipolar interaction between tubes in the 2D array. The second term is always negative which indicates that this interaction term favours an easy anisotropy axis perpendicular to the tube axis, or in the *xy*-plane. The amplitud of this term is modulated by both packing fractions: P_1 of the particles in the tube and P_2 volume occupied by the tubes in the thin film containing the 2D array.

To analyze the behaviour and the effects of this second term, we have calculated separately the values of this term alone as well as the total anisotropy, equation (6.12). For this

calculation, the tube aspect ratio was kept constant at a value of $\tau = 10$, and we varied the tube wall thickness β.

The results are plotted as a function of the inverse of the reduced distance, this is $1/d$ since it is more practical. Indeed, it varies between $[0,1]$, the value $1/d = 0$ corresponds to the case were the tube and infinitely apart and the interaction goes to zero. Inversely, when $1/d = 1$ corresponds to the limiting case where the tubes touch and its the smallest possible distance between them.

Figure 6.5 (a) and (b) show the reduced interaction field, (c) and (d) reduced anisotropy as a function of the inverse reduced distance ($1/d$) for different values of the tube wall thickness β and a constant aspect ratio of τ=10. In (a) and (c) P_1=1, while in (b) and (d) were obtained for P_1=0.5.

For the interaction field between the tubes in the 2D array, figure 6.5 (a), it goes to zero when the tubes are separated ($1/d = 0$). When the distance between them is reduced, the interaction field increases following a quadratic behaviour ($1/d^2$), until reaching its highest value when the tubes come into contact ($1/d = 1$). We can see that as the tube wall thickness decreases, β increases; the magnitude of the interaction field decreases. This is similar to the effect described for a single tube in the previous section, this is, the anisotropy of the tube is reinforced when the tube wall becomes thinner.

As pointed out before, the amplitude of both terms in equation (6.12) is modulated by the factor $P_1/2$. To this end we compare the reduced interaction field for P_1=1 a P_1=0.5 in figures 6.5 (a) and (b). As expected, the same behaviour is obtained in both cases, the only change being the amplitude of the interaction field.

Regarding the effective magnetic anisotropy, this is shown in figure 6.5 (c) and (d). The overall behavior reflects the sum of the shape anisotropy, the first term in equation (6.12), and the dipolar interaction between tubes, second term in equation (6.12), which is preceded by a negative sign. As seen in the figure, the total anisotropy is maximal when the tubes are apart ($1/d = 0$) and as the distance between them is reduced, the interaction between them (with its negative sign) leads to a reduction of the total anisotropy, leading to a change in sign for certain values of β. At large separation ($1/d = 0$), the effective anisotropy reduces to that of the single (non-interacting) tube, which as discussed above, increases as the width of the tube wall decreases (β approaches 1), in agreement with the results shown in figure 6.3.

As mentioned before, the amplitude of the effective anisotropy is proportional to the packing fraction of the spheres $P_1/2$, which also defines the upper limit value of the anisotropy. This is shown as horizontal dashed lines in figure 6.5 (c) and (d). So by increasing the dis-

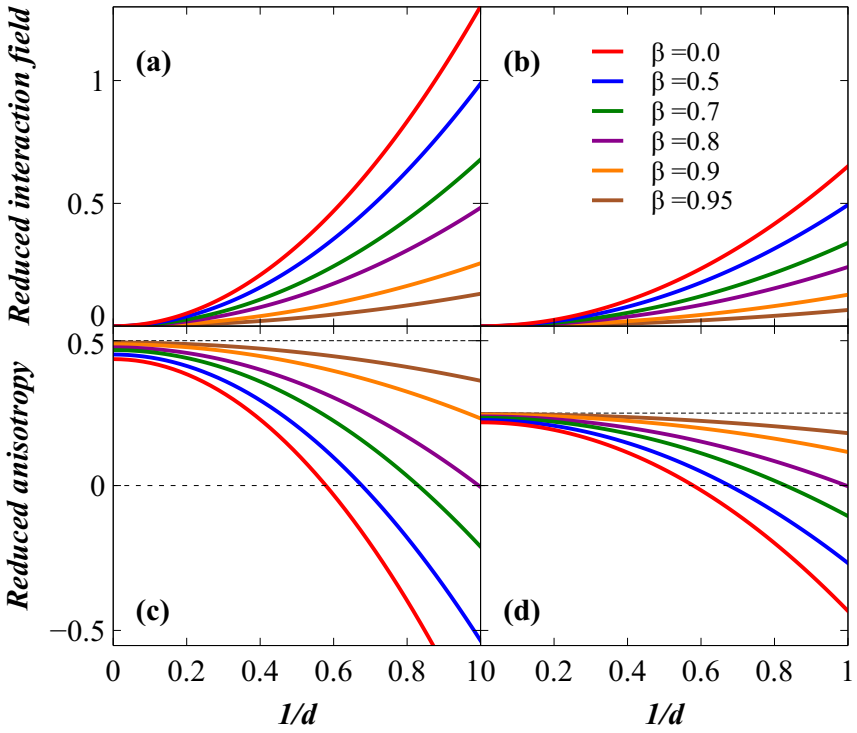

Figure 6.5: (a) and (b) Reduced interaction field, (c) and (d) reduced anisotropy as a function of the inverse reduced distance ($1/d$) for different values of the tube wall thickness β and a constant aspect ratio of τ=10. In (a) and (c) P_1=1, while in (b) and (d) were obtained for P_1=0.5.

tance between tubes, $1/d \to 0$, we see that the anisotropy tends to this upper limit and as this distance is reduced (increasing $1/d$), the anisotropy decreases as the interaction field becomes stronger. The rate at which the anisotropy decreases and changes sign, $1/d = 0$, depends on the tube wall thickness (β).

As already mentioned, the packing fraction of the particles in the tube P_1 modulates the amplitude of the effective anisotropy but its not expected to change its behaviour. To show verify this we have calculated the effective anisotropy as a function of the inverse of the reduced distance for different packing fractions of the spherical particles in the tubes with constant tube aspect ratio τ = 10 and thickness of the tube wall β =0.2. The results are shown in figure 6.6 where we verify that the volume fraction of the particles in the tube only change the amplitude of the anisotropy. For the case shown in figure 6.6 we see that the point where the anisotropy is zero is the same for all the values of P_1. This is in agreement with the results from the previous section, in particular those shown in figure 6.4 (a).

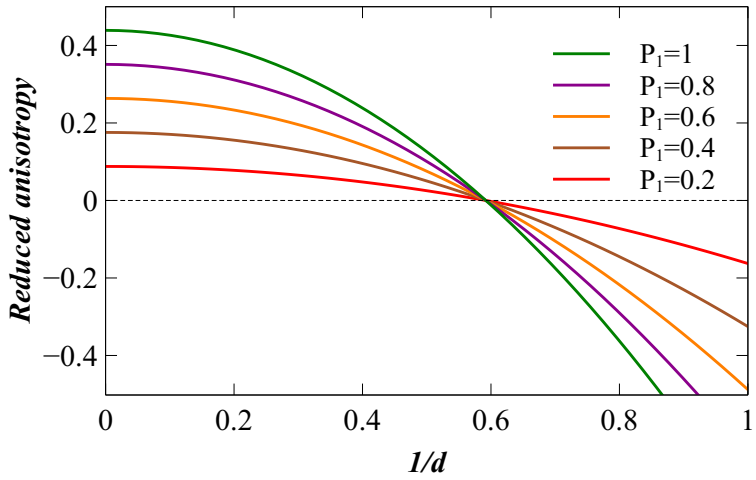

Figure 6.6: Reduced anisotropy as a function of the inverse of the reduced distance for different packing fractions of the spherical particles in the tubes (P_1) with constant tube aspect ratio $\tau = 10$ and thickness of the tube wall β =0.2.

As observed for the case of a single tube, the effective anisotropy shows a change of sign, as seen in figures 6.5 (c), (d) and 6.6. However, this does not happen above certain values of β. As before, the change in sign indicates that the easy axis direction changes from being parallel to the tube axis (positive anisotropy) to perpendicular to the axis (negative anisotropy). However, this easy axis reorientation is inhibited as the tube wall thickness decreases. To find the conditions where the effective anisotropy vanishes, we equate to zero equation (6.12) and solve to find the critical aspect ratio τ_c, leading to,

$$\tau_c = \frac{\sqrt{\pi}}{4}\left(\frac{\frac{\pi\sqrt{3}}{2d^2}\left(1-\beta^2\right)-3}{\frac{\pi\sqrt{3}}{2d^2}\left(1-\beta^2\right)-1}\left(1-\beta^2\right)-1\right). \tag{6.15}$$

This expression shows that the critical aspect ratio ($\tau_c \geq 0$) is given solely by the tube wall thickness ($0 < \beta < 1$) and the reduced distance between tubes ($d \geq 1$).

Equation (6.15) allows calculating the zero anisotropy curves for the tube aspect ratio (τ) as a function of the reduced distance between them for different values of the tube wall thickness β. Figure 6.7 shows these results.

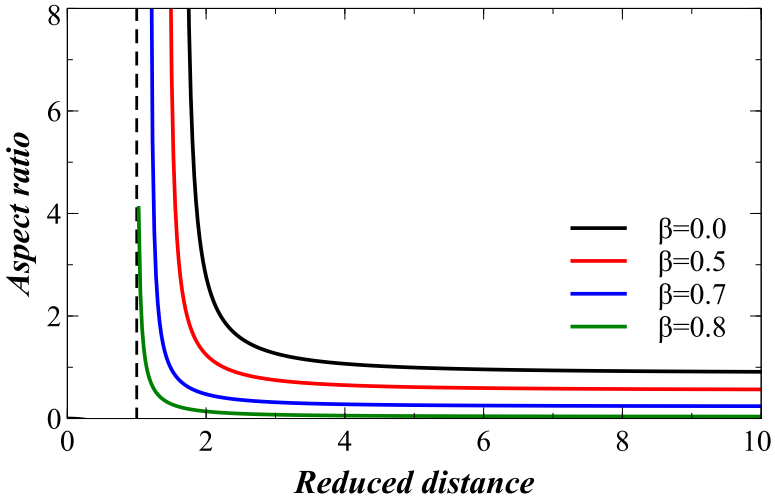

Figure 6.7: Isotropic curves for the tube aspect ratio (τ) as a function of the reduced distance between them for different values of the tube wall thickness β.

As we can see, each value of β provides a different curve. Each curve corresponds to the aspect ratio and the corresponding reduced distance for which the effective anisotropy vanishes. Point above and to the right of the curve correspond to an easy axis along the tube axis (z-axis). On the contrary, those points below the curve are those with the easy axis perpendicular to the tube axis. An important property is that, as mentioned before, reducing the tube wall thickness (increasing β) reinforces the easy axis direction along the tube axis. So that above a certain value, it is no longer possible to reverse the easy axis when the aspect ratio is decreased.

A final remark is that equation (6.15) for the 2D array of tubes made of spherical particles is the same as equation (17) in ref. [107] for the case of continuous tubes. This despite of being different systems. However, the case reported in ref. [107] is obtained as a particular case of equation (6.12) when $P_1 = 1$. In this sense, the main reason why the same expression is obtained is that the spherical particles are isotropic and therefore the do not contribute to the shape anisotropy. Indeed, as seen from equations (6.10) and (6.12), the only variable related to the spherical particles present in the effective anisotropy is their packing fraction P_1. Which as discussed above, only modulates the magnitude of the anisotropy without changing its behaviour.

To validate the model, we analyze selected experimental reports based on systems with affine geometrical features. The first case of interest is that of individual magnetic particles packed into, or confined to, a well defined geometry where the dipolar interaction between particles leads to an observable magnetic anisotropy. In these regards, there are two notable examples, the first one involves packing magnetic nanoparticles into cylinders, ideally as

shown schematically in figure 6.1 (A). In one report, Pal, et al, [108] filled carbon nanotubes with small magnetic nanoparticles. In another report, Duong, et al, [95] filled cylindrical nano holes made in a polyacrylinitrile substrate with magnetite nanoparticles. In these two studies, the magnetic characterization showed an increase of both remanence and coercive field in the cylindrically confined particles with respect to the non-confined particles. This is an indication of the presence of a magnetic anisotropy. In both cases, these effects are attributed to the enhancement of the dipolar interaction between the confined particles. The other example is the work of Merk et al [97], and Segmehl, et al, [109] who have performed the synthesis of magnetic nanoparticles within the hierarchical structure of wood. This structure is highly anisotropic with a predominant cylindrical structure as building block, similar to an array of pores aligned parallel to each other. The in-situ growth of nanoparticles from liquid solutions leads to an important fraction of the particles being fixed on the walls of the pores, leading to a tubular structure. This corresponds approximately to the situation depicted in figure 6.1 (A). In both studies, the analysis of the magnetic properties of the magnetic wood shows a magnetic anisotropy favoring an easy axis parallel to the symmetry axis of the tubes. This anisotropy is attributed to the dipolar interaction between particles that are confined to the tubular shape. In the context of our model, this follows from either equation (3) or (6), where it is clear that a finite magnetostatic anisotropy arises from the dipolar interaction between the particles. Moreover, from equation (3) we see that the magnitude of the resulting anisotropy is a function of the cylinder aspect ratio (N_z) and the packing fraction (P) of the particles. For the more complex case of analyzing the inter-cylinder dipolar interaction, these studies do not explore experimentally these effects, although they recognize its importance.

The model is also well suited for 2D arrays of magnetic nanowires grown by electrodeposition into nanoporous templates. These are 2D arrays of circular cylinders, arranged so that their long exes are parallel to each other and distributed spatially forming a film. In this case, the geometrical features are the circular cylinder and the thin film containing the 2D array. For this system, equation (6.12) needs to be simplified by taking $P_1 = 1$ corresponding to ideal case of a continuous magnetic material and then, to treat the case of a homogeneous cylinder, we need to take $\beta = 0$. Leaving only a dependence on the wire aspect ratio and the distance between wires, this is,

$$\Delta N_{Dt} = \frac{1}{2}\left[1 - \frac{3}{1+\frac{4\tau}{\sqrt{\pi}}}\right] - \frac{\pi\sqrt{3}}{4d^2}\left[1 - \frac{1}{1+\frac{4\tau}{\sqrt{\pi}}}\right] \tag{6.16}$$

This expression shows the competition between two terms: (a) the shape anisotropy which favors an easy axis parallel to the wires long axis (z) and (b) the dipolar interaction between wires, which due to the negative sign preceding it, favors an easy axis perpendicular to the long axis of the wires. The effective anisotropy of the system, in the absence of other anisotropy contributions, is the result of this competition. In this sense, a well known effect observed in arrays of NWs is the rotation of the easy axis from parallel

to perpendicular to the long axis of the wires when the dipolar interaction overcomes the shape anisotropy [110, 111]. For the case of an array of continuous cylindrical NWs, the expression defining the easy axis rotation is given by equation 6.15 for $\beta = 0$. In this case, it only depends on the interwire distance and the aspect ratio of the wires. As mentioned above, this leads to a curve defining the limit where the system is isotropic, this is, where the shape anisotropy of the single wire and the dipolar interaction cancel out and the effective anisotropy of the system is zero.

This effect can be analyzed using the model and comparing it with reported experimental results where the easy axis is shown to rotate as a function of either the distance between wires or their aspect ratio. To this end, we have selected data for Ni [4–6] and NiFe [7] NWs in order to avoid other materials that can have other magnetic anisotropy contributions.

Figure 6.8 (a) shows the easy axis diagram as a function of the aspect ratio and the inverse of the reduced distance. The continuous curve corresponds to equation 6.15 for $\beta = 0$. The horizontal dashed line at $1/d$= 0.606 corresponds to the distance for the critical packing fraction of $P_2 = 1/3$ in an hexagonal array at which the easy axis rotates for the limiting case of infinitely tall nanowires [111]. Notice that this is the value at which the continuous curve tends asymptotically. In this diagram, the region above and to the left side of the curve, corresponds to an easy axis parallel to the long axis of the wires. The region below and to the right of the curve, corresponds to the case where the easy axis is perpendicular to the long axis of the wires.

Consider first the experimental data for the case when the aspect ratio is varied while keeping constant the distance between wires [4, 5]. As seen in the figure, the easy axis rotates from parallel to perpendicular to the cylinder axis when the aspect ratio is reduced. Moreover, as seen from the two series of data shown in the figure, the aspect ratio at which the transition takes place is lower for larger interwire distance ($1/d \to 0$). The easy axis rotation is conditioned by the wires having an easy axis parallel to the symmetry axis. For a single, non-interacting, cylinder this requires an aspect ratio larger than 0.91, since at this point the system is isotropic. Wires with aspect ratios larger but close to the critical value require a small interaction field to reverse the easy axis.

As the wire aspect ratio increases, the distance between wires required to reverse the easy axis needs to be reduced ($1/d$ increases) in order to increase the strength of the interaction field. The largest value of the shape anisotropy for the circular cylinder is attained when the aspect ratio is very large. In this case, as mentioned before, the axis axis rotates when the packing fraction is larger than 1/3. This is seen in figure 6.8 (a) for the data corresponding to those series of samples where the packing fraction is larger than 1/3 [4,6,7]. Furthermore, we can see that the easy axis rotation takes place at different aspect ratio values. The predictions of the model are in excellent agreement with the experimental results.

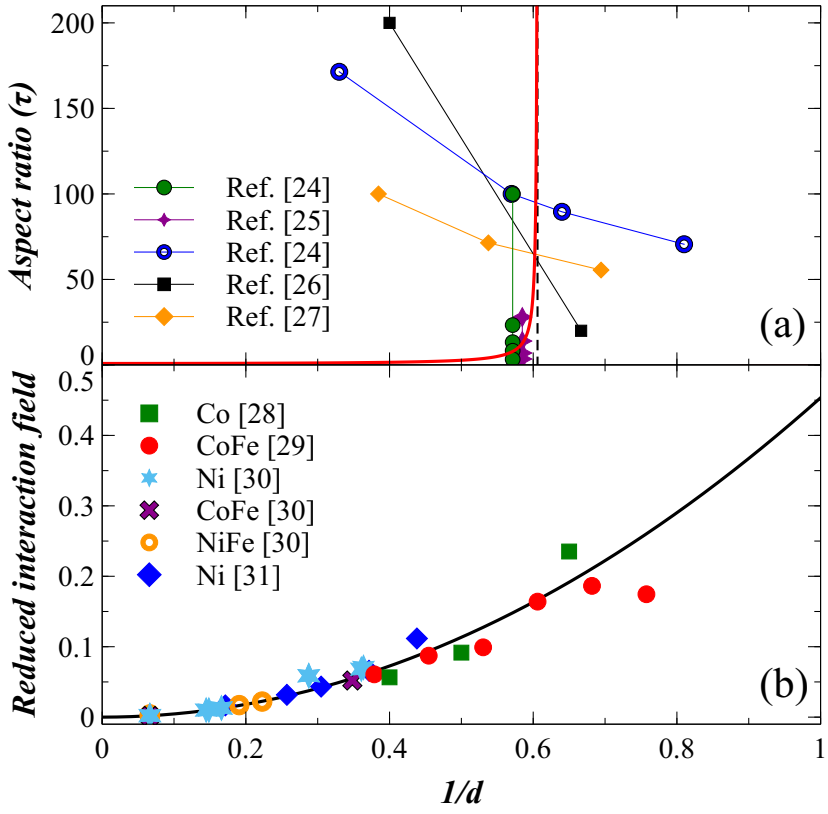

Figure 6.8: (a) Effective anisotropy diagram for an array of nanowires as a function of the wire aspect ratio (τ) and the inverse reduced distance ($1/d$). The continuous line corresponds to the model, equation (6.16). The horizontal dashed line at $1/d$= 0.606 corresponds to the distance for the critical packing fraction of $P_2 = 1/3$ in an hexagonal array. The data points correspond to examples of Ni [4–6] and NiFe [7] NWs. (b) Axial component of the reduced interaction field calculated from the model (continuous line) and compared to experimental results reported for arrays of very tall nanowires [8–11].

The other measurements that can be compared with the model are those of the axial component of the dipolar interaction field. To compare the model with available experimental results on arrays of tall NWs, we have taken the date obtained using FORC diagrams for Co (M_S =1400 emu/cm^3) [8] and CoFe (M_S =1991.5 emu/cm^3) [9], as well as those obtained using remanence curves in Ni (M_S =485 emu/cm^3), NiFe (M_S =788 emu/cm^3) and CoFe (M_S =1900 emu/cm^3) NWs with diameters of 71 nm and below [10]. In addition, we have extracted the data obtained from the width of the switching field distribution (SFD) for Ni NWs [11]. To obtain the value of the interaction field from the width of the SFD we assume that the reported width w is the sum of the constant intrinsic width w_0 and the shearing due to the interaction field $H_{int}(d)$, this is, $w = w_0 + H_{int}(d)$. By interpolating the data for infinite separation between NWs ($H_{int} = 0$), we obtain w_0 so that $H_{int}(d) = w - w_0$.

The values reported in these studies correspond to the interaction term of the axial com-

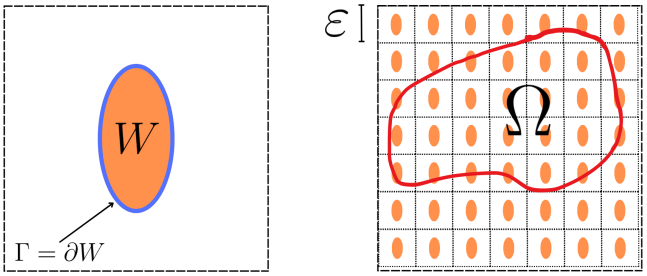

Figure 6.9: Sketch of the model used to homogenize a system of magnetic SW nanoparticles.

ponent of the interaction field [103], so to convert these values to dimensionless effective field, we have divided their magnitude by $4\pi M_s$ (CGS) or $\mu_0 M_s$ (MKS), using the values of M_S mentioned above. Moreover, equation (6.16) is the total effective anisotropy field, so to obtain the axial component, we have to divide the second term by 3 [103]. The axial component of the interaction field is given by the second term in equation (6.16), which for infinitely tall NWs, requires taking $\tau \to \infty$. By doing so, and using the inverse of the reduced distance, we can compare a single interaction curve for all the experimental points as shown in figure 6.8 (b). Here, the continuous line corresponds to the model while the points correspond to the experimental data. As seen in the figure, the entire data set shows a very good agreement with the model.

6.2 Homogenization of a system of magnetic nanoparticles

In this section, we choose a representative elementary volume (REV) of a certain lattice of single-domain magnetic nanoparticles in vacuum, and then, we use the asymptotic homogenization technique to extend the theory to study the characteristics of a bulk material made of an array of the REV that we previously choose. We have made this process by two methods: the first one is the asymptotic homogenization technique. Although is a valid method to approximate a bulk property from the microscopic characteristics, we decided to go on the second method: the two-scale homogenization technique. This, as the two-scale homogenization has more mathematical formality.

6.2.1 Asymptotic homogenization for a lattice of magnetic nanoparticles

We start with a configuration like the one in figure 6.9, where the blue line in the left panel indicates the boundary (Γ) between the magnetic material and vacuum and the red line in the right panel indicates an arbitrary REV.

The goal of this exercise if to obtain an homogenized form of the demagnetization field operator. In order to do so, we start by obtaining an expression for the magnetostatic scalar potential u, which is solution to

$$\text{Problem} \begin{cases} -\triangle u(x) = -\nabla \cdot \vec{m}(x) \\ H_d(\vec{m}) = \nabla u(\vec{m}). \end{cases} \tag{6.17}$$

Now, to start with the asymptotic homogenization we assume that exist a solution in the form

$$u^{\varepsilon}(x) = \sum_{i=0}^{\infty} \varepsilon^i u_i(x,y), \tag{6.18}$$

and that the nabla operator converges to

$$\nabla u_i = \nabla_x u_i + \frac{1}{\varepsilon} \nabla_y u_i \tag{6.19}$$

and least but not at least, we propose the magnetization as

$$\vec{m}(x) = \chi(\frac{x}{\varepsilon}) \vec{m}_0(x), \tag{6.20}$$

where χ is a characteristic function of the position of the material. This is, $\chi(x) = 1$ if $x \in W$ and $\chi = 0$ if $x \notin W$. The next step is to substitute the assumptions that we have made just above into the problem shown in equation (6.17) to get

$$\begin{aligned} \chi(x/\varepsilon)\nabla_x \cdot m_0(x) + \tfrac{1}{\varepsilon} m_0 \cdot \nabla_y \chi(x\varepsilon) &= \\ &+ \varepsilon^{-2}[\triangle_y u_0] \\ &+ \varepsilon^{-1}[\triangle_y u_1 + \nabla_y \nabla_x u_0 + \nabla_x \nabla_y u_0] \\ &+ \varepsilon^{0}[\triangle_x u_0 + \nabla_x \nabla_y u_1 + \nabla_y \nabla_x u_1 + \triangle_y u_2] \end{aligned} \tag{6.21}$$

Now, for the equation to be true, we need it to be true for every power of ε. Therefore, this leaves us with the next system of equations

$$\begin{aligned} \triangle_y u_0 = &\quad 0 \\ \triangle_y u_1 + \nabla_y \cdot \nabla_x u_0 + \nabla_x \cdot \nabla_y u_0 = &\quad \vec{m}_0 \cdot \nabla_y \chi(x/\varepsilon) \\ \triangle_x u_0 + \nabla_x \cdot \nabla_y u_1 + \nabla_y \cdot \nabla_x u_1 + \triangle_y u_2 = &\quad \chi(x/\varepsilon)\nabla_x \cdot \vec{m}_0(x) \end{aligned} \tag{6.22}$$

And from the first one we can conclude that

$$u_0(x,y) = u_0(x). \tag{6.23}$$

So if we put this information in the second equation, we get that

$$\nabla_y \cdot (\nabla_y u_1 - \vec{m}_0 \chi(y)) = 0 \tag{6.24}$$

Which leads us to

$$u_1(x,y) = \sum_i \omega_i(y) m_{0i}(x) = \vec{\omega} \cdot \vec{m}_0 \tag{6.25}$$

If we put the above information into the equation (6.24) we get

$$\nabla_y \cdot \begin{pmatrix} \partial_{y1}\omega_1 - \chi & \partial_{y1}\omega_2 \\ \partial_{y2}\omega_1 & \partial_{y2}\omega_2 - \chi \end{pmatrix} \begin{pmatrix} m_{01} \\ m_{02} \end{pmatrix} = 0 \tag{6.26}$$

Which is precisely the

$$\text{Cell Problem} \begin{cases} \nabla_y \cdot [\nabla_y \omega_i - \vec{e}_i \chi] = 0, \text{ in C} \\ \omega_i \text{ periodic in } \partial \text{C} \end{cases} \tag{6.27}$$

Where C represents the *Cell*, this is, the particle W inside $\Omega = (0,1)^2$ which is completely empty.

Now, for the equation corresponding to ε^0 we have

$$\triangle_y u_2 = \chi \nabla_x \cdot \vec{m}_0 - \triangle_x u_0 - \nabla_x \cdot (\nabla_y u_1) - \nabla_y \cdot (\nabla_x u_1) \tag{6.28}$$

And by the Fredholm alternative (condition) [112] this equation has solution if and only if

$$\int_C \underbrace{[\chi \nabla_x \cdot \vec{m}_0 - \triangle_x u_0 - \nabla_x \cdot (\nabla_y u_1) + \nabla_y \cdot (\nabla_x u_1)]}_{=0} dy = 0 \tag{6.29}$$

where the last term in the right side of the equation is zero by means of a proof that can be found in the appendix A.

Therefore,

$$-\triangle_x u_0 |C| = -|C| \nabla_x \cdot \vec{m}_0(x) + \int_C \nabla_x \cdot \nabla_y u_1 dy - \underbrace{\int_C \nabla_y \cdot \nabla_x u_1 dy}_{=0}, \tag{6.30}$$

Then,

$$\begin{aligned} -\triangle_x u_0 |C| &= -|C| \nabla_x \cdot \vec{m}_0(x) \\ &= -\nabla_x \cdot \left(|C| \vec{m}_0(x) - \int_Y \nabla_y u_1 \right) \\ &= -\nabla_x \cdot (|C| I_d - \hat{W}) \vec{m}_0. \end{aligned} \tag{6.31}$$

Where we have used the fact that

$$\int_Y \nabla_y u_1 = \underbrace{\begin{pmatrix} \int_Y \partial_{y1} \omega_1 dy & \int_Y \partial_{y1} \omega_2 dy \\ \int_Y \partial_{y2} \omega_1 dy & \int_Y \partial_{y2} \omega_2 dy \end{pmatrix}}_{=\hat{W}} \begin{pmatrix} m_{01} \\ m_{02}. \end{pmatrix} \tag{6.32}$$

From here is easy to see that

$$-\triangle_x u_0 = -\nabla_x \cdot (I_d |C| + \hat{W}) \vec{m}_0 \tag{6.33}$$

And by definition of the problem

$$-\triangle u = -\nabla \cdot \vec{m} \mid H_d(\vec{m} = \nabla u(\vec{m})) \tag{6.34}$$

So finally we can conclude that

$$\triangle u = H^{Hom}(\vec{m}_0) = \nabla_x u_0 + \hat{W}\vec{m}_0, \tag{6.35}$$

Where we can identify $\nabla_x u_0 = H(\vec{m}_0)$. And then, as expected, we have found the correction term to the magnetic demagnetization operator which depends only on the geometry of the particles, the volume fraction of the particle ($|C|$). But, this still is a naive approximation as we expected to see a term that models the interaction between the particles in different cells. For this, is necessary to use a more mathematical sound as the two-scale convergence.

6.2.2 Two-scale homogenization to a system of magnetic nanoparticles

We begin explaining the model that we use to calculate the demagnetization operator field. A sketch of the model can be found in figure 6.9. We are assuming a 3D system in which the particle W is an ellipsoid and satisfies that

$$W \subset Q = (0,1)^3$$

where $\Gamma = \partial W$ is the boundary of the ellipsoid and $Q = (0,1)^3$ is a unit periodic cell in $\mathbb{R}^3$ and $\theta = |W|$ is the volume fraction of magnetic material in the unit cell.

Let $\varepsilon << 1$ and $\Omega \in \mathbb{R}^3$, then, inside Ω we have a crystallilne array of particles such that

$$\Omega_p^\varepsilon = \{x \in \Omega \mid \frac{x}{\varepsilon} \in W\}$$
$$\Gamma^\varepsilon = \{x \in \Omega \mid \frac{x}{\varepsilon} \in \Gamma$$

and outside the particles we have free space denoted by

$$\Omega_\varepsilon = \Omega \setminus \Omega_p^\varepsilon.$$

Now, since the ellipsoid W and $|W_\varepsilon| \approx \varepsilon << 1$, then m must be constant on each W_ε. With this in mind, we let

$$m^{\varepsilon}(x) = \sum_{k \in I_{\varepsilon}} m_k \chi_Q \left(\frac{x}{\varepsilon} - k \right) \tag{6.36}$$

where $I_{\varepsilon} = \{k \in \mathbb{Z}^3 \mid \frac{k}{\varepsilon} \in \Omega\}$.

Also, inside each particle $k \in I_{\varepsilon}$

$$\mathcal{H} = -N_W m_k$$

where $N_k \in \mathbb{R}^{3\times 3}$ is the demagnetization factor of W such that $Tr(N_W) = 4\pi$.

Now, let u^{ε} be the solution of

$$\begin{cases} -\nabla^2 u^{\varepsilon} = 0 \quad \text{in} \quad \mathbb{R}^3 \setminus \Omega_p^{\varepsilon} \\ \frac{\partial u^{\varepsilon}}{\partial \nu} = \nu \cdot [(I - N_W) m^{\varepsilon}] \quad \text{on} \quad \Gamma^{\varepsilon} \end{cases} \tag{6.37}$$

Then the demagnetization field operator will be given by

$$\mathcal{H}^{\varepsilon}(m^{\varepsilon}) = \chi_{\mathbb{R}^3 \setminus \Omega_p^{\varepsilon}} \nabla u^{\varepsilon} + \chi \Omega_p^{\varepsilon} N_W m^{\varepsilon} \quad \text{in} \quad \mathbb{R}^3 \tag{6.38}$$

The task at hand is to compute the limit of the above operator when $\varepsilon \to 0$. For this end, we are going to build some concepts.

Definition 6.2.1 (Two-scale convergence)**.** We can say that $u^{\varepsilon} \in L^2(\Omega)$ two-scale converges to $u_0(x,y) \in L^2(\Omega \times Q)$ if

$$\lim_{\varepsilon \to 0} \int_{\Omega} u^{\varepsilon}(x) \phi(x, \frac{x}{\varepsilon}) dx = \int_{\Omega} \int_{Q} u_0(x,y) \phi(x,y) dy dx \quad \forall \phi \in C[\bar{\Omega}; C_{\#}(Q)].$$

This is written in short as $u^{\varepsilon} \to^{2s} u_0$

Theorem 6.2.1. Let $u^{\varepsilon} \in L^2(\Omega)$ be uniformly bounded. Then, exist some $u_0(x,y) \in L^2(\Omega \times Q)$ such that

$$u^{\varepsilon} \to^{2s} u_0$$

Theorem 6.2.2. Let $u^{\varepsilon}H^1(\Omega)$ be uniformly bounded such that

$$u^{\varepsilon} \to u \quad \text{weakly in} \quad L^2(\Omega)$$

then exists some $u_1(x,y) \in L^2(\Omega, H^1_{\#}(Q))$ such that

$$\nabla_x u^{\varepsilon} \to^{2s} \nabla_x u_0(x) + \nabla_y u_1(x,y).$$

With this tools in hand we proceed to compute the above mentioned limit. Let $\{m^{\varepsilon}(x), \mathcal{H}^{\varepsilon}(m^{\varepsilon})\}$, then $m^{\varepsilon} \to m$ in $L^2(\Omega)$ and $\mathcal{H}^{\varepsilon}(m^{\varepsilon}) \to^{2s} \bar{\mathcal{H}}(m)$ where

$$\bar{\mathcal{H}}(x,y) = -\chi_{Q\setminus W}(y)[\nabla_x u(x) + \nabla_y u_1(x,y)] + \chi_W(y) N_W m(x) \tag{6.39}$$

where u is a solution of

$$\begin{cases} - & \triangle u = 0 \quad \text{in} \quad \mathbb{R}^3 \setminus \Omega \\ - & \nabla \cdot [(I_d - D)\nabla u] = -\nabla \cdot \left[\left(\frac{1}{1-\theta} I_d + N_W \right) m \right] \quad \text{on} \quad \Omega \\ & \nu \cdot [(I_d - D)\nabla u \mid_{in} - \nabla u \mid_{out}] = \nu \cdot \left(\frac{1}{1-\theta} I_d + N_W \right) m \quad \text{on} \quad \partial\Omega \end{cases} \tag{6.40}$$

and

$$u_1 = -\omega \cdot [\nabla u + (I_d - N_W) m(x)] \tag{6.41}$$

and $\omega = (\omega_1, \omega_2, \omega_3)$ are solutions of the cell problem

$$\begin{cases} -\triangle_y \omega_i = 0 \quad \text{in} \quad Q \setminus W \\ \frac{\partial \omega_i}{\partial \nu_i} = \nu \cdot e_i \quad \text{on} \quad \Gamma \\ \omega_i \quad \text{is Q-periodic} \quad \text{on} \quad \partial Q \end{cases} \tag{6.42}$$

and representing the proxy of interaction we have

$$D = \int_{Q\setminus W} (D\omega(y))^T dy \tag{6.43}$$

Later, with that has been declared in this section we can get to homogenize the micromagnetic energy. In this fashion, let the micromagnetic energy be written as

$$\begin{aligned} E^{\varepsilon}(m^{\varepsilon}) &= \frac{1}{2}\int_{\mathbb{R}^3} \mathcal{H}^{\varepsilon}(m^{\varepsilon})\cdot\mathcal{H}^{\varepsilon}(m^{\varepsilon})dx - \int_{\Omega_p^{\varepsilon}} m^{\varepsilon}\cdot h_{ext}dx \\ &= \frac{1}{2}\int_{\Omega_p^{\varepsilon}} m^{\varepsilon}\cdot\mathcal{H}^{\varepsilon}(m^{\varepsilon})dx - \int_{\Omega_p^{\varepsilon}} m^{\varepsilon}\cdot h_{ext}dx \end{aligned} \tag{6.44}$$

Then, as $\varepsilon \to 0$ the micromagnetic energy converges to

$$\begin{aligned} \bar{E}(m) &= -\frac{1}{2}\int_{\Omega} m\cdot\left(\int_Q \bar{\mathcal{H}}(m)dy\right)dx - \theta\int_{\Omega} m\cdot h_{ext}dx \\ &= \frac{1}{2}\int_{\Omega} m\cdot((1-\theta)(N_1\nabla u + N_2 m) + \theta(N_W m))\,dx - \theta\int_{\Omega} m\cdot h_{ext}dx \end{aligned} \tag{6.45}$$

where

$$N_1 = (I_d - D) \quad \text{and} \quad N_2 = D(I_d - N_W) \quad \text{in} \quad \mathbb{R}^{3\times 3}, \tag{6.46}$$

In such fashion that D and N_1 are a measure of the interaction between the particles and N_W and N_2 are taking into account the shape of the particles W. Finally, to interpret this results let us assume that we are working with a macroscopic thin film such that $\nabla u \to \mathcal{H}_{stray}$. Then,

$$-\mathcal{H}_{stray} = \left(\underbrace{(1-\theta)N_\Omega + \theta N_W)}_{\text{as in literature}} + \underbrace{(1-\theta)D(I_d - N_w - N_\Omega)}_{\text{correction term}}\right) m \tag{6.47}$$

From this last equation is easy to see that the correction term decreases when the ratio of the semiaxis of the particles (a/b) tends to unity. Also, the correction term becomes significant when this ratio becomes smaller, this is, when the particle takes an oblate form.

Chapter 7

Conclusions and future work

Once we have stated all the results that have been obtained, we shall review the most remarkable results obtained in the current research.

First of all, we have successfully developed a mathematical model that get the averaged properties of magnetic systems. In particular, we have obtained an analytical expression for the effective magnetic anisotropy. As a limitation to this work, the model describes the properties of only two configurations: a system made up spherical particles which in turn are arranged into cylinders; and a system made up of spherical particles which in turn are arranged inside a hollow tube. Despite of the limitations of the model, we have proved the usefulness of the model as we compared with experimental results to obtain remarkable concordance. Also, we found that for cylindrical arrangements like the above mentioned, the geometry of the volume containing the particles leads to a magnetic anisotropy that corresponds to the dipolar interactions ignoring the fact that the particles in the arrangement are isotropic.

Next, as an expansion of the mean-field model, we developed a more rigorous model based on homogenization techniques. First, we used the asymptotic homogenization technique to find an analytical expression for the demagnetization field operator for a system made up of a particle with an arbitrary shape that repeats itself over a representative element of volume (REV), and this REV repeats over space to the extent of the bulk material. Finally, we extend our analysis of such a system by means of the two-scale homogenization technique. This turned out as an analytical expression for the stray-field operator which corresponds exactly with the known expression in literature for the stray-field operator plus a correction term that is related to the proxy of interaction between the particles inside the cell given its shape and arrangement.

The above mentioned shed light into the study and analysis of magnetic systems depending on whether the particles of the system are identical or if each particle has a singular geometry. For the first, we shall use the mean-field model which has proved to be accurate and for the last, we shall use the homogenized model as it has been designed specifically to treat the geometry of each particle inside the analytical expressions.

As a matter of fact, we have corroborated the hiphothesys as we have created a numerical scheme based on the minimization of the micromagnetic energy which determines the configuration of the individual magnetization of each particle that corresponds to a local minimum in the micromagnetic energy. Hence, we can obtain the equilibrium configuration of the individual magnetization that corresponds to a stable state.

Later, we have already implemented this numerical scheme into a programming language, *FreeFEM++*. This enables the code to run in Windows, OsX and Linux using open source libraries. Also, the software runs in a normal CPU, hence not requiring expensive hardware nor advanced coding skills. And last but not least, the code can be downloaded for free, allowing the scientific community to develop and grow the code into their particular necessities.

In perspectives, we aim to extend the analytical model to more complex systems such as geometries in three dimensions, more types of boundary conditions, and maybe, autosimilar or fractal structures in which we could analyze the unit cell and get conclusions on what the properties of such a system might be. With regard to the numerical results, we aim to implement our algorithms into the most modern platforms for coding and computing. Also, we are willing to test our results on the homogenized model versus experimental data to see the reach of the model and the possible usefulness that could acquire in the near future. Finally, we are interested in use the geometrical optimization techniques to obtain the best geometry which maximize a certain feature of the material. Then, the above mentioned will serve as a guide to know a priori the optimal geometrical configuration that an array of magnetic particles must have in order to attain a desirable property.

Appendix A

Appendix: proofs

We want to prove that

$$\int_Y \nabla_y \cdot (A\nabla_x u^1) dy = 0$$

First we note that we can write $A\nabla_x u^1$ can be written as

$$A\nabla_x u^1 = \begin{pmatrix} \omega^1 A_{11}\partial^2_{x1}u^0 + \omega^1 A_{12}\partial_{x1}\partial x2u^0 + \omega^2 A_{11}\partial_{x1}\partial x2u^0 + \omega^2 A_{12}\partial^2_{x2}u^0 \\ \omega^1 A_{21}\partial^2_{x1}u^0 + \omega^1 A_{22}\partial_{x1}\partial x2u^0 + \omega^2 A_{21}\partial_{x2}\partial x1u^0 + \omega^2 A_{22}\partial^2_{x2}u^0 \end{pmatrix} \tag{A.1}$$

then

$$\begin{aligned} \nabla_y \cdot (A\nabla_x u^1) =& \nabla_y \cdot [(A_{11},A_{21})\omega^1]\partial^2_{x1}u^0 + \nabla_y \cdot [(A_{12},A_{22})\omega^1]\partial_{x1}\partial_{x2}u^0 \\ &+ \nabla_y \cdot [(A_{11},A_{21})\omega^2]\partial_{x2}\partial_{x1}u^0 + \nabla_y \cdot [(A_{12},A_{22})\omega^2]\partial^2_{xx}u^0 \end{aligned} \tag{A.2}$$

and also

$$\nabla_y \cdot (A\nabla_x u^1) = \begin{pmatrix} \nabla_y \cdot [(A_{11},A_{21})\omega^1] & \nabla_y \cdot [(A_{12},A_{22})\omega^1] \\ \nabla_y \cdot [(A_{11},A_{21})\omega^2] & \nabla_y \cdot [(A_{12},A_{22})\omega^2] \end{pmatrix} : D^2_x u^0 = A' : D^2_x u^0 \tag{A.3}$$

where D^2_x us the Hessian applied to u^0; Now from the equation

$$\int_Y \left(\nabla_y \cdot (A\nabla_x u^1) + \nabla_x \cdot (A\nabla_y u^1 + A\nabla_x u^0\right) dy = f(x) \tag{A.4}$$

we integrate each element of the matrix. This results in elements of the form

$$\int_Y A_{ij} dy = \int_y \nabla_y \cdot [(A_{11},A_{21}\omega^1)] dy \tag{A.5}$$

Using the Divergence theorem this becomes

$$\int_{\partial Y} \nu \cdot (e_i A\omega) dy = 0 \tag{A.6}$$

this is naught due to the periodicity of A and ω in the micro-domain.Therefore

$$\int_{Y} \nabla_y \cdot (A\nabla_x u^1) dy = 0 \tag{A.7}$$

Bibliography

[1] R. Walser, "Metamaterials: An introduction," in *Introduction to Complex Mediums for Optics and Electromagnetics*, pp. 295–316, SPIE, 2003.

[2] W. Lin, *Diversity, Biomineralization and Rock Magnetism of Magnetotactic Bacteria*. Springer-Verlag Berlin Heidelberg, 2013.

[3] K. Hintze Maldonado, *Tesis del kevin*. PhD thesis, Instituto Potosino de Investigación Científica y Tecnológica, 2023.

[4] G. Kartopu, O. Yalçın, K.-L. Choy, R. Topkaya, S. Kazan, and B. Aktaş, "Size effects and origin of easy-axis in nickel nanowire arrays," *J. Appl. Phys.*, vol. 109, p. 033909, feb 2011.

[5] B. Das, K. Mandal, P. Sen, and S. K. Bandopadhyay, "Effect of aspect ratio on the magnetic properties of nickel nanowires," *J. Appl. Phys.*, vol. 103, p. 013908, jan 2008.

[6] S. Khalid, R. Sharif, and Z. H. Shah, "TAILORING OF MAGNETIC EASY AXIS OF NICKEL NANOWIRES BY VARYING DIAMETER," *Surf. Rev. Lett.*, vol. 23, p. 1650024, jan 2016.

[7] E. V. Tartakovskaya, M. Pardavi-Horvath, and M. Vázquez, "Configurational spin reorientation phase transition in magnetic nanowire arrays," *J. Magn. Magn. Mater.*, vol. 322, pp. 743–747, mar 2010.

[8] M. P. Proenca, K. J. Merazzo, L. G. Vivas, D. C. Leitao, C. T. Sousa, J. Ventura, J. P. Araujo, and M. Vazquez, "Co nanostructures in ordered templates: comparative FORC analysis," *Nanotechnology*, vol. 24, p. 475703, oct 2013.

[9] S. Alikhanzadeh-Arani, M. Almasi-Kashi, and A. Ramazani, "Magnetic characterization of FeCo nanowire arrays by first-order reversal curves," *Curr. Appl. Phys.*, vol. 13, pp. 664–669, jun 2013.

[10] Y. G. Velázquez, A. L. Guerrero, J. M. Martínez, E. Araujo, M. R. Tabasum, B. Nysten, L. Piraux, and A. Encinas, "Relation of the average interaction field with the coercive and interaction field distributions in First order reversal curve diagrams of nanowire arrays," *Sci. Rep.*, vol. 10, pp. 1–11, dec 2020.

[11] S. Da Col, M. Darques, O. Fruchart, and L. Cagnon, "Reduction of magnetostatic interactions in self-organized arrays of nickel nanowires using atomic layer deposition," *Appl. Phys. Lett.*, vol. 98, p. 112501, mar 2011.

[12] L. Exl, D. Suess, and T. Schrefl, "Handbook of magnetism and magnetic materials," in *Handbook of Magnetism and Magnetic Materials*, pp. 1–44, Springer International Publishing, 2021.

[13] B. Eliezer and L. De la Pena, *Electromagnetismo: de la ciencia a la tecnologia*. cdmx, Mexico: Fondo de cultura economica, 2001.

[14] R. P. Feynman, R. B. Leighton, and M. L. Sands, *The feynman lectures on physics: Mainly electromagnetism and matter*. Addison-Wesley, 1964.

[15] J. Trefil, *The nature of science: An A-Z guide to the laws and principles governing our universe*. Houghton Mifflin Co., 2003.

[16] D. Mattis, *History of Magnetism*. Berlin, Heidelberg: Springer Berlin Heidelberg, 1981.

[17] B. Bunch and A. Hellemans, *The timetables of science: A chronology of the most important people and events in the history of Science*. Simon and Schuster, 1991.

[18] A. Aharoni, *Introduction to the theory of ferromagnetism*. Oxford University Press, 2007.

[19] E. A. Azizov, "Tokamaks: From a d sakharov to the present (the 60-year history of tokamaks)," *Physics-Uspekhi*, no. 2, 2012.

[20] U. Enz, "Chapter 1 magnetism and magnetic materials: Historical developments and present role in industry and technology," Handbook of Ferromagnetic Materials, Elsevier, 1982.

[21] P. A. Kruzik M, "Recent developments in the modeling, analysis, and numerics of ferromagnetism," *SIAM Review*, vol. 48, no. 3, 2006.

[22] L. C. Evans, *Partial Differential Equations*. American Mathematical Soc., 2010.

[23] O. Oluleke, *Finite Element Modeling For Materials Engineers Using Matlab*. London: Springer-Verlag, 2011.

[24] G. Arfken, *Mathematical Methods for Physicist 3rd Edition*. Orlando Florida: Academic Press, 1985.

[25] J. Jöst and X. Li, *Calculus of variations*. Cambridge University Press, 1998.

[26] M. Clapp, *Introducción al análisis real*. Universidad Nacional Autónoma de México, 2010.

[27] F. S. Botelho, *Functional Analysis, Calculus of Variations and Numerical Methods for Models in Physics and Engineering*. CRC Press, 2021.

[28] R. M. and R. R. C., *An Introduction to Partial Differential Equations*. Springer-Verlag, 2004.

[29] G. Allaire, "Homogenization and two-scale convergence," *SIAM Journal on Mathematical Analysis*, vol. 23, no. 6, pp. 1482–1518, 1992.

[30] H. Ulrich, *Homogenization and Porous Media*. New York: Springer Science Bussiness Media, 1997.

[31] T. Lewinski and J. Telega, *Plates, laminates and shells asymptotic analysis and Homogenization*. Singapore: World Scientific Publishing, 2000.

[32] I. Andrianov, J. Awrejcewicz, and V. Danishevskyy, *Linear and nonlinear waves in microstructured solids homogenization and asymptotic approaches*. New York: CRC Press, 2021.

[33] C. Abert, "Micromagnetics and spintronics: models and numerical methods," *The European Physical Journal B*, vol. 92, jun 2019.

[34] J. Leliaert and J. Mulkers, "Tomorrow's micromagnetic simulations," *Journal of Applied Physics*, vol. 125, may 2019.

[35] M. Donahue, "Oommf user's guide, version 1.0," 1999-09-01 1999.

[36] M.-A. Bisotti, D. Cortés-Ortuño, R. Pepper, W. Wang, M. Beg, T. Kluyver, and H. Fangohr, "Fidimag – a finite difference atomistic and micromagnetic simulation package," *Journal of Open Research Software*, vol. 6, p. 22, sep 2018.

[37] D. Berkov, "Micromagus - software for micromagnetic simulation," 01 2008.

[38] C. Abert, F. Bruckner, C. Vogler, R. Windl, R. Thanhoffer, and D. Suess, "A full-fledged micromagnetic code in fewer than 70 lines of numpy," *Journal of Magnetism and Magnetic Materials*, vol. 387, pp. 13–18, 2014.

[39] A. Vansteenkiste, J. Leliaert, M. Dvornik, M. Helsen, F. Garcia-Sanchez, and B. V. Waeyenberge, "The design and verification of MuMax3," *AIP Advances*, vol. 4, oct 2014.

[40] G. Selke, B. Kruger, A. Drews, C. Abert, and T. Gerhardt, "magnum.fd," 2020-06-01 2014.

[41] L. Gross, P. T. Cochrane, M. Davies, H.-B. Muhlhaus, and J. Smillie, "Escript: Numerical modelling with python," 2005.

[42] T. Kolev and V. Dobrev, "Modular finite element methods (mfem)," 2010.

[43] M. Alnaes, J. Blechta, J. Hake, A. Johansson, B. Kehlet, A. Logg, C. Richardson, J. Ring, M. Rognes, and G. Wells, "The fenics project version 1.5," vol. 3, 01 2015.

[44] W. Scholz, J. Fidler, T. Schrefl, D. Suess, R. Dittrich, H. Forster, and V. Tsiantos, "Scalable parallel micromagnetic solvers for magnetic nanostructures," *Computational Materials Science*, vol. 28, pp. 366–383, oct 2003.

[45] T. Fischbacher, M. Franchin, G. Bordignon, and H. Fangohr, "A systematic approach to multiphysics extensions of finite-element-based micromagnetic simulations: Nmag," *IEEE Transactions on Magnetics*, vol. 43, pp. 2896–2898, jun 2007.

[46] A. Kakay, E. Westphal, and R. Hertel, "Speedup of fem micromagnetic simulations with graphical processing units," *IEEE Transactions on Magnetics*, vol. 46, no. 6, pp. 2303–2306, 2010.

[47] R. Chang, S. Li, M. V. Lubarda, B. Livshitz, and V. Lomakin, "FastMag: Fast micromagnetic simulator for complex magnetic structures (invited)," *Journal of Applied Physics*, vol. 109, apr 2011.

[48] S. M. Esfarjani, A. Dadashi, and M. Azadi, "Topology optimization of additive-manufactured metamaterial structures: A review focused on multi-material types," *Forces in Mechanics*, vol. 7, p. 100100, may 2022.

[49] X. Wang, C. P. Neu, and D. M. Pierce, "Advances toward multiscale computational models of cartilage mechanics and mechanobiology," *Current Opinion in Biomedical Engineering*, vol. 11, pp. 51–57, sep 2019.

[50] A. Sridhar, V. G. Kouznetsova, and M. G. D. Geers, "Homogenization of locally resonant acoustic metamaterials towards an emergent enriched continuum," *Computational Mechanics*, vol. 57, pp. 423–435, feb 2016.

[51] D. M. Kochmann, J. B. Hopkins, and L. Valdevit, "Multiscale modeling and optimization of the mechanics of hierarchical metamaterials," *MRS Bulletin*, vol. 44, pp. 773–781, oct 2019.

[52] W. Chen and J. Fish, "A generalized space–time mathematical homogenization theory for bridging atomistic and continuum scales," *International Journal for Numerical Methods in Engineering*, vol. 67, no. 2, pp. 253–271, 2006.

[53] W. Chen and J. Fish, "A dispersive model for wave propagation in periodic heterogeneous media based on homogenization with multiple spatial and temporal scales," *Journal of Applied Mechanics*, vol. 68, pp. 153–161, aug 2000.

[54] P. Cupillard and Y. Capdeville, "Non-periodic homogenization of 3-d elastic media for the seismic wave equation," *Geophysical Journal International*, vol. 213, pp. 983–1001, may 2018.

[55] L. Ruiz, W. Xia, Z. Meng, and S. Keten, "A coarse-grained model for the mechanical behavior of multi-layer graphene," *Carbon*, vol. 82, pp. 103–115, feb 2015.

[56] J. Ling, A. Kurzawski, and J. Templeton, "Reynolds averaged turbulence modelling using deep neural networks with embedded invariance," *Journal of Fluid Mechanics*, vol. 807, pp. 155–166, oct 2016.

[57] J. Fish, G. J. Wagner, and S. Keten, "Mesoscopic and multiscale modelling in materials," *Nature Materials*, vol. 20, pp. 774–786, may 2021.

[58] E. Davoli, L. D'Elia, and J. Ingmanns, "Stochastic homogenization of micromagnetic energies and emergence of magnetic skyrmions," jun 2023.

[59] K. Chacouche, L. Faella, and C. Perugia, "Quasi-stationary ferromagnetic problem for thin multi-structures," *Revista Matemática Complutense*, vol. 30, pp. 657–685, jun 2017.

[60] C. Choquet, , M. Moumni, and M. T. and, "Homogenization of the landau-lifshitz-gilbert equation in a contrasted composite medium," *Discrete and Continuous Dynamical Systems - S*, vol. 11, no. 1, pp. 35–57, 2018.

[61] F. Alouges and G. D. Fratta, "Homogenization of composite ferromagnetic materials," *Proceedings of the Royal Society A: Mathematical, Physical and Engineering Sciences*, vol. 471, p. 20150365, oct 2015.

[62] U. de Maio, L. Faella, and S. Soueid, "Junction of quasi-stationary ferromagnetic thin films," *Asymptotic Analysis*, vol. 94, pp. 211–240, sep 2015.

[63] K. Santugini-Repiquet, "Homogenization of the demagnetization field operator in periodically perforated domains," *Journal of Mathematical Analysis and Applications*, vol. 334, pp. 502–516, oct 2007.

[64] H. Kronmuller, *General Micromagnetic Theory*. John Wiley Sons, Ltd, 2007.

[65] S. Bossmann and H. Wang, eds., *Magnetic Nanomaterials*. The Royal Society of Chemistry, 2017.

[66] L. An-Hui and W. Schmidt, "Nanoengineering of magnetically separable hydrogenation," *Angewandte: A journal of the German Chemical Society*, 2004.

[67] A. Gupta and M. Gupta, "Synthesis and surface engineering of iron oxide nanoparticles for biomedical applications," *Biomaterials*, 2005.

[68] B. Ramaswamy, S. Kulkarni, and et al, "Movement of magnetic nanoparticles in brain tissue: mechanisms and impact on normal neuronal function," *Nanomedicina: Nanotechnology, biology and medicina*, 2015.

[69] I. Kavre, G. Kostevc, S. Kralj, A. Vilfan, and D. babi, "Frabrication of magneto-responsive microgears based on magnetic nanoparticle embedded pdms," *RSC Advances*, 2014.

[70] P. Arosio, "Applications and properties of magnetic nanoparticles," *Nanomaterials*, vol. 11, no. 5, 2021.

[71] C. Döpke, T. Grothe, P. Steblinski, M. Klöcker, L. Sabantina, D. Kosmalska, T. Blachowicz, and A. Ehrmann, "Magnetic nanofiber mats for data storage and transfer," *Nanomaterials*, vol. 9, no. 1, 2019.

[72] T. Schrefl, G. Hrkac, S. Bance, D. Suess, O. Ertl, and J. Fidler, *Numerical Methods in Micromagnetics (Finite Element Method)*. John Wiley Sons, Ltd, 2007.

[73] K. Preis, I. Bardi, O. Biro, C. Magele, G. Vrisk, and K. Richter, "Different finite element formulations of 3d magnetostatic fields," *IEEE Transactions on Magnetics*, vol. 28, no. 2, pp. 1056–1059, 1992.

[74] A. Manaf, M. Leonowicz, H. Davies, and R. Buckley, "Effect of grain size and microstructure on magnetic properties of rapidly solidified fe82.4nd13.1b4.5 alloy," *Journal of Applied Physics*, vol. 70, no. 10, pp. 6366–6368, 1991.

[75] E. C. Stoner and E. P. Wohlfarth, "A mechanism of magnetic hysteresis in heterogeneous alloys," *Philosophical Transactions of the Royal Society of London Series A*, vol. 240, pp. 599–642, may 1948.

[76] I. Mayergoyz and G. Bertotti, *The science of hysteresis*. Elsevier, 2006.

[77] J. Nocedal, *Numerical optimization*. New York, NY: Springer, Verlag, 2nd ed. ed., 1999.

[78] F. Hecht, "New development in freefem++," *J. Numer. Math.*, vol. 20, no. 3-4, pp. 251–265, 2012.

[79] V. Carrera, "Magnetic particle simulator." https://github.com/00009/, 2023.

[80] J. Coey, *Magnetism and Magnetic Materials*. Cambridge University Press, 2010.

[81] E. Kneller and F. Luborsky, "Particle size dependence of coercivity and remanence of single domain particles," *Journal of Applied Physics*, vol. 34, pp. 656–658, 2004.

[82] D. B. Dusenbery, *Living at micro scale : the unexpected physics of being small*. Cambridge, Mass.: Harvard University Press., 2009.

[83] S. Simmons and K. Edwards, "Unexpected diversity in populations of the many-celled magnetotactic prokaryote," *Environmental Microbiology*, 2007.

[84] S. Spring, R. Amann, W. Ludwig, K. Schleifer, V. Gemerden, and N. Petersen, "Dominating role of an unusual magnetotactic bacterium in the microaerobic zone of a freshwater sediment," *Applied and Environment Microbiology*, 1993.

[85] D. Bazylinkski and R. Frankel, "Magnetosome formation in prokaryotes," *Nature Reviews Microbiology*, 2004.

[86] R. Amann, J. Peplies, and D. Schüler, "Diversity and taxonomy of magnetotactic bacteria," *Magnetoreception and magnetosomes in bacteria*, 2007.

[87] C. Lang and D. Schüler, "Biogenic nanoparticles: Production, characterization, and application of bacterial magnetosomes," *Journal of Physics: Condensed Matter*, 2006.

[88] B. Moskowitz, "Magnetic properties of magnetotactic bacteria," *Journal of Magnetism and Magnetic Materials*, 1988.

[89] B. Weiss, S. Kim, J. Kirschvink, R. Kopp, and et al., "Ferromagnetic resonance and low-temperature magnetic tests for biogenic magnetite," *Earth and Planetary Science Letters*, 2004.

[90] C. Carvallo, S. Hickey, D. Faivre, and N. Menguy, "Formation of magnetite in magnetospirillum gryphiswaldense studied with forc diagrams," *Earth Planets Space*, 2009.

[91] E. A. Périgo, B. Weidenfeller, P. Kollár, and J. Füzer, "Past, present, and future of soft magnetic composites," *Appl. Phys. Rev.*, vol. 5, p. 031301, sep 2018.

[92] O. Gutfleisch, M. A. Willard, E. Brück, C. H. Chen, S. G. Sankar, and J. P. Liu, "Magnetic Materials and Devices for the 21st Century: Stronger, Lighter, and More Energy Efficient," *Adv. Mater.*, vol. 23, pp. 821–842, feb 2011.

[93] J. M. Silveyra, E. Ferrara, D. L. Huber, and T. C. Monson, "Soft magnetic materials for a sustainable and electrified world," *Science*, vol. 362, no. 6413, p. eaao0195, 2018.

[94] P. S. Normile, M. S. Andersson, R. Mathieu, S. S. Lee, G. Singh, and J. A. D. Toro, "Demagnetization effects in dense nanoparticle assemblies," *Applied Physics Letters*, vol. 109, p. 152404, 2016.

[95] B. Duong, H. Khurshid, P. Gangopadhyay, J. Devkota, K. Stojak, H. Srikanth, L. Tetard, R. A. Norwood, N. Peyghambarian, M.-H. Phan, and J. Thomas, "Enhanced magnetism in highly ordered magnetite nanoparticle-filled nanohole arrays," *Small*, vol. 10, p. 2840, 2014.

[96] Q. Li, C. W. Kartikowati, T. Iwaki, K. Okuyama, and T. Ogi, "Enhanced magnetic performance of aligned wires assembled from nanoparticles: from nanoscale to macroscale," *R. Soc. Open Sci.*, vol. 7, p. 191656, apr 2020.

[97] V. Merk, M. Chanana, N. Gierlinger, A. M. Hirt, and I. Burgert, "Hybrid Wood Materials with Magnetic Anisotropy Dictated by the Hierarchical Cell Structure," *ACS Appl. Mater. Interfaces*, vol. 6, pp. 9760–9767, jun 2014.

[98] K. N. Al-Milaji, R. L. Hadimani, S. Gupta, V. K. Pecharsky, and H. Zhao, "Inkjet Printing of Magnetic Particles Toward Anisotropic Magnetic Properties," *Sci. Rep.*, vol. 9, pp. 1–9, nov 2019.

[99] K. Deng, Z. Luo, L. Tan, and Z. Quan, "Self-assembly of anisotropic nanoparticles into functional superstructures," *Chem. Soc. Rev.*, vol. 49, pp. 6002–6038, aug 2020.

[100] H. Gavilán, K. Simeonidis, E. Myrovali, E. Mazarío, O. Chubykalo-Fesenko, R. Chantrell, Ll. Balcells, M. Angelakeris, M. P. Morales, and D. Serantes, "How size, shape and assembly of magnetic nanoparticles give rise to different hyperthermia scenarios," *Nanoscale*, vol. 13, no. 37, pp. 15631–15646, 2021.

[101] E. H. Sánchez, M. Vasilakaki, S. S. Lee, P. S. Normile, M. S. Andersson, R. Mathieu, A. López-Ortega, B. P. Pichon, D. Peddis, C. Binns, P. Nordblad, K. Trohidou, J. Nogués, and J. A. De Toro, "Crossover From Individual to Collective Magnetism in Dense Nanoparticle Systems: Local Anisotropy Versus Dipolar Interactions," *Small*, vol. 18, p. 2106762, jul 2022.

[102] S. Singh, Y. Mollet, and J. Gyselinck, "Numerical Modeling of the Soft Magnetic Composite Material," in *2019 Electric Vehicles International Conference (EV)*, pp. 1–5, IEEE, oct 2019.

[103] J. M. Martinez-Huerta, J. D. L. T. Medina, L. Piraux, and A. Encinas, "Configuration dependent demagnetizing field in assemblies of interacting magnetic particles," *Journal of Physics: Condensed Matter*, vol. 25, no. 22, p. 226003, 2013.

[104] B. Nam, J. Kim, and K. Ki Hyeon, "Analysis of effective permeability behaviors of magnetic hollow fibers filled in composite," *Journal of Applied Physics*, vol. 111, p. 07E347, 2012.

[105] M. Sato and Y. Ishii, "Simple and approximate expressions of demagnetizing factors of uniformly magnetized rectangular rod and cylinder," *Journal of Applied Physics*, vol. 66, p. 983, 1989.

[106] Y. Velázquez-Galván, J. M. Martínez-Huerta, J. D. L. T. Medina, Y. Danlée, L. Piraux, and A. Encinas, "Dipolar interaction in arrays of magnetic nanotubes," *Journal of Physics: Condensed Matter*, vol. 26, no. 2, p. 026001, 2013.

[107] Y. Velázquez-Galván and A. Encinas, "Analytical magnetostatic model for 2d arrays of interacting magnetic nanowires and nanotubes," *Physical Chemistry Chemical Physics*, vol. 22, no. 23, pp. 13320–13328, 2020.

[108] S. Pal, S. Chandra, M.-H. Phan, P. Mukherjee, and H. Srikanth, "Carbon nanostraws: nanotubes filled with superparamagnetic nanoparticles," *Nanotechnology*, vol. 20, no. 48, p. 485604, 2009.

[109] J. S. Segmehl, A. Laromaine, T. Keplinger, A. May-Masnou, I. Burgert, and A. Roig, "Magnetic wood by in situ synthesis of iron oxide nanoparticles via a microwave-assisted route," *J. Mater. Chem. C*, vol. 6, pp. 3395–3402, mar 2018.

[110] G. J. Strijkers, J. H. J. Dalderop, M. A. A. Broeksteeg, H. J. M. Swagten, and W. J. M. de Jonge, "Structure and magnetization of arrays of electrodeposited Co wires in anodic alumina," *J. Appl. Phys.*, vol. 86, pp. 5141–5145, nov 1999.

[111] A. Encinas-Oropesa, M. Demand, L. Piraux, I. Huynen, and U. Ebels, "Dipolar interactions in arrays of nickel nanowires studied by ferromagnetic resonance," *Phys. Rev. B*, vol. 63, p. 104415, feb 2001.

[112] I. Fredholm, "Sur une classe d'équations fonctionnelles," *Acta Mathematica*, vol. 27, no. 0, pp. 365–390, 1903.